SPATIALLY ADAPTIVE CONSTRAINED NON NEGATIVE MATRIX FACTORIZATION FOR HYPERSPECTRAL UNMIXING

By

Miguel Angel Goenaga-Jimenez

A dissertation submitted in partial fulfillment of the requirements for the degree of
DOCTOR OF PHILOSOPHY
in
COMPUTING AND INFORMATION SCIENCE AND ENGINEERING

University of Puerto Rico
MAYAGUEZ CAMPUS
2014

Approved by:

_____   _____

Shawn Hunt, PhD   Date
President, Graduate Committee

_____   _____

Miguel Velez-Reyes, PhD   Date
Co-President, Graduate Committee

_____   _____

Domingo Rodriguez, PhD   Date
Member, Graduate Committee

_____   _____

Vidya Manian, PhD   Date
Member, Graduate Committee

_____   _____

J. Danilo Chinea, PhD   Date
Member, Graduate Committee

_____   _____

Samuel Santana, PhD   Date
Graduate School Representative

_____   _____

Wilson Rivera, PhD   Date
Program Coordinator

ABSTRACT

President: Shawn Hunt, PhD, Co-President: Miguel Velez-Reyes, PhD.
Major Department: Computing and Information Science and Engineering.

This dissertation proposes a spatially adaptive constrained Nonnegative Matrix Factorization (sacNMF) for unmixing of hyperspectral imagery. The image is decomposed into spectrally homogeneous regions using quadtree region partitioning. The constrained Nonnegative Matrix Factorization (cNMF) is applied to the individual image tiles to perform spectral endmember extraction. Spectral endmembers are clustered into endmember classes that better capture the endmember spectral variability across the image. Abundances are estimated using constrained least squares or sparse regression depending on the number of spectral endmembers. It is shown that by decomposing the image into spectrally homogeneous regions, the piecewise convex structure of the spectral cloud and the material mixing constraints imposed by the spatial relation between materials are better captured. A computational framework in MATLAB is developed to implement the proposed approach. The performance of sacNMF is evaluated using real hyperspectral data from the AVIRIS and the AISA sensor. Unmixing results are compared to available ground truth for the images and to results from standard unmixing algorithms, and some algorithms that use spatial information. Experimental results show that sacNMF outperforms the cNMF applied to the entire image (no spatial decomposition) and other standard unmixing algorithms that do not incorporate spatial information. Results also show that sacNMF performs equally or better than unmixing algorithms that incorporate spatial information..

RESUMEN

Presidente: Shawn Hunt, PhD, Co-Presidente: Miguel Velez-Reyes, PhD.
Departamento: Ciencias de Computación e Información e Ingeniería.

Esta disertación propone el método factorización con matrices no negativas con restricciones adaptativo espacialmente (sacNMF) para desmezclado de imágenes hiperespectrales. La imagen se descompone en regiones espectralmente homogéneas utilizando quadtree en la partición de regiones. El limitado método factorización de matrices no negativas con restricción (CNMF) se aplica a las particiones individuales de la imagen para llevar a cabo la extracción de las firmas espectrales. Las firmas espectrales se agrupan en clases de firmas espectrales, que capturan mejor la variabilidad de las firmas espectrales a través de la imagen. Las abundancias se estiman mediante restricción de mínimos cuadrados o regresión esparcida en función del número de firmas espectrales. Se muestra que mediante la descomposición de la imagen en regiones espectralmente homogéneas, la estructura a trozos de la nube espectral es convexa y las limitaciones impuestas por la relación espacial entre los materiales mezclados es mejor capturada. Un marco computacional en MATLAB se ha desarrollado para implementar el enfoque propuesto. El rendimiento de sacNMF se evalúa a partir de datos hiperespectrales reales de sensores como AVIRIS y AISA. Resultados del desmezclado espectral se comparan con datos verdaderos del suelo disponible para las imágenes y para los resultados de los algoritmos de desmezclado estandarizados, y algunos algoritmos que utilizan la información espacial. Los resultados experimentales muestran que sacNMF supera al CNMF aplicado a toda la imagen (sin descomposición espacial) y otros algoritmos de desmezclado estándar que no incorporan la información espacial. Los resultados también muestran que sacNMF realiza igual o mejor desmezclado que algoritmos que incorporan la información espacial.

Copyright

To my parents Carmen, Miguel (R.I.P.), my brother Gabriel, my sister Eloina, my daughter Laura Sofia and my wife Orisnella, I love you.

ACKNOWLEDGEMENTS

TABLE OF CONTENTS

TABLES LIST

FIGURES LIST

ABBREVIATIONS

(cNMF)   constrained non negative matrix factorization

(sacNMF)   spatially adaptive constrained non negative matrix factorization

(MNF)   minimum noise fraction

(MaxD)   Maximum Distance

(VCA)   Vertex Component Analysis

(PI)   projection index

(PCE)   Piece-Wise Convex Endmember

(SMM)   Stochastic Mixing Model

(AMEE)   Automated Morphological Endmember Extraction Approach

(SSEE)   Spatial-Spectral Endmember Extraction Approach

(SVD)   singular value decomposition

(SAHU)   Spatial Adaptive Hyperspectral Unmixing Approach

(UUMR)   Unsupervised Unmixing based on Multiscale Representation
                Approach

1. INTRODUCTION

1.1   Justification.

Hyperspectral imaging (HSI) systems collects hundreds of images at contiguous spectral bands in the electromagnetic spectrum. HSI technology is used in a wide range of remote sensing applications such as agriculture, geology, ecology, and surveillance. The high spectral resolution provided by HSI can be used to identify materials by their spectral signatures. Processing of hyperspectral data is not a trivial task because it is usually necessary to deal with large volumes of data produced inherently by HSI systems subject to different sources of spectral variability such as atmospheric effects, and illumination changes between pixels among others. Furthermore, in many practical applications, such as threat detection in surveillance systems, it is crucial to perform the processing in real time, making this task even more challenging.

In hyperspectral imaging, the reflected or emitted radiation represented by a single pixel rarely comes from the interaction with a single homogeneous material. However, the high spectral resolution of imaging spectrometers enables the detection, identification, and classification of subpixel (means when a pixel is composed of different materials) objects from their contribution to the measured spectral signal. Unmixing is a hyperspectral image processing approach for subpixel information extraction where the measured spectral signature is decomposed into a collection of constituent spectra, or endmembers, and a set of corresponding fractions or abundances of the particular endmembers in that pixel.

The use of a single endmember spectrum, to represent an endmember class does not take into account the variability of spectral signatures caused by natural factors. For instance, in a forest scene, the spectral signature of a particular tree species may vary due to minerals concentration in

the soil or by water content. A single spectral signature can, by itself, provide suitable accuracies in some relatively homogeneous environments. Because of the spectral complexity of many landscapes, the use of single endmember spectrum to represent a particular material may result in inaccurate unmixing analysis for complex regions over large landscapes.

1.2 Problem Statement.

The use of a single spectral signature to represent an endmember across a large landscape does not take into account the natural variability of spectral signatures caused by multiple factors. A single spectral signature may provide suitable accuracies in a local neighborhood, but, because of the complexity of many landscapes, the use of single endmember spectra may result in inaccurate unmixing analysis over large landscapes. Therefore, it is more appropriate to use a set of representative spectra as endmembers to account for spectral variability. In unmixing, this set of representative spectra are called spectral endmember classes. They represent the basic components of an image, accounting for spectral variability.

This research proposes to address the question of how to perform unsupervised unmixing where endmember classes are assumed to be composed of multiple spectral endmembers. We proposed to look at local information to extract local endmember information and merge it at global level to develop an accurate description of the scene under study. The rationale is that, at the local level, endmember classes are more uniform, so that a single endmember is adequate to represent it. Also, is worth to mention that rare endmembers are easier to find when using local data. In addition, in uniform areas, the data cloud behavior better follows the convex hull model used in the unmixing analysis.

The proposed work contributes to information sciences by looking at information extraction from hyperspectral image data. In the computing area, we study the integration of different existing and novel approaches to perform the unmixing process into a Matlab framework for unsupervised unmixing.

1.3   Overview of sacNMF.

This research proposes an approach to perform unsupervised unmixing where endmember classes, composed of multiple spectral signatures, are used to describe the "endmember" across a large scene. Local spectral signatures are extracted from spectrally homogeneous regions. Spectrally homogeneous regions are identified using a quadtree region partitioning method. Once the regions are identified, local endmembers can be extracted using any of the available endmember extraction methods. Endmember classes are built by clustering local spectral endmember signatures to build up a more precise description of the landscape under study. The cNMF is used at individual image tiles to perform endmember extraction. We call the proposed approach the spatially adaptive constrained NMF or sacNMF. The approach is summarized in Figure 1-1.
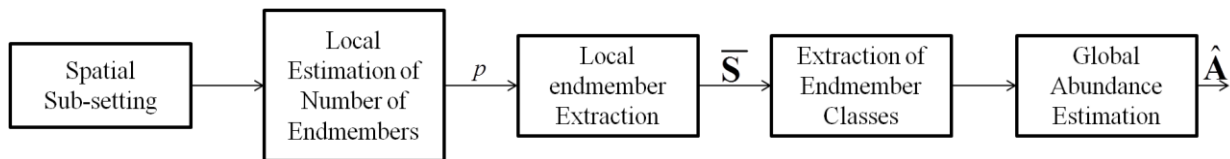
Figure 1-1. Local Unmixing Analysis Approach.

Initially, the spatial subsetting is performed comparing the value of the homogeneity metric between the whole image and the region quadtree of the image recursively split into four quadrants until the value of the homogeneity metric of the quadrants is smaller than the value of the homogeneity metric of the full image. The metric used for comparing the homogeneity metric between image subsets is the Shannon Entropy and comes from the image data and can be calculated using the expression:

$$\boldsymbol{Shannon}\ (\boldsymbol{X}) = -\sum_{i=1}^{Alpha} \boldsymbol{q}(\boldsymbol{x_i})\log(\boldsymbol{q}(\boldsymbol{x_i})) \tag{1.1}$$

where **X** is a given image or portion of image and $\boldsymbol{q}(\boldsymbol{x_i})$ is the ratio between the sum of all elements of the same sample $\boldsymbol{x_i}$ in specific area, and the whole area of image, and $\boldsymbol{Alpha}$ is the number of the specific areas. This is performed on vector, after to reshape the 3D data to 2D data.

Quadtree partitioning (see Chapter 4) is used to decompose the image in spectrally uniform regions. After image decomposition, unmixing is performed on each tile using cNMF.

The process to estimate the number of endmembers $\boldsymbol{p}$ is performed by applying the cNMF to each tile and varying the rank of the positive matrix approximation $\boldsymbol{p}$ from 2 to 20. The number of endmembers for that particular tile is selected such that the cNMF approximation error does not change significantly (< 0.00005).

$$\boldsymbol{E_p} = \frac{\|X - S_p A_p\|_F^2}{\|X\|_F^2} \tag{1.2}$$

After extracting the endmembers for each tile, hierarchical clustering is performed to extract the endmember classes. Spectral endmembers represent the distinct components in a scene as well as their spectral variability.

Abundances are computed by solving the abundance estimation problem for the full image using all extracted spectral endmembers. The abundance for an endmember class is the sum of the abundances of the spectral endmembers in the class.

1.4 Objectives.

1.4.1 General Objective.

The main objective of this research was to develop an unsupervised unmixing MATLAB framework based on the non negative matrix factorization for large scenes that take full advantage of local information to build a global image description.

1.4.2 Specific Objectives.

Specific objectives of this research are:

- ✓ Develop methods that extract local information for unmixing.
- ✓ Develop a cNMF algorithm that takes full advantage of information in the spatial domain.
- ✓ Study the effect of multiple resolution images in the use of local information for unmixing in Hyperspectral Imaging.
- ✓ Develop a MATLAB based framework to implement a prototype of the proposed approach.
- ✓ Test and validate the system using real hyperspectral imagery.

1.5 Contributions.

The main contribution of this work is in the area of unmixing in hyperspectral imaging. The significance of unmixing for the analysis of hyperspectral imagery is important. It is necessary that the unmixing algorithms take advantage of the spatial and the spectral information available in hyperspectral images. The developed approach uses both spatial and spectral information for

unmixing analysis of hyperspectral imagery and the fact that the behavior of the data cloud in homogeneous regions is convex (see Ch.3) is very convenient in unmixing analysis. This work builds up a framework in MATLAB for unsupervised unmixing that makes possible the analysis of these images for several applications. Because the information extraction is unsupervised, the interpretation of the results require analyst intervention.

This work is part of the research field of Computational Signal and Image Processing inside of the concentration in Computer Science and Engineering in the Computing and Information Science and Engineering (CISE) doctoral program at the University of Puerto Rico [35]. CISE program seeks to integrate engineering, computing and information science components. In this work, these three components can be identified. The engineering component involves the design of the spatial-spectral algorithm for the unmixing analysis based on spatially homogeneous division of the image. The computing component is formed by a framework for the unsupervised unmixing analysis in MATLAB. The information science component is related to the information extraction process from hyperspectral imagery in which the problem of estimation of the basic components and extraction of spectral signatures is very important. The developed unmixing technique is a novel approach that takes advantage of existing techniques of image processing and data mining such as clustering for the extraction of information (number and the spectral endmember classes) from hyperspectral imagery.

Finally, some published articles during the process of the research are:

Goenaga-Jimenez, M. and Velez-Reyes, M., "Incorporating Local Information in Unsupervised Hyperspectral Unmixing". In Proceedings of SPIE: Algorithms and Technologies for Multispectral, Hyperspectral, and Ultraspectral Imagery XVIII, Vol 8390, April 2012.

Goenaga, M. A., Torres-Madronero, M. C., Velez-Reyes, M., Van Bloem, S. J., Chinea, J. D. "Unmixing Analysis of a Time Series of Hyperion Images Over the Guánica Dry Forest in Puerto Rico". Journal of Selected Topics in Applied Earth Observations and Remote Sensing, IEEE Geoscience; Signal Processing & Analysis Issue: 99. 2012, Page(s): 1 - 10.

Goenaga-Jimenez M.A. and Velez-Reyes, M. "Comparing Quadtree Region Partitioning Metrics for Hyperspectral Unmixing." In Proceedings of SPIE: Algorithms and Technologies for Multispectral, Hyperspectral, and Ultraspectral Imagery XIX, Vol. 8743, April 2013.

Goenaga-Jimenez M.A., and Velez-Reyes, M. "Integrating Spatial Information in Unmixing using the Nonnegative Matrix Factorization". In Proceedings of SPIE: Algorithms and Technologies for Multispectral, Hyperspectral, and Ultraspectral Imagery XX, Vol. 9088-39, May 2014.

Hunt, S., Rodríguez, N., Goenaga-Jimenez, M., and Velez-Reyes, M., "Determining Optimum Pixel size for Classification". In Proceedings of SPIE: Algorithms and Technologies for Multispectral, Hyperspectral, and Ultraspectral Imagery XX, Vol. 9088-34, May 2014.

1.6   Outline

Background and literature review is presented in Chapter 2. Data used for the experiments is described in that chapter.

Exploratory visual analysis to study the relation between spatial and spectral information is shown in Chapter 3. This exploratory analysis serves as the motivation for the structure proposed for the sacNMF.

Chapter 4 presents image decomposition using quadtree partitioning. Experiments with real data are used to evaluate different spectral uniformity metrics for the partitioning.

The Chapter 4 incorporates the local information in unsupervised hyperspectral unmixing processes. Consists of five sections, the first section mentions the quadtree representation, the second section is about the metrics in hyperspectral images, the third to the last section shows comparing results between different images.

Chapter 5 describes the proposed sacNMF algorithm.

Chapter 6 presents evaluation of the sacNMF using different data sets and available ground truth.

Chapter 7 presents a discussion about ethical issues in remote sensing. Chapter 8 presents conclusions and future work.

2. BACKGROUND AND LITERATURE REVIEW

This chapter presents a general summary of the current state of the art in hyperspectral image processing emphasizing in the linear unmixing methods that use both spatial and spectral information. In Section 2.1, an overview of hyperspectral imaging is presented. Then, in Section 2.2., the linear mixing model (LMM) and spectral unmixing is reviewed. In Sections 2.3. and 2.4, several approaches to determining the number of endmembers and endmember extraction techniques are described. In Section 2.5, abundance estimation approaches are described. Section 2.6 introduces the concept of endmember variability in unmixing analysis and clustering algorithms. The Sections 2.7 and 2.8 present a review of the Nonnegative Matrix Factorization method to solve hyperspectral unmixing. Section 2.9 shows two different approaches to find boundaries in the image. Finally, Section 2.10 describes the hyperspectral imagery used in the research.

2.1   Hyperspectral Imaging.

Remote sensing can be defined as the measurement of properties of an object on the Earth's surface with data from aircraft or satellites. Since they are not in direct contact with an object of interest, must rely on signals propagating some form, for instance, microwave or acoustic [1]. These remote systems, principally those deployed in satellites, supply recurrent and reliable visualization of the Earth's surface, that is important to follow variations in the short and long term, see Figure 2-1 [1]. A few of the critical applications using remote sensing technology are:

Figure 2-1 Images Before (left, 2008) and after (right, 2011) of Tsunami over Japan. Image capture with ASTER [1].

- *Ecological Risks***:** Pollutants (direct and indirect), environmental substrate.

- *Coastline and Inner Seawaters***:** Biochemical standoff discovery, oil leak watching and tracing.

- *Ecosystem:* Content of water and chlorophyll in the leaf, callose, cellulose, and nonphotosynthetic components.

- *Commercial Applications***:** Exploration of minerals, food production and forestry behavior.

- *Military Applications:* Detection of mines in the land, tracing of objects, traps.

- *Others:* Medical and human arrangement, etc.

- The process of remote sensing and hyperspectral image processing, is summarized in Figure 2-2.
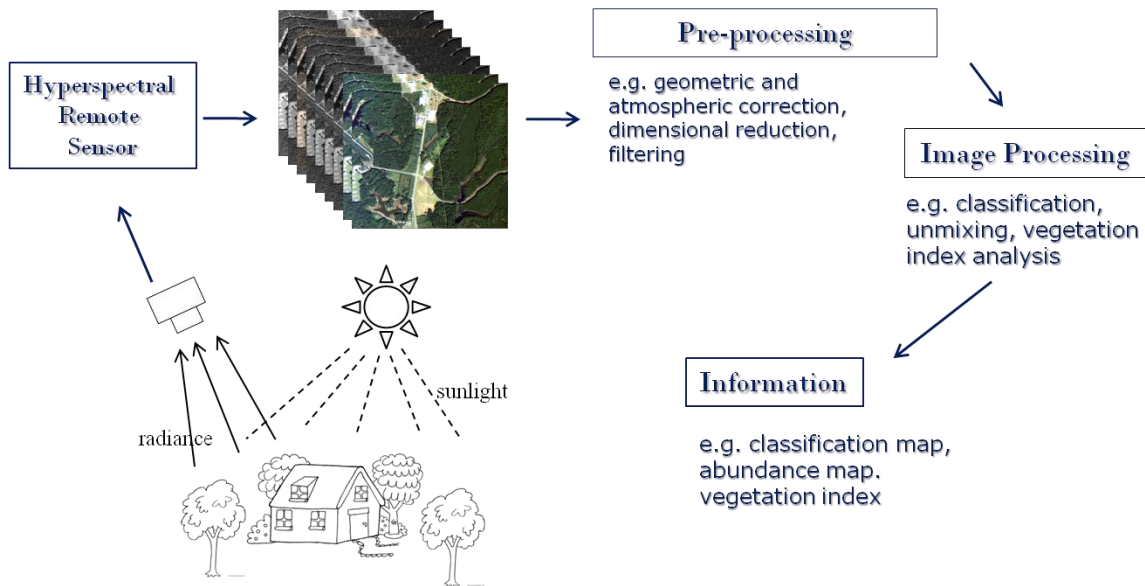
Figure 2-2 Hyperspectral Image processing chain [2].

Materials absorb, reflect, and radiate electromagnetic energy, at particular wavelengths, in distinct forms associated to their structure, a hyperspectral image is a result of the collection of a hyperspectral sensor. The smallest element in a hyperspectral image is called pixel. The reflectance associated with each pixel is the result of interaction of different physical factors but in particularly of the constituent materials in the field of view of the sensor.
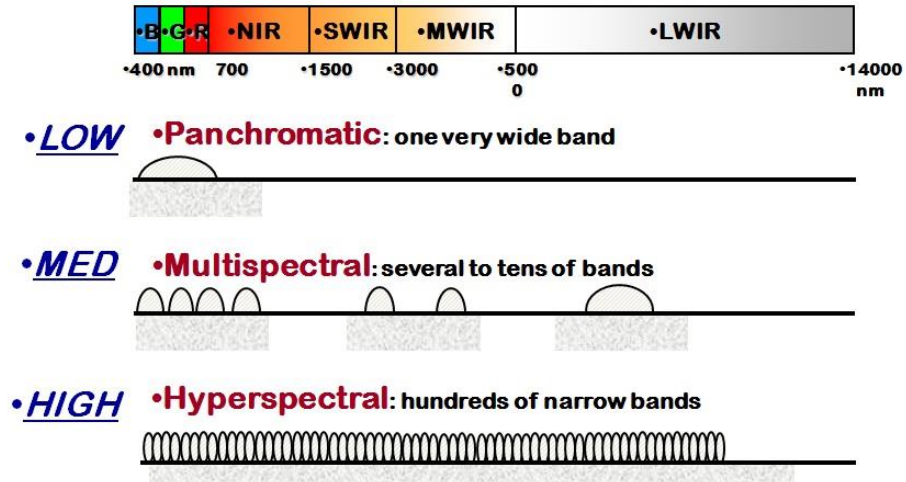
Figure 2-3 Types of spectral sampling in spectral imaging [2].

Multispectral sensors acquire images simultaneously at separate non-contiguous wavelength intervals or bands. Multispectral scanners typically record up to 10, or so, spectral bands with bandwidths in the order of 0.1 micrometers. More recently, remote sensing imaging technology has advanced in two major ways: enhancement in the spectral resolution and enhancement in spatial resolution. The hyperspectral images samples the spectra at hundreds contiguous wavelengths with a wavelength with in the order of 1-10 nm. Figure 2-3 illustrates the differences between multispectral and hyperspectral sensing.

Three aspects characterize in a general way a hyperspectral image: the spatial resolution that determines the spatial size of the pixel, the spectral resolution that determines the wavelength thickness between different bands captured by the sensor, and the radiometric resolution that determines the amount of radiation that the sensor is capable to discriminate. Usually hyperspectral images have more than 100 bands. Each hyperspectral pixel is a vector, where the number of components be subject to the number of bands in the image that represents a spectral signature (Figure 2-4).

12

Examples of hyperspectral imagers are listed in the Table 2-1 Airborne Visible Infrared Imaging Spectrometer (AVIRIS) [3], 244-band AISA Eagle [4], HYPERION satellite sensor [5] developed by NASA and HYDICE sensor
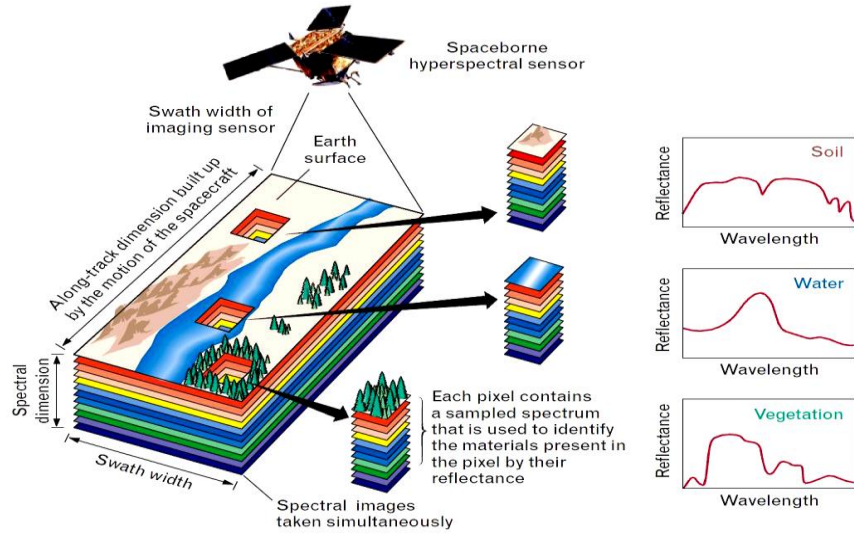
Figure 2-4 Endmembers for Hyperspectral Image [6].

Table 2-1. Examples of Hyperspectral Sensors

Specification	AVIRIS	HYDICE	HYPERION
Spectral Range (nm)	400-2500	400-2500	400-2500
Spectral Resolution (nm)	10	10	10
Spectral Samples (bands)	224	210	220
Spatial Resolution (m)	20	1-4	30
Radiometric Resolution (bits)	12	16	16

2.2   Linear Mixing Model and Spectral Unmixing.
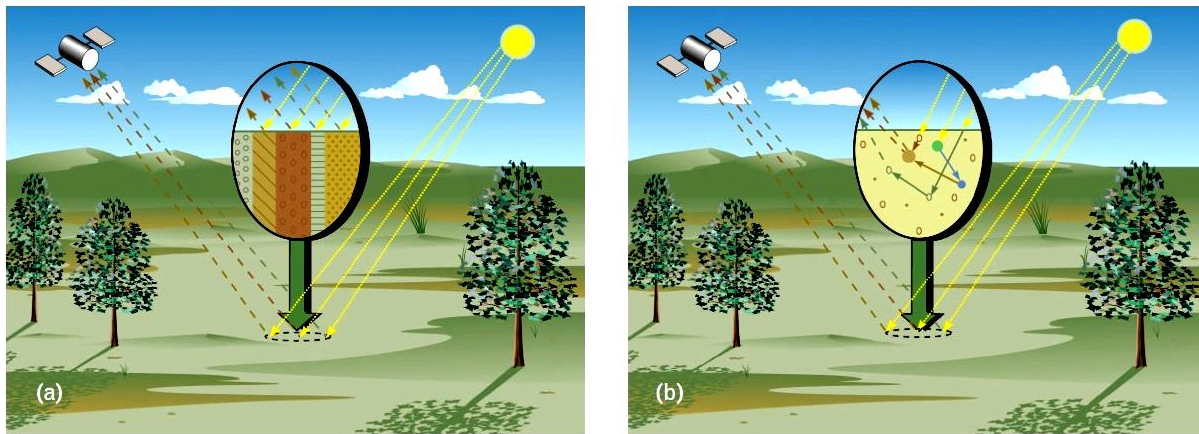
Figure 2-5 Mixing models. (a) The linear mixing models, (b) Nonlinear mixing models [7].

In hyperspectral imaging, the reflected or emitted radiation represented by a single pixel in the remotely sensed image rarely comes from the interaction with a single homogeneous pure material. However, the high spectral resolution of imaging spectrometers enables the detection, identification, and classification of sub-pixel objects from their contribution to the measured spectral signal. Every approach in unmixing hyperspectral data should begin with a model that describes how the component of materials in a pixel associate to produce the merged spectrum measured in the sensor. The mixing models try to characterize the essential physics that are the grounds of hyperspectral phenomenon, and unmixing procedures that use these models to accomplish the inverse process, trying to recuperate the endmembers and associate fractional abundances from the mixed pixel. Figure 2-5 shows two mixing models, the linear mixing and nonlinear mixing models. The first model [6] represents a pixel as the linear combination of the

spectral signatures of each material multiplied by its fractional coverage area or abundance and is given by.

$$x_j = \sum_{i=1}^{p} s_i a_i + w = S a_i + w_j \ , \ j = 1, 2, 3, \dots, N \qquad (2.1)$$

where $x_j \epsilon \ \mathbb{R}_+^m$ is the measured spectral signature at pixel, $S \epsilon \ \mathbb{R}_+^{m \times p}$, is the endmembers matrix, $a_j \epsilon \ \mathbb{R}_+^p$ is the spectral abundances vector, and $w_j \epsilon \ \mathbb{R}^m$ is a measurement noise vector, m is the number of spectral bands, and p is the number of endmembers [1]. In HSI, typically, $m > p$, notice that all elements of S, a, and x are constrained to be positive, and the sum of a_{ij} for all spectral bands m is less than or equal to one. For the full HSI, the linear mixing model given above can be written in matrix form as:

$$\mathbf{X} = \mathbf{SA} + \mathbf{W} \qquad (2.2)$$

where $\mathbf{X} = [x_1 \dots x_N]$ is the matrix that contain all pixels in the image, $\mathbf{S} = [s_1 \dots s_p]$ the endmembers matrix, $\mathbf{A} = [a_1 \dots a_N]$ the abundance matrix, $\mathbf{W} = [w_1 \dots w_N]$ the noise matrix, this noise is related with sensor limitations in spatial and spectral domains and by natural spectral variability [26], and N is the number of pixels in the image.

Spectral unmixing is the inverse procedure by which given the image $\mathbf{X}$, we want to determine p the number of endmembers, the endmembers matrix S, and the abundance matrix A, as depicted in Figure 2-6.
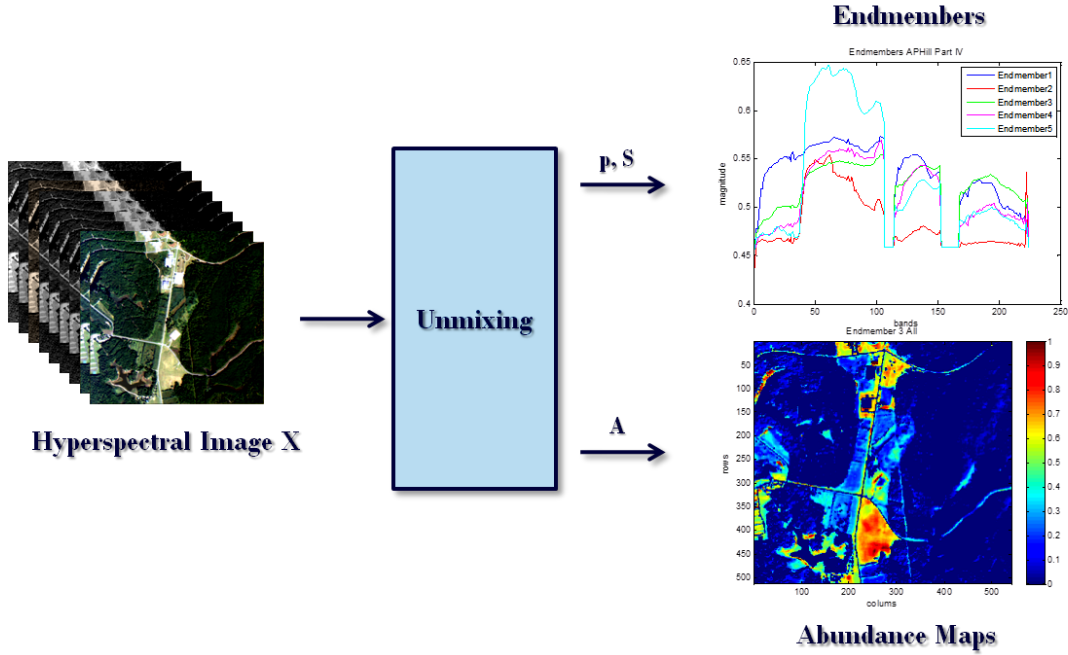
Figure 2-6 Spectral Unmixing Process [10].

Mathematically, the unmixing problem could be formulated as follows:

$$\left(\widehat{p}, \widehat{S}, \widehat{A}\right) = argmin_{S_{ij}>0,\ A_{ij}>0, \sum_{i=1}^{p} a_i \leq 1, p \in Z} \|X - SA\|_F^2 \qquad (2.3)$$

where $\| \ \|_F$ is the Frobenious norm (used by most authors), and 1_N is a N-dimensional vector of ones. For known p, the optimization problem (2.3) is connected to the non-negative matrix factorization approximation problem considered in many fields [8], [9], and [10]. For fixed p, we can consider equation (2.3) as a constrained non negative matrix factorization (cNMF) [11]. Z are the integers numbers, and $argmin$ means minimize the expression $\|X - SA\|_F^2$ subject to the constraints.

If in (2.3), in addition to p, the matrix of endmember (**S**) is known, then the problem is the abundance estimation problem, which is a constrained linear least squares problem. The estimation problem for the abundance can be resolved with diverse methods.

Different approaches have been proposed to solve the linear unmixing problem. Most methods solve the unmixing problem in two stages and not as an optimization problem like (2.3). In the first step, the number of endmembers is determined and spectral signatures of the endmembers are extracted by searching for "pure" pixels in the image or by using spectral signatures from libraries or from field data [6][7][10][12]. In the second step, abundances are calculated by solving a constrained linear least squares problem [13] - [15]. However, though most of the unmixing approaches use similar mathematical procedures, they differ in the criteria and the assumptions used for endmember extraction [16].

2.3   Approaches to Determine the Number of Endmember.

2.3.1 Determining the Number of Endmembers.

Most endmember extraction methods consider the number of endmembers as an input to the algorithm, for this reason the estimation of the number of endmembers also has to be considered in the analysis of the unmixing problem solution. Approaches pursued in hyperspectral unmixing to determine the number of endmembers can be grouped as follows:

- **Rank of the signal subspace:** the number of endmembers is equal to the "rank" of the covariance matrix [17].

- **Rank of the data matrix X:** here the rank of X in the linear algebra sense is used. Recall that the rank of X is equal to the rank of the sample correlation matrix ($\frac{1}{N}X^TX$) [17]**.**

- **Positive rank of X:** thus is related to the non-negative matrix factorization (**pos_rank(X)**) [6], [10].

The presence of noise and natural spectral variability makes the determination of the number of endmembers, like any rank estimation problem, hard. The relationship between the different definitions of rank are as follows:

rank(X) **= rank(corr(X))**

rank(cov(X)) **≤ rank(X)**

rank(X) **≤ pos_rank(X)**

Therefore, these notions are not equivalent.

Here, we use the positive rank as an estimate of the number of endmembers. There are no direct methods to estimate the positive rank. We use the fitting error as a function of p and use as an estimate of the number of endmembers the value after which no significant change in fitting error is achieved. The fitting error is given by:

$$E_p = \frac{\|X - SA\|_F^2}{\|X\|_F^2} \tag{2.4}$$

where $\|\ \|_F$ is the Frobenius norm. The estimate corresponds to the knee of the error curve where further increase of p does not result in a significant reduction of the fitting error.

Other methods to estimate the number of endmembers from various approaches are mentioned in references [18], [19]. These methods, are related to as Signal Subspace Estimation (SSE), [18] and virtual dimensionality [19], which compares the eigenvalues of the covariance and correlation matrices for the images [20]. A hypothesis testing problem is used to determine in [19] if the differences is positive or zero, how many times the difference is positive is an estimate of how many endmembers there are. The theoretical soundness of this method is questioned in [20].

2.4 Endmember Extraction Approaches.

Once the number of endmember is estimated, the next step is to find the spectral signatures. Some algorithms assume that the endmembers are known, and signatures from field or laboratory spectral libraries can be used as endmembers. Other spectral unmixing algorithms are based on the assumption of pure pixels and search them in the image. The automated unmixing algorithms seek to extract the endmember signatures from the hyperspectral image itself. These endmembers are called image-based endmembers [19].

Unmixing algorithms can be classified based on the underlying model in: ***Geometric Models*** [93]***, Parametric Models*** [93] ***and Spatial-Spectral Algorithms*** [44]***.***

2.4.1 Geometric Approaches.

Algorithms based on geometric models assume that pixels are bounded in a convex hull where the corners are the endmembers. In geometrical mixing, the determination of the endmembers is the problem of finding t the corners of the minimum volume simplex that encloses the cloud of data [10], [22]. Figure 2-8 show illustrations of the convex hull.

a)   b)
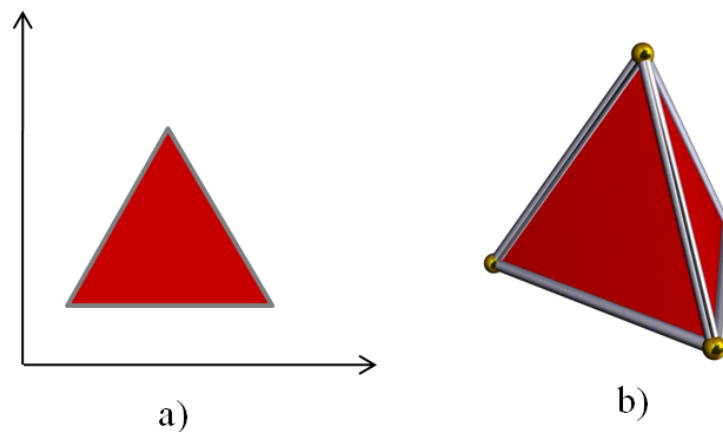
Figure 2-7. Convex hull illustration in (a) 2-D and (b) A regular 3-simplex or tetrahedron [22].

The relation between the unmixing problem and convex geometry has been used by many researchers to develop algorithms for the extraction of endmember signatures. Some of the commonly used geometric methods are summarized below.

The **Pixel purity index** (PPI) [19] is a popular approach used in endmember selection. PPI tries to locate the purest pixels in the image using random projections onto random unit vectors and visualizations using scatter plots. The pixels in the extreme on each projection are stored and the pixels marked as extreme multiple times are confirmed as pure. The approach requires data preprocessing and post processing before determining the endmembers [20]. Usually this approach runs using principal component transformation or minimum noise fraction (MNF) image excluding noisy bands.

Another approach for endmember determination is described in [20]. This algorithm does not do dimensionality reduction; instead it thins the data set using exemplar selection process in which redundant spectra are rejected. The elimination of redundant spectra is made by computing the spectral angle between vectors and keeping those that are separated by a threshold angle. The remaining vectors that are not separated are thinned from the data. The approach finds a basis group of lower dimension than the initial data using Gram-Schmidt orthogonalization. Before the thinned data is projected onto the previously basis subspace, a simplex is established using a minimum volume transform [22].

The **N-FINDR** method developed by Winter [33] and modified by Du et al. [34] looks for a convex hull with volume maximum inscribed into the cloud of data, based on $\sum_{i=1}^{p} a_{ij} = 1$ and imposing the assumption that there is at least one pure pixel per each endmember material in the image. They identify pure pixels as those pixels that have one of its abundance coefficients approximately

equal to one. The process is initialized with an arbitrary group of pixels as endmembers. The group of estimated endmembers is redefined by evaluating each pixel if it is at the extreme of the scatter plot to find new pure pixels. The endmembers are allocated in the matrix S and the volume of the convex hull is computed. If the new pixel increases the volume, the endmember is replaced by the pixel. This procedure is continued until there are no more pixel substitutions. The matrix $\overline{S}$ in (2.5) is the endmembers matrix S enlarged with a row of ones and V is the volume of the convex hull.

$$\overline{S} = \begin{bmatrix} 1 & 1 & ....1 \\ s_1 & s_2 & ....s_p \end{bmatrix} \; ; V(\overline{S}) = \frac{1}{p-1} \, |\overline{S}| \tag{2.5}$$

The ***Maximum Distance*** (MaxD) is a geometric method by Lee [35] that also aims at discovering the vertices of the simplex. The method starts by finding two vectors with special characteristics. The first two endmember candidates are the largest and smallest vector in the data. These vectors are the two first endmembers and the two initial corners of the simplex. Let us call these vectors v_1 and v_2 respectively. The next step is to construct the difference vector $v_{12} = v_1 - v_2$ and project all pixels of the image in the plane perpendicular to v_{12}. In that plane, the maximum distance between the projections of the pixel and the distance of the vector projected is found. The new selected endmember is the vector with maximum distance to the difference vector v_{12} calculated previously, let us call it v_3. In the next stage, the procedure is continued until the expected number of endmembers is reached. MaxD also assumes that pure pixels exist in the image (see Figure 2-9).
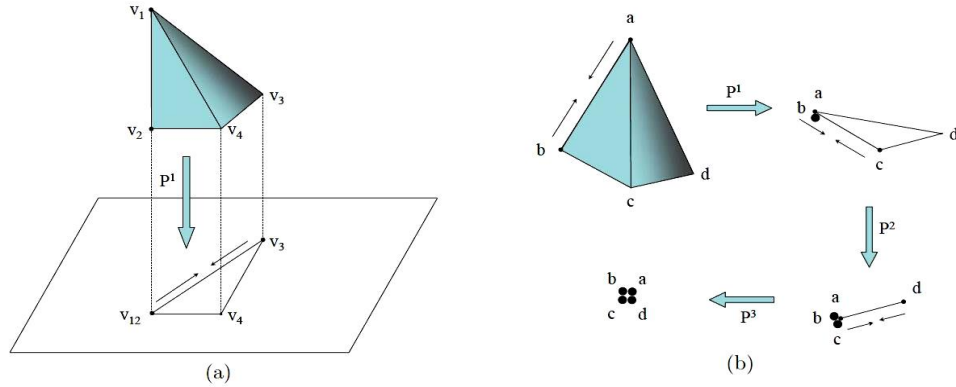
Figure 2-8. . Illustration the process to select the endmembers in the MaxD method [25].

The ***Vertex Component Analysis*** (VCA) is another geometric method proposed in [36]. This method assumes two things. First, endmembers are located at the corners of a convex hull and second a transformation of a convex hull is another convex hull. Like PPI, MaxD and N-FINDR algorithms, also assumes that the data have pure pixels. This algorithm projects data in the perpendicular direction to the subspace spanned by extracted endmembers repeatedly while the number of endmembers is not pre-determined. The next endmembers are the extremes of the projection.
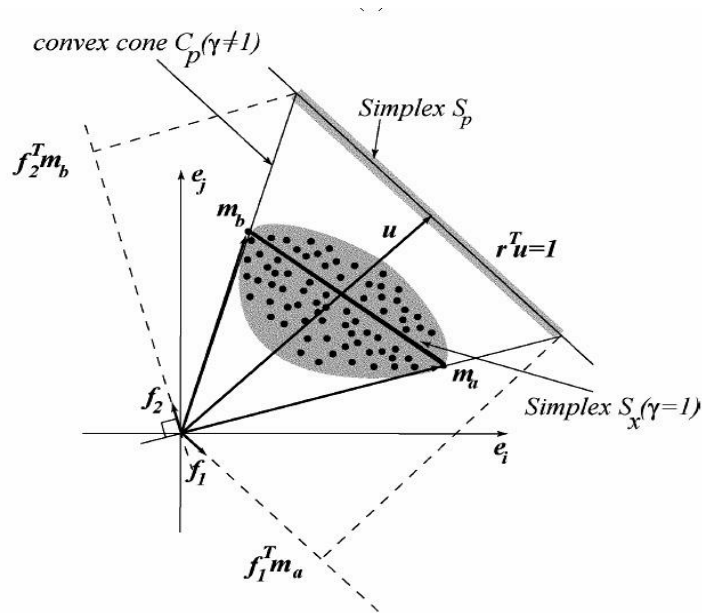
Figure 2-9 Illustration of the VCA algorithm [36].

The constrained ***Nonnegative Matrix Factorization*** (cNMF) is another geometric approach proposed in [32]. Given a hyperspectral image arranged as a non negative matrix $X \in \mathbb{R}_+^N$, the method cNMF finds two non-negative matrices $\mathbf{S}$ and $\mathbf{A}$ (Endmember and Abundance respectively), such that $\mathbf{X} \approx \mathbf{SA}$. Correspondingly, the lowest value of the number of endmembers p for which the factorization exists is called the positive rank [32] [33]. In other works [34] [35], the NMF has a geometric interpretation, related to finding the convex cone that contains the spectral data points. The NMF method does not assume pure pixel in hyperspectral image.

2.4.2 Parametric Approaches.

Geometric approaches are the most used techniques for unmixing. On the other hand, researchers have shown that not all hyperspectral images follow the convex hull model [21], and consequently geometric algorithms are not appropriate in these cases. Parametric methods in hyperspectral imagery for endmember extraction, include deterministic approaches and Bayesian approaches [37]. In deterministic approaches, endmembers and abundances are estimated without

assuming a prior distribution for them. Parametric algorithms model the endmembers and the abundances as random vector. Most assume Gaussian distributions for the pure constituents [7] preceded by the acquisition of enough statistics and representing each endmember as a single spectrum. Some of the most used parametric methods are summarized next.

The *Piece-Wise Convex Endmember* (PCE): The (PCE) algorithm is an unmixing technique based on the modeling of the spectral data as piece-wise convex. The endmembers are represented as Gaussian distributions, and the apriori distributions for the abundance vectors are polynomial functions [80]. This method divides the image data cloud in convex regions using the Dirichlet process to describe a hyperspectral image. Instead to using a single spectrum, PCE uses the endmember distribution detection procedure in each region to estimate each endmember as a distribution. Abundance vectors in PCE are sparse because each pixel only uses a subgroup of the endmembers [80].

The *Stochastic Mixing Model* (SMM): The SMM provides a technique for depicting the mixing of the pure image materials, and numerical variation in the endmembers. For instance, variability due to sensor noise and normal variability for pure materials [39]. Estimation of the parameters in SMM is determined basically by initialization of the algorithm, constraints, and class assignment. The statistical representation in SMM of hyperspectral imagery is better with respect to endmember class separation [39].

The approaches described previously only use the spectral information in the hyperspectral image. The next section describes several methods that include spatial information.

2.4.3 Spatial-Spectral Approaches.

Spatial information has been incorporated in the hyperspectral analysis using well-known image processing techniques such as morphological analysis, spatial kernels, and segmentation. Some spatial-spectral approaches are summarized below.

Automated Morphological Endmember Extraction Approach, (AMEE). Performs unsupervised determination of pure pixels and its extraction, using the spatial and spectral information. This method is based on mathematical morphology, a common image processing method that is applied to the spectral domain conserving its spatial features [40].

This method searches the endmembers using spatial kernels. The parameters that the algorithm uses are the maximum and minimun size of the spatial kernel (K). The kernel, with the minimun size, is moved through all the image finding the local neighorhoods around each pixel *x(x,y)* [40]. This method uses an ordering method based on the spectral purity index. The spectrally purest pixel ***d*** is related to the dilation operation. The spectrally mixed pixels ***e*** are related to the erosion operation. Dilation and erosion are defined for a pixel *x(x,y)* and a kernel K as:

$$d = argmax_{(s,t)\epsilon K}\{D(x(x + s, y + t), K)\} \tag{2.6}$$

$$e = argmax_{(s,t)\epsilon K}\{D(x(x - s, y - t), K)\} \tag{2.7}$$

where ***D*** denotes a distance metric given by:

$$D(g(x, y), K) = \sum_s \sum_t dist(g(x, y), g(s, t)) \qquad \forall (s, t) \in K \tag{2.8}$$

where ***dist()*** is the spectral angle distance.

In morphological operations, dilation expands regions and erosion shrinks regions. In this method, the dilation expand regions with pure pixels while erosion shrink regions with pure pixels. Figure 2-10 shows the effects of dilation and erosion in a hyperspectral image.
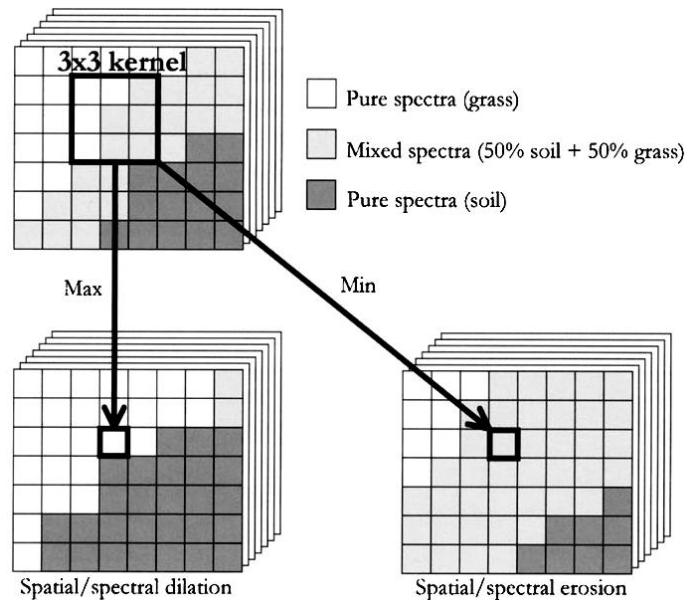
Figure 2-10. Local and global effects of applying spatial-spectral dilation and erosion operations to common hyperspectral image [40].

The dilation and erosion choose the purest pixel and the most mixed pixel. These correspond to the maximum and minimum respectively in a specific spatial neighborhood. The distance between them provides a value for the particular pixel that lets an assessment of the spectral purity of the pixel. This idea is incorporated, as a new quality measure defined as the morphological eccentricity index (MEI), which is the angle distance between the maximum and minimum element in the cluster [40].

The MEI is assigned to the maximun pixel in the neighborhood, and determines the capacity of this pixel to representate the other pixels at the cluster. The process is iterated for all pixels in the

image using clusters of increasing dimension until the maximun spatial kernel size is reached. The value of the MEI is changed at each iteration and a threshold is applied for unsupervised endmember selection. The number of endmembers corresponds to the number of pixels that are not eliminated from the MEI and select the most spectrally pure an the highly mixed pixels [40].

The *Spatial-Spectral Endmember Extraction Approach* (SSEE) [41] algorithm partitions (subsets) an image to enhance the spectral contrast of small contrast endmembers. Therefore, the potential for these endmembers to be designated as pure is improved. It is based on the statement that the detection of endmembers with high spectral contrast is easy with any convex approach, and it is more challenging to find the endmembers with low spectral contrast.

The SSEE algorithm includes three key steps. The application of singular value decomposition (SVD) is the first step to obtain a group of basic vectors that describe most of the spectral variances for the partitions in the scene. The second step is the projection of the data on the local basis vectors to obtain a group of posible nominee endmember pixels. In the third step, similar spectrally endmembers are averaged, and separating endmembers that are spectrally similar, but spatially independent [41]. In the SSEE, three essential parameters are necessary. First, the size of the pixel subset (20 pixels is suggested in [41]). Second, a threshold to group the largest eigenvectors (around 99%). Third, another threshold to select similar endmembers (around 1 degree for spectral angle distance) [41].

The *Spatial Adaptive Hyperspectral Unmixing Approach,* [42] performs spectral unmixing using a spatially adaptive approach, it divides an image in partitions (subsets) such that these partitions are used to identify local endmembers. Unmixing is accomplished at each pixel with endmembers recognized at local level, but the abundance maps are generated globally by grouping

27

the endmenbers obatained locally in particular groups. This method uses the MaxD algorithm [25] to determine the local endmembers. Abundances are estimated in each partition using local endmembers, and similar endmembers are clustered to determine global abundances. MaxD requires as input the number of endmembers. The algorithm estimates the number of endmembers using a methodology based on the Gram matrix [42].

This method begins by computing the volume of the convex hull formed by the endmembers in the corners extracted using MaxD. The volume of the convex hull is computed as the determinant of the local Gram matrix (G) expressed as:

$$G(x_k)_{i,j} = \langle (x_k - x_i), (x_k - x_j) \rangle \tag{2.9}$$

where $\langle \ \rangle$ denotes dot product, x_i, x_j, are two endmembers, and x_k is the mean.
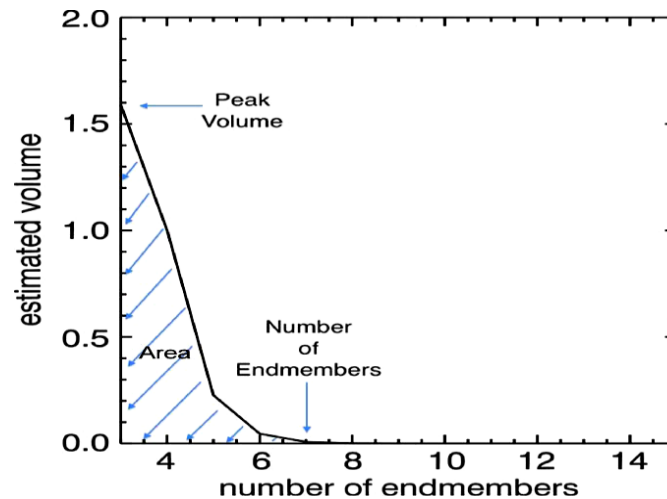
Figure 2-11. Data volume values as a function of the number of EMs from the Gram Matrix algorithm [42].

The convex hull volume is calculated for several number of endmembers (N). The graph of the function of the number of endmembers and the estimated volume is plotted and the number of

endmembers is selected as the point where the volume of the normalized cumulative function (NCF) is sufficiently close to zero (see Figure 2-11) [42].

The ***Spectral Endmember Extraction based on Multiscale Representation Approach,*** [43] takes advantage of the sampling operation used to build the coarse grids in a multigrid nonlinear diffussion method [44]. The endmember extraction method exploits the multigrid structure at the selected scale to determine the spectral endmembers. This technique extracts spectral signatures and spectral endmember classes from hyperspectral imagery in an unsupervised fashion. The spatial-spectral unmixing approach usees the multiscale representation to determine locally spectrally uniform regions and their representative spectra avoiding the explicit segmentation of the hyperspectral image.

A multiscale representation of the hyperspectral images is obtained using nonlinear diffusion. Then, spectral endmembers are automatically identified using multigrid methods to solve the diffusion partial differential equation. The multiscale representation and multigrids allow to avoid the use of spatial kernels. When the spectral endmembers are found, similar spectra are clustered to assemble spectral endmember classes, hence accounting for the spectral variability of the materials in the unmixing analysis, see Figure 2-12.
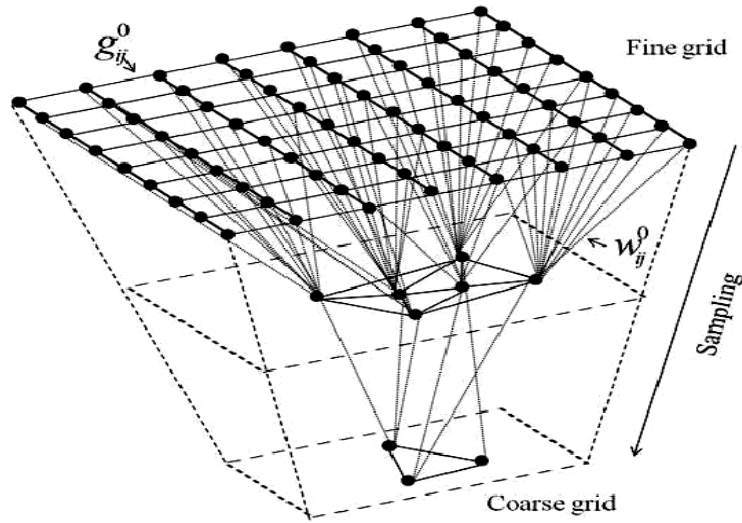
Figure 2-12. Construction of multigrid, where the vertices are the representative spectra in the HSI [43].

In the coarsest grid, the equation is solved exactly and then, the solution is propagated back to the finer grid. Each grid is represented by a graph. The vertices in the initial graph are the pixels in the original hyperspectral image and the initial edges are built using the closest neighbors. A sampling operation is responsible for building the next grid by selecting those vertices that represent a large number of vertices in the previous one. These vertices are selected such that they represent the vertices in the previous grids. Vertices in the coarsest grid represent the main spectral features of the image. The vertices in the coarsest grid (Figure 2-12) are used as the spectral endmembers. Most of the existing spatial-spectral endmember extraction techniques require the use of a spatial window. In contrast, this approach takes advantage of the properties of partial diferential equations and multigrid methods to select the spectral endmember without the need to define neighborhoods. This method only uses one of the smoothed images from the multiscale representation for spectral endmember extraction [43].

Other methods to determine the endmembers use clustering. For instance, K-means clustering is used to set the data and the cluster centroids are used as the endmembers. Notice that the clustering approach does not need the existence of pure pixels in the image [36]. The endmember determination approaches discussed in this section are not related to an optimization problem like Equation (2.3) since endmembers are determined separately from their abundances. The clustering approach deviates from the deterministic geometric model and treats endmembers as if they come from a distribution.

In [44]], a review of the different methods that incorporate spatial information at different stages in hyperspectral unmixing, either by preprocessing of the data, in the selection of spectral signatures or in the abundance estimation is presented. It is important to highlight Table 9 in this review where a comparison between different methods is presented.

2.5   Abundance Estimation Approaches.

Once the endmember signatures are determined, the next step is to estimate their abundances. Abundance estimation is the process of determining the abundances associated with the endmembers for each pixel in the image.

If the matrix of endmembers S is known or extracted using the approaches described in Section 2.3.2, the optimization problem (2.3) reduces to the abundance estimation problem. The cost function in (2.3) is separable in the abundance vectors for each pixel, so can be estimate the abundances for each pixel independently. The abundance estimation problem for a particular pixel is given by the constrained linear least squares problem:

$$\bar{a}_j = argmin_{a_{ij} \geq 0, \sum_{i=1}^{P} a_i = 1}, \left\| x_j - Sa_j \right\|_2^2 \tag{2.10}$$

31

The objective function in (2.10) and constraints are convex, consequently the solution is unique.

Several solution methods have been proposed in the literature to solve the AEP. The simplest solution presented is to completely ignore the constraints which leads to an unconstrained linear least squares (LLS) problem with direct solution given by [42].

$$\hat{a}_{STO} = (S^T S)^{-1} S^T x \tag{2.11}$$

The simplest restriction is the sum to one as a direct answer still exists for this case and is agreed by [42].

$$\hat{a}_{STO} = \hat{a}_{STO} + (S^T S)^{-1} \lambda 1_P \tag{2.12}$$

where

$$\lambda = \frac{1 - 1_P^T * \hat{a}_{ULS}}{1_P^T (S^T S)^{-1} 1_P} \tag{2.13}$$

A direct solution no longer exist when the positive constraints are enforced [42], [45]. The linear least squares problem with positive restrictions simply is denoted as the non-negative linear least squares problem (NNLS) for which Lawson and Hanson's algorithm [41] is the most frequently used algorithms. The NNLS algorithm uses the *Active Set Strategy* presented in [46]. The NNLS is a especial case of the Linear Least Square problem with Linear Inequality Constraints (LSI). The NNLS algorithm is described in detail by Lawson and Hanson [41] as well as its convergence properties.

To solve the NNLS algorithm, generally are used iterative procedures. For instance, NNLS applying to spectral unmixing with positive constraints, and as abundance estimation problem completely constrained, are shown in [45] and [47]. In [45], an approach for the fully constrained abundance estimation is presented, where the problem of unmixing is changed to a least distance problem. In [47], another method using quadratic penalty constraints is proposed..

2.5.1 Sparse Regression.

The sparse regression method is used when the amount of endmembers is larger than the number of bands. In a hyperspectral image, the pixels can be obtained as a linear combination of a subset of endmembers from a very big spectral library **S**. The unmixing issue can be posed as the search of the best subgroup of spectral signatures that represent each mixed pixel. Then the abundance vector converts a sparse vector [46]. The problem of sparse unmixing can be formulated as:

$$min_a\|a\|_0 \quad \text{subject to} \quad \|x - Sa\|_2 \leq \varepsilon, \quad a_i \geq 0, \sum a_i \leq 1 \qquad (2.14)$$

where $\| \quad \|_0$ is the zero-norm and indicate the number of elements nonzero, and ε is a threshold fitting error.

Another approach [49] proposes some procedures to solve the issue in (2.14), for instance orthogonal matching pursuit. Within the benefits of sparse unmixing are the estimation of the abundance is independently on the availability of pure pixels, and the capacity of an endmember extraction method.

In [54], a supervised unmixing algorithm based on dictionary learning is presented. Different from [49], they do not use spectral libraries. Given a set of training samples per class Y_i, the algorithm seeks a dictionary D that is used as the endmember matrix to solve the unmixing problem. The dictionaries D_i for each training sample set Y_i are learned solving the problem:

$$min_{X_i,D_i}\|X_i\|_1 \quad \text{subject to} \quad \|D_iX_i - Y_i\|_2 \leq \varepsilon, \qquad (2.15)$$

where X_i is the sparse representation, $\| \quad \|_1, \| \quad \|_2$ denote the ℓ_1 and ℓ_2 norms, and the ε is the error threshold. The unmixing problem is solved for each pixel using the dictionary $D = [D_1, D_2, ..., D_c]$ as the endmember matrix.

There are several algorithms to solve the sparse regression problem. For example, SUnSAL, Spectral Unmixing by Splitting and Augmented Lagragian, and C-SUnSAL, the constrained SUnSAL, are based on alternating direction method of multipliers [51]. SUnSAL solves the problem:

$$\hat{\boldsymbol{a}} = argmin \ \frac{1}{2}\|S\boldsymbol{a} - x\|_2^2 + \lambda\|\boldsymbol{a}\|_1 \ \text{subject to} \ 1^T\boldsymbol{a} = 1 \text{ and } \boldsymbol{a} \geq 0 \qquad (2.16)$$

where $\lambda \geq 0$ is a control parameter. C-SUnSAL solves:

$$\hat{\boldsymbol{a}} = argmin \ \|\boldsymbol{a}\|_1 \ \text{subject to} \quad \|S\boldsymbol{a} - x\|_2 \leq \varepsilon, \ 1^T\boldsymbol{a} = 1 \text{ and } \boldsymbol{a} \geq 0 \qquad (2.17)$$

2.6 Approaches to Deal with Endmember Variability in Unmixing Analysis.

The use of a single endmember spectra to represent an endmember class does not take into account the variability of spectral signatures across a scene. The endmember extraction methods depend on the capability to distinguish among pixels based on spectral characteristics only. Endmembers with high spectral contrast are simple to detect, while those with low spectral contrast are more difficult.

2.6.1 MESMA.

The *Multiple Endmember Spectral Mixture Analysis (MESMA)* works as a simple spectral mixture analysis (SSMA) method. In SSMA, a spectrum is represented as the sum of pure endmembers, weighted by the fraction of the endmember necessary to produce the mixture [53]. SSMA fails to account for pixel-scale variability and normal difference in the spectra of most materials. Consequently, SSMA exploits the potential of most remote sensing data sets for

separating materials, whereas producing small errors as a result of wrong type or number of endmembers used to unmix a pixel.

MESMA proposed by Roberts et al, in [53], was the first work to address endmember variability. Here, the authors introduced a technique based on iterative mixture analysis cycles. In this procedure, endmembers are allowed to change. MESMA allows various endmembers used for each material, eliminating the constraint to use fixed endmembers of simple spectral mixture analysis. In MESMA, the most-suitable model is selected as the one with the minimum root mean square error. MESMA has been successfully tested in forest, urban and extraterrestrial environments using both multispectral and hyperspectral and thermal imagery [54]. The ability of MESMA to take into account variable endmembers is confirmed after it is applied to vegetation cover mapping. It shows improved agreement with ground truth when related with SSMA.

In [54], Asner et all presented a Monte Carlo spectral unmixing model like MESMA. Take endmember combinations for each pixel that are calculated selecting spectra randomly from a spectral library. Monte Carlo spectral unmixing model is used to transfer ambiguity in endmember spectra to the last subpixel cover portion results.

The use of MESMA have been limited by some factors like a lack of easy to use software, and challenges in selecting endmembers to be used. MESMA typically is employed using hundreds of endmembers, resulting in significant challenges in interpretation and computation [54].

2.6.2 Subset Selection of Spectral Features.

The *Subset Selection of Spectral Features* [55] emphasized the probable decrease of the variability in spectral mixture analysis (SMA). The authors stipulated that a careful selection of wavelengths, robust against spectral variability (means that minimizing intra and maximizing

inter-class variability), could significantly improve subpixel quantification of fractional material cover, while the problem of computational complexity typical of iterative mixture cycles could be reduced. The approach was successfully tested in (semi-)arid ecosystems and conifer forests [55][56]. The applicability of this algorithm, depends entirely on the accessibility of high reliability short wave-infrared region spectral data (SWIR2 between 2,100 nm and 2,400 nm) and sensor operation. The method initially was focused for semi and arid locations take advantage of the little variability of constituents found in these environments. Not necessarily accurate for other varieties of landscapes depending on the spatial, spectral, and temporal complexity of the endmembers present in the landscapes.

Techniques in subset selection for SMA based on residual analysis [57] [58] and feature extraction approaches using Principal Component Analysis (PCA) and Discrete Cosine Transform (DCT) [59] have been used. These procedures have the extra advantage of incorporating only unlinked spectral data in SMA. Results from [59] revealed that though these approaches of feature extraction decrease the dimensionality of spectral data, did not help to improve abundance estimation results.

2.6.3 Spectral Weighting and Transformations.

The *Spectral Weighting and Transformations* is an approach to diminish the effect of endmember variability in SMA. Normally, all spectral bands are equally weighted in SMA. Weighted Spectral Mixture Analysis (wSMA) [60], highlights less sensitive bands to variability giving them a higher weight in SMA [60].

Generally characteristics with high spectral reflectance will contribute more in the SMA solution, when compared with the bands of low reflectance. For instance, mixed signals with

vegetation and soil will appear similar effects with the endmember variability over the entire NIR spectrum and the high reflectance dominates in the inverse model [56].

Therefore this method seeks to highlight some bands less sensitive to the variability of endmembers giving them larger weight, because if this is not done when we make the calculation of abundance, it would highlight only those with more variability [56].

Another approach that is taken into account to reduce the effect of variability in the endmembers is using transforms. This is, the data of the original spectral reflectance change their information through transformations before being used in the SMA process. In [54], the concept of linked spectrum is used to increase the separability of endmembers. The reflectance of a spectral band (band tied) is subtracted from the other bands. The resulting spectrum of the difference is called linked spectrum to certain band. Another transformation used is the method described in [61], called normalized SMA and the transformation involves dividing all spectra by the average of all of them, which reduces the variability in the brightness of the endmembers and then performs the process of analysis. Another transformation mentioned in [62] is the derivative of spectral unmixing (DSU) in which the second derivative of endmember is used as input to SMA. This enhances the variability between classes and reduces the variability within the same class. Also, the first derivative of spectral endmember has been used in [63] to estimate partial abundances with similar spectra. A transformation in [56] uses the combination of the first derivative with the original reflectance for SMA processing.

2.6.4 Endmembers Bundles.

The concept of *Endmembers Bundles* (see Figure 2-14) was introduced in [64] and [65]. Is another method which also takes into account the variability of the endmembers in SMA process.

37

Similar analysis like Principal Component Analysis (PCA) using eigenvectors, a bundles of vectors are recognized and selected to represent the endmembers. A sequence using linear programming is then used to calculate the maximum, minimum and the mean, abundance for each endmember. Iterative mixture methods give a theoretical background for understanding the endmember variability.
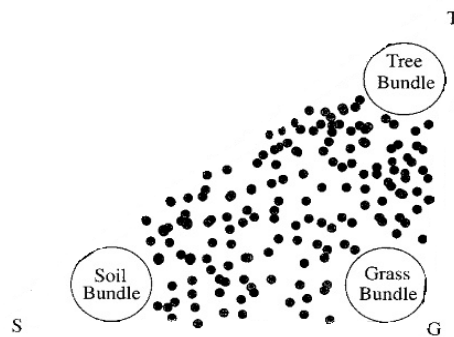
Figure 2-12. Concept of Endmember Bundles. [64]

The endmember extraction in [49] works by evaluating an image in subgroups (bundles), to enhance the spectral contrast of low contrast endmembers, hence improving the probability for these endmembers to be extracted. Endmember are extracted from each tile and merge at a global level to develop an accurate description of the natural landscape under study.

2.7   Clustering Algorithms.

Once spectral endmembers are extracted, a simple form to extract spectral endmember classes is by using clustering methods. Clustering is widely used in the areas of pattern recognition, statistical analysis, data mining and used in hyperspectral imaging for applications in segmentation, classification and unmixing (e.g. [41, 42, 43, 53, 64]). These works have used

clustering over the full image. In our approach, clustering analysis is performed in the set of spectral endmembers. Some unmixing methods have employed clustering to form sets of endmember classes, see [41] and [64].

In this section, a brief review of clustering techniques is presented. There are many references dedicated to clustering [28], [29], [30], [31]. One of the most difficult problems in clustering analysis is the determination of the number of clusters that here corresponds to the number of spectral endmember classes. For this task, validity indexes are used. They are metrics to assess the clusters obtained from different configuration of clustering methods (e.g. different number of clusters) [28, 31, 32]. Validity indexes were used in [43] to determine the number of endmember classes.

Clustering helps us to divides a collection of endmembers into several subsets (clusters), based on some similarity criterion [28], [29], [30], and the partition clustering seeks a n-partition, $C = \{C_1, C_2, \ldots, C_n\}$, of a dataset $S = \{s_1, s_2, \ldots, s_m\}$, with $n \leq m$, such that each sample of S belongs to one single partition C_i .

Clustering methods can be hierarchical, partitional or based in graph theory. A large number of these algorithms perform clustering using a pair wise distance matrix instead of the dataset and a satisfactory selection of the similarity metric is necessary.

Cluster analysis consist of several steps [29]. First, feature extraction techniques can be used to improve the representation of the data. Second, a similarity matrix is calculated using similarity measures. The clustering algorithm performs the separation of the samples into useful subsets. Finally, clustering results are assessed to determine how well the algorithm finds the hidden data structure. This can be done using validity indexes. This section presents a brief summary of what is necessary to perform these steps.

Similarity metrics are used to compare two spectral signatures and establishing how close they are, The more used metrics are the Euclidian Distance (ED), the Spectral Angle measure (SAM), the Spectral Correlation measure, and the Spectral Information Divergence [85], [86], [87]. Clustering algorithm techniques, can be classified as *hierarchical*, *partitional* and *graph theory* approaches.

The *hierarchical approach* makes a group of nested partitions. This type of clustering do not require the number of clusters. The dendrogram can be broken at any level obtaining different partitions of the data (see example in Figure 2-15). The hierarchical algorithms can be divisive or agglomerative. Divisive approaches start with a single cluster that include all samples and perform division operations. This is computationally expensive, and the agglomerative one starts with several clusters formed with one single sample, and then successive merge operations are performed using the similarity matrix until a single cluster is obtained with all samples.
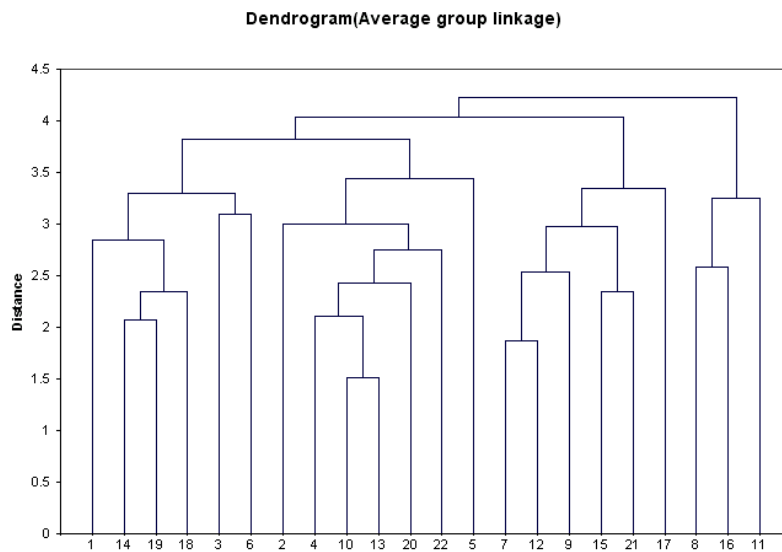
Figure 2-13. Example of Dendrogram for hierarchical clustering [85].

To perform the merge operations, several criteria are used. The single linkage uses as the minimum distance between all pairs of samples from clusters. The complete linkage uses the maximum

distance between all pairs of samples from the clusters. The average linkage uses the distance between centroids as the distance between clusters [29]. All the three methods are available in the statistics toolbox in MATLAB used in this work [30].

The ***partitional approach*** minimizes some criterion function to find the optimal partition of the data. The most common partitional algorithms are based on the square error criterion [29], [30]. The most used partitional algorithm is k-means clustering that starts with a random partition and iteratively reassigns the samples to the clusters according to the similarity between the sample and the centroid of the cluster until convergence. This method is available in the statistic toolbox in MATLAB as well.

The ***graph based approach*** uses a similarity graph $G = (V, E)$, where each vertex represents a sample and the edges are built by the connection of very similar vertices. The problem of clustering can be viewed as the task of partitioning the graph G such that the connection between subgraphs are weak and the connection within subgraphs are strong [88]. In this approach, the edges are built using the ϵ-neighborhood graph that connects all points whose similarity are smaller than ϵ, or using the k-nearest neighbor graph that connects each vertex with its k closest vertices. The other type of graph is the fully connected graph that connects all points using a function (frequently used the Gaussian similarity function $e^{-\|x_i - x_j\|^2 / 2\sigma^2}$) that hold the local neighborhood relations.

2.7.1 Validity Indexes.

Validity indexes are necessary to verify the validity of the clusters obtained. Indexes are metrics that allow the assessment of clustering results obtained by different methods. The validity indexes can be *"external"* that employ a priori information of the dataset, such as previous partitions, to assess the performance of clustering algorithms. They can be *"internal"* that do not depend on a priori information and measure how well a clustering technique recovers the structure

of the data. *"Relative indexes"* are metrics to compare different clustering algorithms or configuration of algorithms in order to determine which one provides the best results [30, 32, 92].

Some examples of validity indexes are mentioned next. Dunn's index [94] uses the fact that well-formed and separated clusters should present large distances between clusters and small diameters. Dunn's index employs the minimum distance among all pairs of trials within two clusters as the distance among clusters. Davies and Bouldin index [95] selects the number of clusters by using the average similarity of each cluster with its most similar cluster. The similarity between clusters is a function of a dispersion measure and a distance measure. Kim et al index [31] uses the mean intra-cluster distance and the over-partition measure function to determine the optimal number of clusters.

Validity Indexes are used in [43] to determine the number of cluster. We will also use the Davies and Bouldin index as in [43] to determine the number of endmember classes.

2.8 Segmentation to find Boundaries in the image.

This section presents a brief review as how the spatial variations in an image can help detect different type of materials in the image. The use of spatial variations is related directly with different textures found in a scene. To detect the different textures we need to detect the boundaries between different materials.

To detect boundaries from different textures in an image, we need to divide the image by sectors (neighborhoods) of different sizes and then calculate some measure of homogeneity to determine the degree of local variation. This is used to determine if this sector belong to the same material or mixed materials. As examples of metrics, there are the Angular second moment, the correlation,

and the entropy [74]. If we can detect the texture features in the image, we can provide a useful information to discriminate the classes in the image.

The segmentation helps to detect different textures in the image and help also to detect the boundaries between objects. For this process, two methods has been examined, conjunctive and disjunctive [74].

2.8.1 Conjunctive Approach.

The conjunctive methods begins using a very little division of the image and join contiguous components together to form uniform objects. In this approach, object seeking involve cell selection and cells merging (see Figure 2-16) [74].
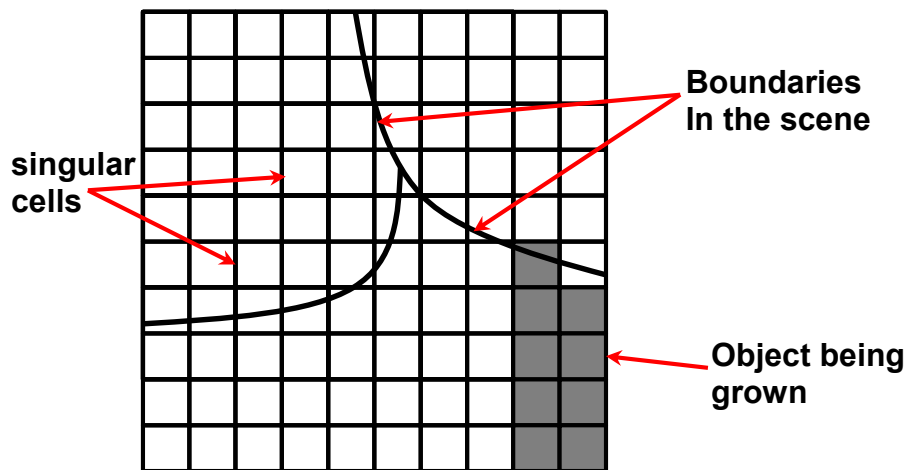
Figure 2-14. Example of Conjunctive Approach [74].

This method consists of testing a cell with a minor check of numerical uniformity. If it conforms, check the neighbor on the left, if it conforms also use a numerical check to decide if the two neighbor have similar statistics. Thus then, the second cell is merged with the first [74]. The process is repeated iteratively until the test fails showing an edge in the image and then a

homogeneous region (object) is created. This segmentation process would be supervised or unsupervised, wherein information of the classes would be used.

2.8.2 Disjunctive Approach.

The Disjunctive methods starts with a very simple partition (the entire image) then split the divisions until each elements fulfills the wanted numerical uniformity criterion (see Figure 2-17) [74].
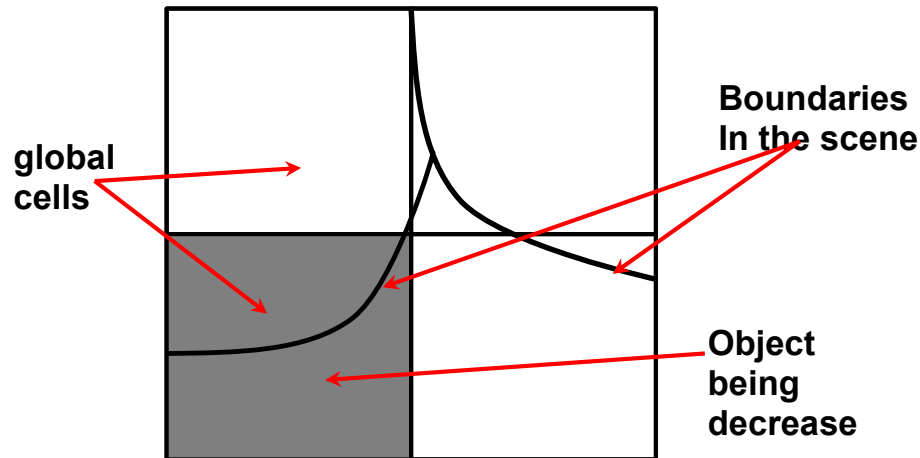
Figure 2-15. Example of Disjunctive Approach [74].

In this approach, the scene is divided iteratively and for each piece a global statistical homogeneous index is calculated and compared with the index of the entire scene. If the values are less than the global, partitions are stopped. If the value is larger than the global, this tile is divided in four parts until the homogeneous regions are found in the image [74]. The quadtree partitioning used in sacNMF can be catalogue as a disjunctive approach.

2.9 Non Negative Matrix Factorization.

This section presents an introduction to the non-negative matrix factorization (NMF) method and its use for spectral unmixing analysis.

2.9.1 Overview of NMF.

The nonnegative matrix factorization (NMF), is a suitable procedure in approaching large dimensional data where the data are composed of positive component. Lee and Seung in [47], suggested the use of the NMF procedure to locate a group of simple functions to characterize image data, where simple functions permit the detection and classification of the object being imaged. Several papers have discussed NMF methods and uses in different areas with positive data values [12], [13], [62].

Recent works in NMF like [76] Esser, Shapiro et al, show a method for dimensionality reduction using a convex model for NMF, also, in [77] Wang et al, show a complete review about NMF where the NMF algorithms can be categorized in four groups the basic, constrained, structured and generalized NMF.

To formulate the Nonnegative Matrix Factorization problem, we need first to introduce some notation. The set $R_+ = [0, \infty)$is named set of positive real numbers. Let $Z_+ = 1, 2, 3, ...$ be the set of positive integers, for $n \in Z_+$, let $Z_n = 1, ..., n$. Symbolize the set of natural numbers N = 0, 1, 2, ... Symbolized by R_+^k the set of k-tuples of positive real numbers. The set $R_+^{n \times m}$ is the set of $n \times m$ positive real matrices.

Definition. (Nonnegative Matrix Factorization): Given a nonnegative matrix $X \in R_+^{n \times m}$, the standard NMF problematic is to find two reduced-dimensional matrices $S \in R_+^{m \times p}$ and $A \in R_+^{p \times n}$ such that

$$X = SA \tag{2-18}$$

Definition. (Positive Rank) Let $X \in R_+^{n \times m}$ for $m, n \in Z_+$. If $X = 0$, the positive rank of X is defined to be 0. The positive rank of the matrix $X \neq 0$ is defined as the least integer $p \in Z_+$ for which there exists a factorization given by Equation (2-18). The equivalent factorization is named minimal positive matrix factorization.

The NMF problem is to determine the positive rank of a positive matrix and the corresponding minimal factorization [63]. Finding and exact solution for NMF is an open problem in linear algebra.

Clearly p cannot be less than the positive rank of X, but in several circumstances even larger values of p do not promise that an exact NMF exists. Hence, it is relevant to contemplate the NMF approximation problem where, given X and p, one minimizes distance between X and SA with respect to positive matrices S and A. There are different norms that can be used in the minimization process. Typically the Frobenious norm is used and the approximate positive matrix factorization can be written as:

Approximate Positive Matrix Factorization: Given a positive matrix $X \in R_+^{n \times m}$ and $p \in Z_+$, the approximate PMF problem is to find two new reduced dimensional matrices $S \in R_+^{m \times p}$ and $A \in R_+^{p \times n}$ such that

$$\widehat{S}\widehat{A} = \text{argmin}_{S_{ij} \geq 0, A_{ij} \geq 0} \|X - SA\| \tag{2-19}$$

Typically the Frobenious norm is used. This optimization problem always has solution [64].

2.9.2 Computational Approaches for approximate NMF.

The NMF can be tied back to 1994, when Paatero published his paper [63] introducing it. This work was prior to the work of Lee and Seung [43] on the Nonnegative Matrix Factorization. Since the work of Lee and Seung [43], a lot of work has focused on the analysis and application of NMF in science, engineering, and other fields. The NMF problem has been formulated in alternate ways based on the application and the corresponding constraints. In [65], NMF was used for document clustering. In [14], NMF was used for quick retrieval of constituent spectra in magnetic resonance and chemical shift imaging of the brain. In [66], NMF algorithms can be divided into three different general. In [12], Lee and Seung Multiplicative updating rules are mentioned. This class uses either the mean squared error or the divergence objective functions. In both cases, the positive rank p is assumed known. An algorithm developed in [12] to solve (2-20) is summarized.

An alternative to the Frobenious norm as a distance metric in (2-19) is the divergence as follow

$$\widehat{S}\ \widehat{A}\ = \text{argmin}_{S \geq 0, A \geq 0}\ D(X||SA) \tag{2-20}$$

where

$$D(X||SA) = \sum_{ij}\left(X_{ij}log\frac{X_{ij}}{(SA)_{ij}} - X_{ij} + (SA)_{ij}\right) \tag{2-21}$$

The corresponding multiplicative updating rules are given in [12] to solve (2-21). These algorithms are the reference point against which the newer algorithms are compared. The main contribution of [12] was the development of the updating rules that converge to a local minima.

The second class of NMF algorithms are founded on gradient descent methods. This class of algorithms update the **S** and **A** matrices in each iteration. The step-size parameters can be chosen in different ways. Several algorithms first set the step size values to, n = 1, then keep changing it by dividing by 2 until a descent step is achieved. This is known as a step halving method [46]. This

type of algorithms does not guarantee that S and A entries to be nonnegative. A projection step is added [67], [46], [65], [68], [69] to overcome negative value entries. The projection step updates the elements of **S** and **A** by setting all the negative elements to 0. Mathematically, this can be written as

$$A_{ij}^{k+1} = \max\{0, A_{ij}^{k} - \eta_{A_{ij}} \frac{\partial J}{\partial A_{ij}}\} \tag{2-23}$$

The last class of NMF algorithms are the alternating least squares (ALS) class. This class of algorithms alternates between two least squares steps. These algorithms were used first by Paatero [63]. The algorithms take advantage of the fact that the problem has a bilinear structure. That is for fixed **A** the problem is linear in **S**, and for fixed **S** the problem is linear in **A**.

This ALS algorithm structure at each iteration is summarized in the following steps:

1. Solve for **A** using $(\mathbf{S^TS})\mathbf{A} = \mathbf{S^TX}$.
2. Set all negative elements in **A** to 0. (This is a projection step.)
3. Solve for S using $(\mathbf{AA^T})\mathbf{S^T} = \mathbf{AX^T}$.
4. Set all negative elements in **S** to 0. (This is a projection step.)

The algorithm keeps alternating between the previous steps until convergence is achieved. These algorithms are different from the multiplicative ones in that they are more flexible in changing the path to the fixed point. The multiplicative algorithms have the drawback that once an element in **S** or **A** becomes 0, it stays at 0. This means that once the algorithm starts heading down a path towards a fixed point, it must continue even if it is a poor path [43]. The ALS algorithms can be very fast and requires less work than other NMF algorithms.

.

Several modifications and improvements to NMF have been introduced in recent years, For example, in [70], a matrix factorization that conforms the geometric data structure is presented. In [71], speed enhancement for NMF is accomplished by an algorithm based on alternating least squares framework.

2.9.3 Hierarchical NMF.

The NMF factorizes a non-negative data matrix $\mathbf{X}$ into two non-negative factors $\mathbf{X} \approx \mathbf{SA}$ such that the columns of S often represent meaningful parts. NMF tries to find the convex hull that encloses the entire data set, as show in Figure 2-18(a). The HCH-NMF [73] searches for the intrinsic structure of the data to extract a hierarchy basis vectors that better describe the data as shown in Figure 2-18 (b)-(c).

This internal structure of the convex-hull NMF (HCH-NMF) [73], is a hierarchical NMF approach that automatically adapts to the low intrinsic dimensionality of data (see Figure 2-18).

<div align="center">a)   b)   c)</div>
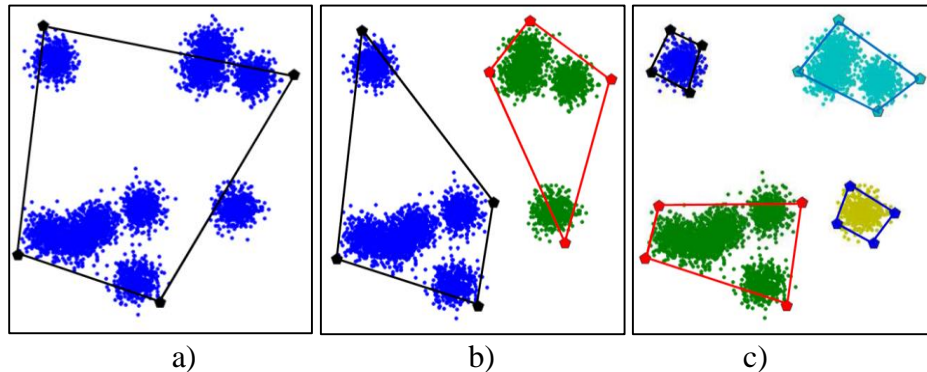
Figure 2-16. Example of HCH-NMF for different basic vectors, 4, 8, and 16 respectively [67].

The HCH-NMF is described in [67] and is based on hierarchical decomposition (of pair a distance *D*) of $\mathbb{R}^D$ in the form of a tree. That is, it begins with an empty tree and repeatedly search for the best test for a node according to any splitting criterion. For each split, the procedure is recursively

<div align="center">49</div>

applied. The splitting is stopped if a minimum number of samples is reached or the variance in one node is small enough.

$$J = \|S - SAH^T\|^2 \tag{2-24}$$

where $S \in \mathbb{R}^{m \times n}$, $A \in \mathbb{R}^{n \times k}$, $X = SA$, $X \in \mathbb{R}^{m \times k}$ and $H \in \mathbb{R}^{n \times k}$.

2.9.4 Non Negative Matrix Factorization for Unmixing.

The NMF is used as a base for the improvement of a constrained non-negative matrix factorization (cNMF) algorithm for unmixing in [14]. In [47], a multiplicative technique that includes a constraint on the smallest amplitude of the recuperated spectra to allow the algorithm to take in hand observations with negative values assuming they arise due to noise is presented. This algorithm does not impose the sum-to-one constraint on the abundances as required by the linear mixing model. By requiring non-negativity for both the endmembers and the weights, NMF is able to produce results which should still have physical interpretation. Another important aspect of NMF is the optimal use of error estimates. NMF computes the solution by minimizing the least squares error of the fit weighted with the error estimates [70].

Other methods based in NMF are used in Hyperspectral Unmixing. In [83] [90], for instance, the Constrained Nonnegative Matrix Factorization. The topography variability of the real data may cause in error solution when we use only the sum-to-one constraint on the abundances. Therefore, in these papers using two characteristics in hyperspectral data the piece wise smoothness and that the abundance are sparseness, to generate a discontinuity adaptive model. In [84], an approach using similar constraints as [83], but only taking in account the abundance separation is presented. In [85], an approach based on sparsity constraint using a L½ regularizer, which induces the sparsity is presented.

Other recent methods presented in [78] [86], improve the NMF method. The first proposes to use the dissimilarity endmember constraint (EDC), which can measure the difference between endmembers. And the second, called the Coupled Nonnegative Matrix Factorization, uses the fusion of data of low spatial resolution in hyperspectral data and high spatial resolution in multispectral data, finding new data that improve de spatial and spectral resolution in the resulting image.

2.10 Hyperspectral Image Data Sets

The data used in the experiments presented later is described here.

2.10.1 AVIRIS, A.P. Hill Image.

This image was collected using the Airborne Visible and Infrared Imaging Spectrometer (AVIRIS) with ground truth data over Fort A. P. Hill, Virginia USA. These images were captured in November 1999 and September 2001, at a spatial resolution of ~3.5 meters.   This ground truth involves a qualitative description of land cover types organized in a geographical information system (GIS) [88]. The image has 512×540 pixels with 224 spectral bands. The spectral library was made by the ground truth data to classify great zones of unvarying land cover type.   They defined endmembers for 14 land cover types: summer deciduous forest, loblolly pine, three examples of autumn deciduous forest, green agricultural fields, three types of soil agricultural fields, generic road, river water, shaded vegetation, grass field, and gravel [88]. An RGB color composite and the classification map are shown in Figure 2-17 (the bands used for the color composite are R 635.19nm (28), G 548.09nm (19), B 461.04 (10)).
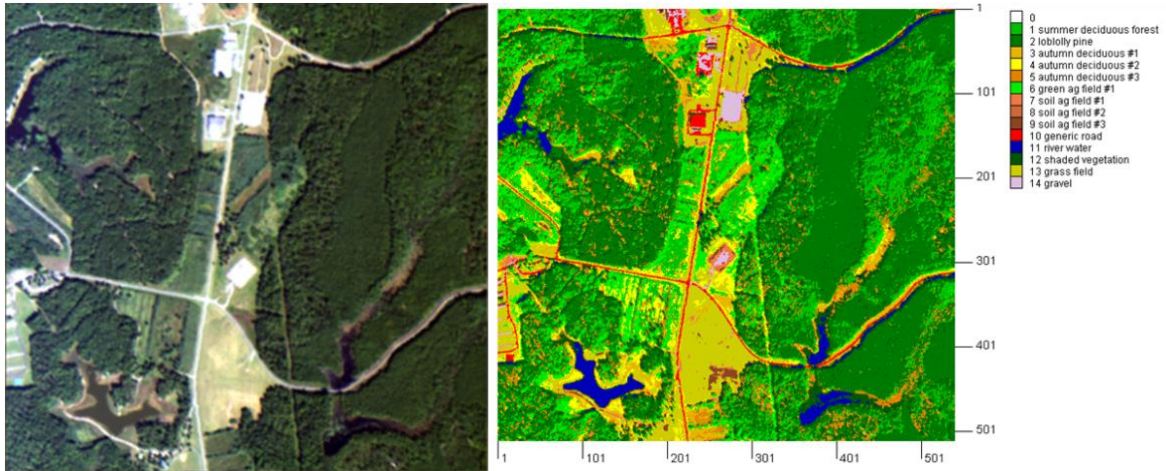
Figure 2-17. RGB (28, 19, 10 bands) image of an AVIRIS Hypercube Fort A. P. Hill Virginia data collect and Ground truth [88].

2.10.2 AVIRIS, Indian Pines Image.

Another important data set is the AVIRIS image captured in NW Indian Pines Test site in an agricultural zone of Northern Indiana. The image has 145×145 pixels with 220 spectral bands and covers about two-thirds agricultural parcel and one-third forest and other materials. "The soybean and corn crops in the image are in early growth stages and, thus, have only about a 5% crop cover" [80], [81]. The left over ground zone is soil covered with residue from the earlier crop. "The no till, min till, and clean till labels indicate the amount of previous crop residue remaining" [80]. No till matches to a large amount of residue, min till has a moderate quantity, and clean till has a minimal quantity of residue [80]. Figure 2-20 shows RGB (R 635.19nm (28), G 548.09nm (19), B 461.04 (10)) composite and a classification map for the area. The 49% of the pixels in the scene have ground truth statistics [81].

Figure 2-18. Color composite and Classification map for AVIRIS image from Indian Pines,
https://engineering.purdue.edu/~biehl/MultiSpec/hyperspectral.html **[79]**

2.10.3 Cuprite Nevada Image.

This is another data set collected with the AVIRIS sensor. Cuprite contains two acid-sulfate hydrothermal alteration centers spanning highway 95 in southwestern Nevada [82]. "Cuprite spectral mineral abundance maps of the area show two elliptical zonation patterns. The western center is zoned progressively inward from sericite, to halloysite-dickite, kaolinite, Na-alunite, through K-alunite with halloysite in the interior. The eastern center is zoned inward from halloysite to kaolinite, intermediate alunite, through K-alunite, with a central core of siliceous sinter" [82]. Classification map for Cuprite shown in Figure 2-19 is USGS [82] derived from an AVIRIS image collected in 1995.

The data is available online [http://aviris.jpl.nasa.gov/data/free_data.html], and http://speclab.cr.usgs.gov/ and it corresponds with a flight conducted in 1995. This image has 224 bands and a spatial resolution of 20 meters. Figure 2-21 presents a RGB composite (bands 28 (635.19 nm), 19 (548.09 nm) and 10 (461.04 nm)) of the image used to evaluate the proposed

approach. A classification map from the USGS is used as references here [82]. Figure 2-21 shows the map which was derived from the AVIRIS image collected in 1995 using the spectral region from 2000 to 2500 nm. The map in Figure 2-21 includes 25 classes. This image is selected to evaluate the proposed approach since it is a complex landscape with small spectral uniform regions and several materials. Several materials within Cuprite do not meet the main assumption of the proposed algorithm of local uniformity. Then, this image allows to understand the limitations of the proposed approach.
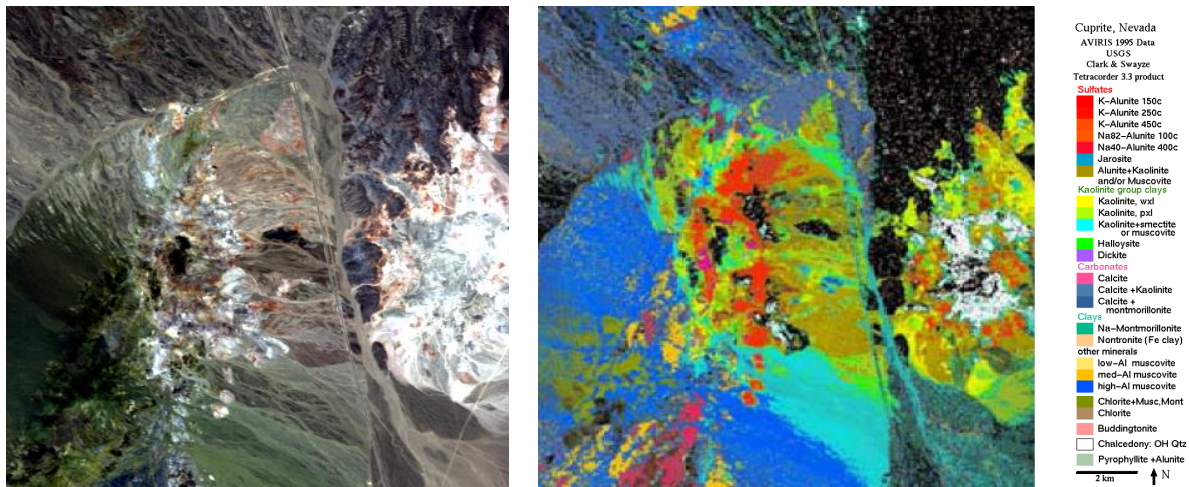
Figure 2-19. AVIRIS Cuprite Nevada and Classification map for Cuprite [80].

2.10.4 Guanica Forest PR Image.

The Guánica Dry Forest is a tropical dry forest designated as a UNESCO man and Biosphere Reserve in 1981 [17]. Located in southwestern Puerto Rico, it is the cores site of the Atlantic Geotropical Domain of the US National Ecological Observatory Network (NEON). AISA images collected over the forest in December of 2007 are used in this work. These images consists of 128 spectral bands from 397 nm to 995 nm and are part of the hyperspectral remote sensing mission conducted over Southwestern Puerto Rico [102]. The data was collected at two different

spatial resolutions: 1 and 4 meters. The available AISA data cover the complete forest. The scene shown in Figure 2-17 is used in this work to study spatial resolution effects. The image with 1 meter spatial resolution has 396 x 600 pixels, and the image with 4 meters has 99 x 150 pixels. This subset was selected because a detailed description of this region found in [100]. RGB composites were built using bands 54 (639 nm), 35 (550 nm), and 15 (459 nm). There are no classification maps for the forest. However, the Guanica Forest has been widely studied by faculty and students at the University of Puerto Rico. Santos [17] presents a description of the region used in this study based on field work conducted in the area in 2009 (Figure 2-23). The Guanica image is composed of tall and low vegetation, with a region covered by grass. Two types of roads are in the scene: pavement road, and dirt road. A building is located near the center of the scene.

a)   b)
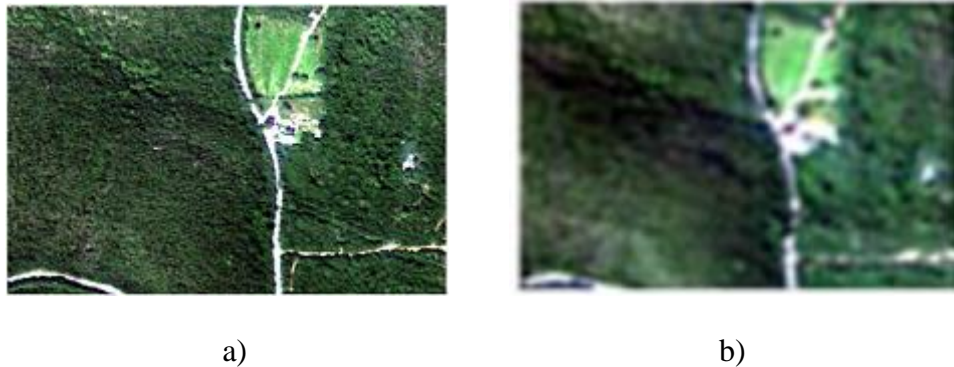
Figure 2-20. Guanica Dry Forest PR. a) 1 meter resolution, b) 4 meters resolution.

Figure 2-21. Ground truth Guanica Dry Forest PR.

2.11 Summary.

This chapter presents the state of the art of different methods for hyperspectral unmixing analysis that use the spatial-spectral information. Also shows a summary of the state of the art of the methods used in each stage of the proposed sacNMF approach.

Most of the spatial-spectral algorithms found in the literature use kernels into their procedures. Therefore, the obtained unmixing results depend on the size of these windows. On the other hand, some algorithm employs unsupervised clustering techniques to determine spectrally uniform regions where endmember are extracted avoiding to use these kernels. However, similarly to most of existing spatial-spectral methods, algorithms do not use the spatial information for the estimation of the number of endmembers. In addition, does not perform the endmember extraction. This is a pre-processing step that determines a set of spectra that are passed to a spectral-only technique for endmember extraction. Therefore, the development of new algorithms that use the

spatial and spectral information of hyperspectral imagery for the combined estimation of the number of endmembers and their spectral signatures that do not use windows is essential.

Finally, this chapter described the hyperspectral imagery and ground truth used for algorithm testing and validation.

3. EXPLORATORY DATA ANALYSIS TO UNDERSTAND SPATIAL-SPECTRAL INTERACTIONS.

The basic assumption on the linear unmixing model is that the pixels are in the convex hull of the cone with the endmembers at its vertices are illustrated in Figure 2-7. Real hyperspectral data in general does not follow the structure as shown in Figure 3-2. Here we use exploratory data analysis to analyze how spatial information can be used to extract homogeneous regions in the image. Several spectral unmixing algorithms look for a single convex region to depict a hyperspectral scene for a particular set of endmembers. A convex region can be defined in Euclidian space as if for every pair of points within the data cloud, every point on the straight line segment that joins the pair of points is also within the data cloud. For instance a solid cube is convex data cloud.

This section proposes an approach to perform unsupervised unmixing demonstrating how the spatial information help to capture the relationship between the grade of uniformity of the clusters, and the convex regions in the image data set. The effect of splitting the image using quadtree region partitioning helps us to obtain homogeneous regions.

3.1   Data Cloud Image Representation.

In this section we demonstrate how the spatial information help to capture the relationship between the degree of uniformity and the convex regions in the image data cloud. To visualize the data, the hyperspectral image is projected into its first three principal components. The first 3 principal components of this image explain 98% of the total variability. 3D scatter plots are generated using visualization capabilities of MATLAB.
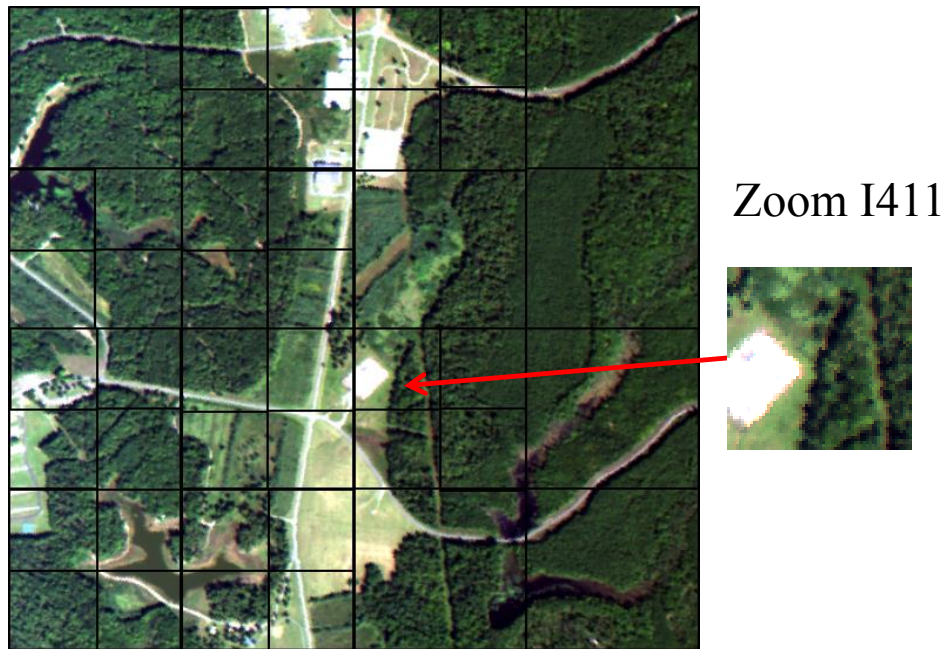
Figure 3-1. RGB Composite for the AVIRIS AP Hill image showing the tile Zoom I411 used in this exercise.
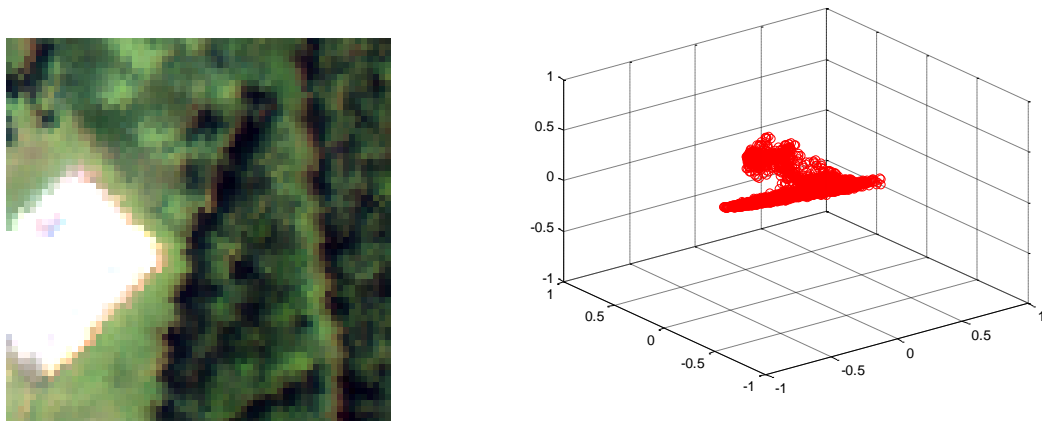
Figure 3-2. PC1 PC2 PC3 Scatterplot of Zoom I411 for the APHill image.

The image example used here is Zoom I411. It was selected because there are several materials in the tile that, because of spatial constraints, cannot mix, resulting in the non-convex data cloud shown in Figure 3-2.

The hypothesis formulated is that by decomposition the image into homogeneous regions we can obtain data cloud with convex for that is very advantageous for the linear mixing analysis.

3.1.1 Manually Regions Partitioning Image.

The image tile in Figure 3-2 is partitioned manually into four quadrants to analyze the behavior of the data in the scatterplot for each region in the scene. Figure 3-3 shows the tiles for the partitions.

a)

Zoom I4111 - Zoom I4112 - Zoom I4113 - Zoom I4114

b)
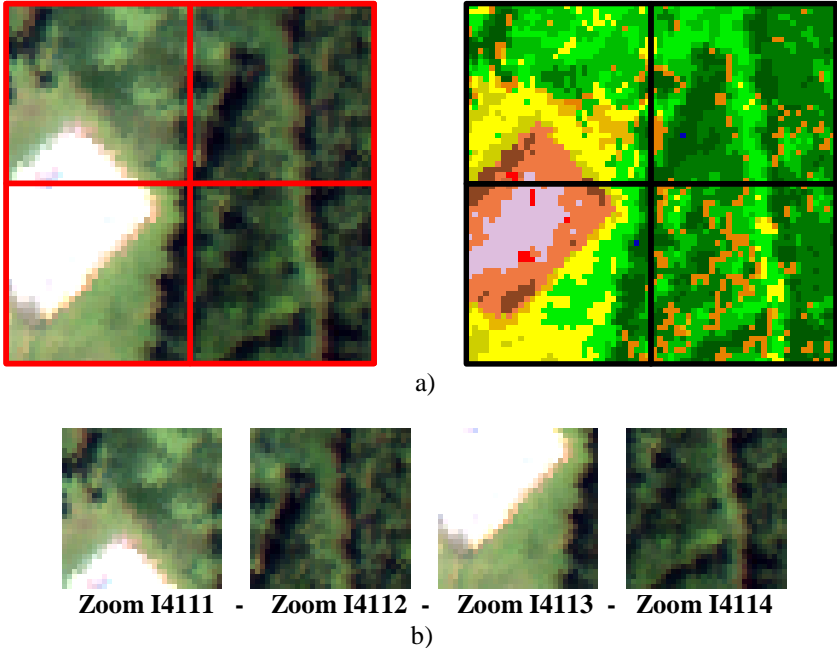
Figure 3-3 Partitions of Zoom I411 of AP Hill image a) the Zoom I411 and the ground truth images b) the partitions in the Zoom I411.

These partitions will be analyzed separately to see the behavior of the cloud of data for each division with respect to the full image data cloud in Figure 3-2.

The next figures show the data cloud for the different partitions for the Zoom I411.
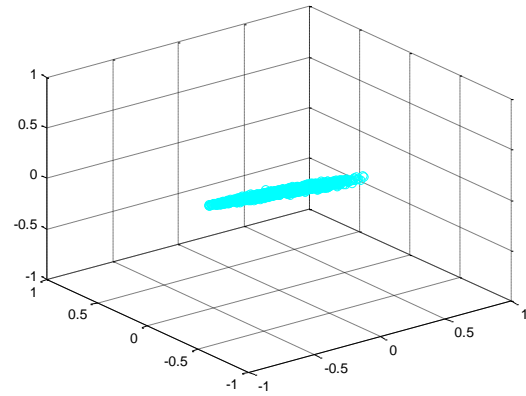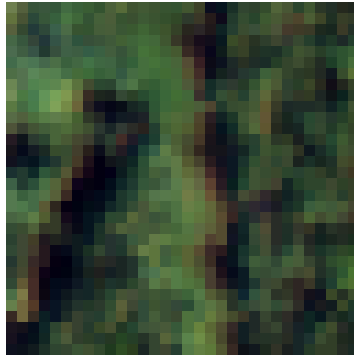
Figure 3-4 PC1 PC2 PC3 Scatterplot for of Zoom I4112 of AP Hill.
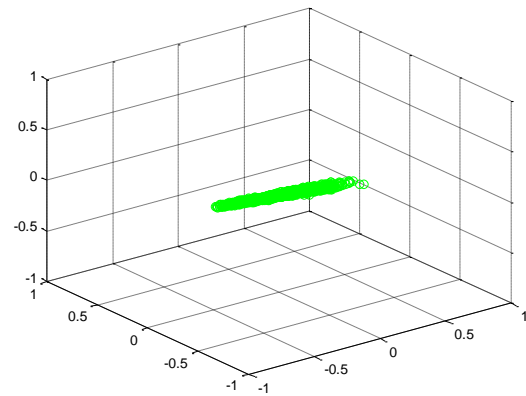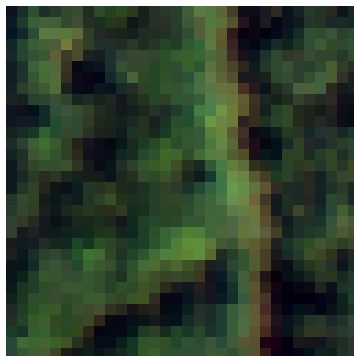
Figure 3-5 PC1 PC2 PC3 Scatterplot for of Zoom I4114 of AP Hill.
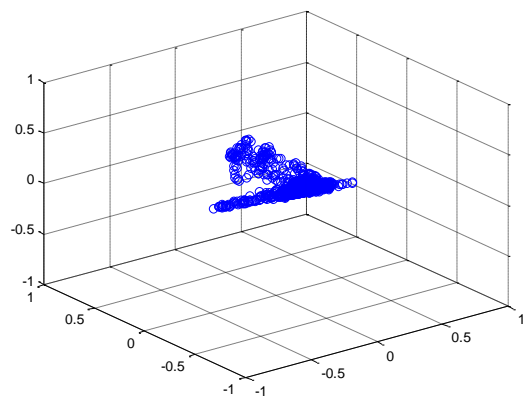
Figure 3-6 PC1 PC2 PC3 Scatterplot for of Zoom I4111 of APHill.

61
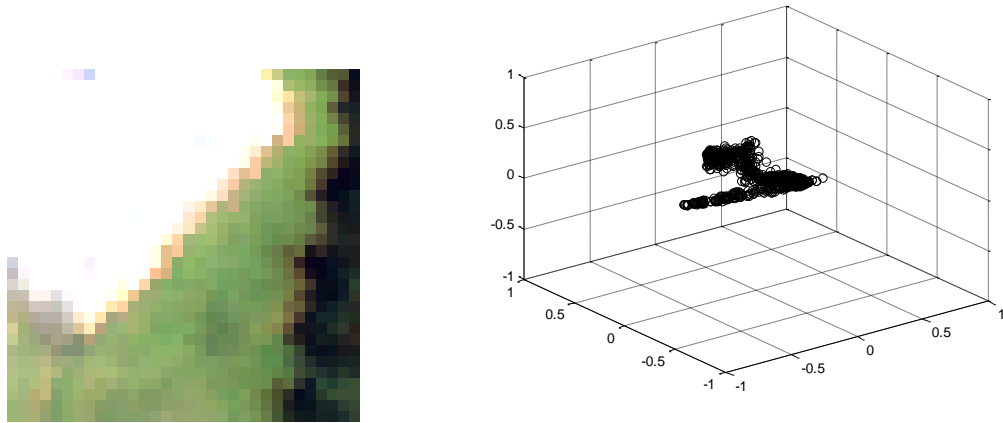
Figure 3-7 PC1 PC2 PC3 Scatterplot for of Zoom I4113 of AP Hill.

As shown in Figures 3-4 and 3-5, although there are still distinguishable classes on the image, its data cloud is convex. The data cloud shows an elongated convex form that represent 2 endmembers which clearly facilitates endmember extraction and unmixing. Figures 3-6 and 3-7 include the buildings class and still shows a non convex data cloud. Notice that the image is not a uniform subtile of the image.

Then we repeat the procedure again, Zoom I4111 is partitioned into four quadrants as shown in Figure 3-8. Notice that the tiles show different levels of uniformity. The corresponding data clouds for each subtile are shown in Figures 3-9 to 3-12. Notice that again uniform tiles lead to convex data clouds. Figures 3-11 and 3-12 show non uniform tiles and, hence non convex data clouds.
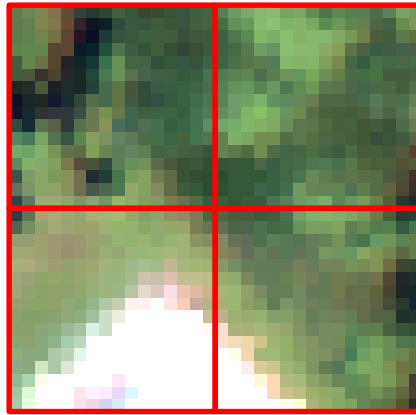
a)
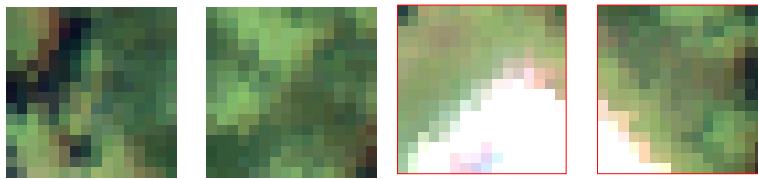
Zoom I41111 - Zoom I41112 - Zoom I41113 - Zoom I41114

b)

Figure 3-8 Partitions for Zoom I4111 of AP Hill .
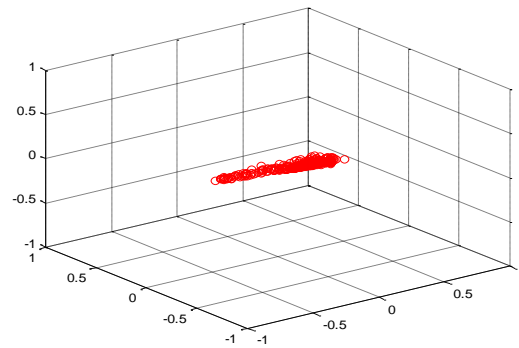
Figure 3-9 PC1 PC2 PC3 Scatterplot for Zoom I41111 of AP Hill.
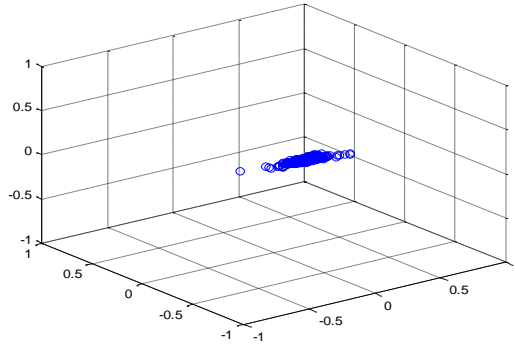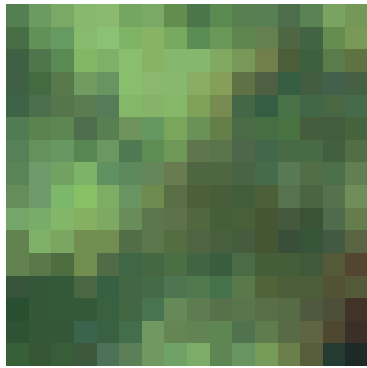
Figure 3-10 PC1 PC2 PC3 Scatterplot for Zoom I41112 of AP Hill.
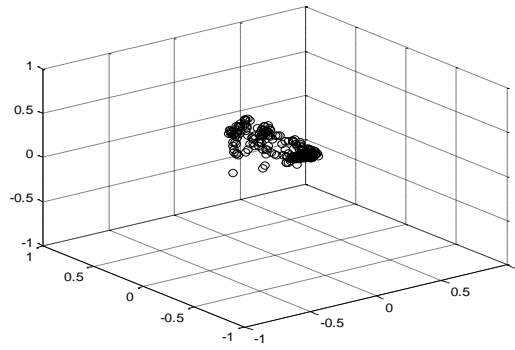
Figure 3-11 PC1 PC2 PC3 Scatterplot for Zoom I41113 of AP Hill.
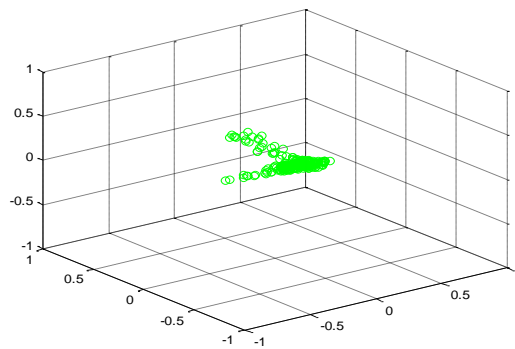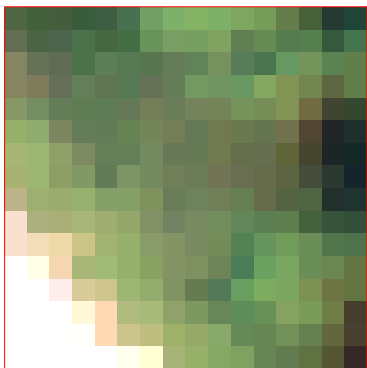
Figure 3-12 PC1 PC2 PC3 Scatterplot for Zoom I41114 of AP Hill.

If we repeat the analysis with the other image tiles similar results are obtained. Uniform regions map to convex sub-clouds in the main data cloud, and tiles with multiple materials have non convex clouds associated with them. These results suggest that by decomposing the image in

homogeneous regions, we partition its data cloud into piece wise convex regions. This is the main motivation behind image partitioning using quadtree, presented in the next chapter.

3.2   Summary.

In this chapter we used exploratory analysis to understand the relation between the spatial domain information and data cloud structure. We saw experimentally that by partitioning the image in homogeneous regions we can decompose the data cloud in piece wise convex regions. We can then apply linear unmixing to these regions and easily extract endmembers for different homogeneous tiles in the image.

Decomposition of the image into uniform regions is the main idea behind the quadtree image decomposition method described in the next chapter. By decomposing the image into uniform regions and extracting endmembers for each tile using cNMF we make the cNMF sensitive to spatial information.

4. INCORPORATING SPATIAL INFORMATION IN HYPERSPECTRAL UNMIXING

In Chapter 3, we illustrated how partitioning the image into homogeneous regions may help to extract the convex pieces of the data cloud corresponding to mixing materials in the image. In this chapter, we show how to decompose a hyperspectral image in homogeneous tiles using quadtree partitioning. This section shows how to perform hyperspectral unmixing using local information and merge them at a global level to develop an accurate description of the scene under study.

4.1   Quadtree Image Representation.

In the proposed unmixing algorithm, the hyperspectral image is partitioned in spectrally homogeneous regions using quadtree region partitioning. The effect of different spectral variability metrics in the splitting of the image using quadtree partitioning is studied in this chapter. Experimental results using the AVIRIS Fort AP Hill and NW Indian Pines images show that the Shannon entropy (see equation 4.5 and section 5.2 for this calculate) produces the image partitioning with the fewest classes per tile.

4.1.1 Quadtree Region Partitioning.

The unmixing approach described in [103] analyzes a scene by partitioning it in subsets of tiles such that the spectral contrast of endmembers with respect to its neighbors is increased. This improves the potential for these endmembers to be selected by an endmember extraction algorithm. A partition approach is also followed here, however with the assumption that, within a tile, endmember variability will be small and endmembers can be represented by a single spectral

signature. Once the local endmembers are extracted, they are clustered to extract endmember classes that provide a more accurate description of endmember variability and of the scene under study.

Different types of data can be represented by quadtree data structures [95]. The most common quadtree is "region quadtree" where the image is partitioned in regions or quadrants according to a given split criterion, e.g. color homogeneity [94], or percent (10%) of the difference between the maximum and minimum grayscale values in the quadrant image, or the level of the tree or different indices as shown later. The quadtree helps us to represent images at different levels of homogeneity. Figure 4-1 shows two examples for binary images and their region quadtree representation.
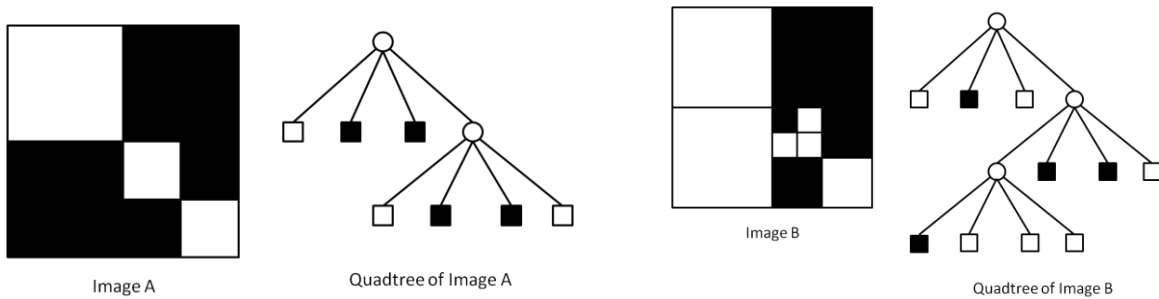
Figure 4-1. Region Quadtree Representation [95].

Quadtree is an unbalanced spatial data structure built by recursive divisions of space in four equally sized quadrants. In this data structure, the tree has a root node that corresponds to the entire image to analyze. Depending of the partitioning criterion selected, the image is partitioned in four equal parts, which appear as different levels on the quadtree that contains the different partitions of the image. If the image does not conform to the selected partitioning criterion, then the root had four descendant nodes representing the first level of the quadtree image [103].

The partition criterion establishes when the algorithm stops the partitioning and which divisions are leafs in the quadtree. A node is a leaf when its corresponding image quadrant conforms to the partition criterion, otherwise, the node is internal. Specifically, in the case of binary images (see Figure 4-1), internal nodes are characterized as gray. If k is the number of internal nodes in the image quadtree, a non empty quadtree has $4k+1$ nodes and $3k+1$ leaf nodes. The quadtree is called a full quadtree if all leaves appear at the same level [96]. A full balance quadtree with h levels (h $\geq$ 1), contains:

$$\sum_{i=1}^{h} 4^{i-1} = \frac{4^h - 1}{3} \ \ nodes \tag{4.1}$$

The cardinal directions in the quadtree, left-right and up-down, following NW (0), NE (1), SW (2), SE (3) directions [96], see Figure 4-2 is used to reference the tile in the process.

First four quadrant identification

Sub-quadrant Identification
for quadrant 00
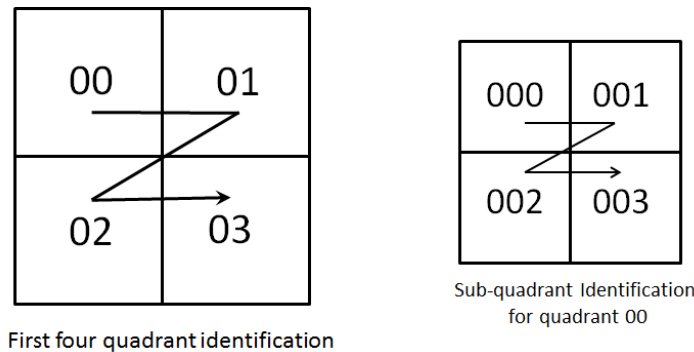
Figure 4-2 Example of the Identifier used in cardinal directions.

In addition, quadtree region partitioning can be used to handle positional data of image characteristics for color image segmentation and for shape and feature detection [97]. A number of approaches use quadtree region partitioning to store image characteristics. In these methods, every image is represented by a quadtree having a fixed number of levels, frequently a full three level quadtree. Each quadtree node represents an image quadrant by storing its characteristics [98].

4.1.2 Partition Criterion.

The region quadtree decomposition approach is, typically, a method that segments an image in four regions repeatedly every time, until a partition stopping criterion is met. There are several partition stopping criterion proposed in the literature. For instance, color, texture homogeneity of an image quadrant, or a maximal number of feature points in the quadrant. This process is called quadtree decomposition, or quadtree segmentation [80].

Specifically, for Hyperspectral images, we explore different spectral variability metrics to use in a split stopping criterion for quadtree partitioning. Some published works use the entropy of the hyperspectral image and the correlation in spectral dimension as stopping criterion in quadtree partitioning [96].

Here, we show how different metrics used as stopping criterion split the image using quadtree region partitioning. The metrics used or partition criteria are mentioned bellow.
The ***mean distance from the spectral centroid*** [96,97] using the spectral centroid help us to calculate it. Another useful metric is the ***norm of the spectral centroid*** [97] [95], the ***mean of all values in the image*** (across all pixels and all bands) [98] and finally the ***norm of Shannon entropy***.

4.1.3 Applications of Quadtree in Hyperspectral Images.

The quadtree data structure is used in numerous approaches with the aim of capturing the spatial composition of small features in an image [103].

Quadtree Decomposition for Hyperspectral Imagery is an adaptive hierarchical division approach based on quadtree partitioning and a modified minimum distance classifier. This method adapts to the local features of the hyperspectral data, in which each cluster center, the mean vector, is recursively update to follow the local characteristics. The approach does not need to adopt the

distribution type of each region, and reduces substantially the computational cost because the splitting decision logic is simple [103].

The algorithm decomposes spatially and recursively the hyperspectral image until they are divided into rectangular uniform regions in which the spectral bands values curve (Euclidian distance) are similar to one another. The cost function consists of the Euclidian distance measured between the featured vector of each component type and the input vector and the spatial similarity term. The spectral band values of the selected band areas are be close for each component to form the feature vector [103].

Compression of Hyperspectral Images based on Quadtree Partitioning. Uses quadtree partitioning to acquire the mean image and the important correlation can be eliminated by subtracting the mean image from original image [104].

In this approach, the image representation using quadtrees is applied to compression of a hyperspectral image. This is done taking into account the spatial correlation of a band image. A spectral image is divided into a mean image and a difference image. The key of the compression algorithm is how to get the mean of the image with minimum data. This algorithm takes 4x4 blocks of the image without overlapping between blocks and arrange them as quadtree structure. This method uses two threshold to works, the correlation coefficient for Hyperspectral image, and the value of the Entropy for the entire image and the different blocks obtained during the process.

4.2 Metrics for Hyperspectral Imagery.

The quadtree decomposition or quadtree segmentation described previously is based on a criterion that measures image variability in the sub-image. For Hyperspectral images, we explore different

spectral variability metrics to use as partition stopping criterion for quadtree partitioning. Some published works use the entropy of the hyperspectral image and the correlation in spectral dimensions as stopping criterion in quadtree partitioning [84].

4.2.1 Spectral Variability Metrics.

In this section, we present the metrics studied as stopping criterion to split the image using quadtree region partitioning. The metrics used were:

*M_1: **The Mean distance from the spectral centroid**.* The local spectral heterogeneity of an area can be measured from the size of the clouds of pixels in the spectral space [96] [97].

The spectral centroid is defined by:

$$C_i = \frac{1}{N}\sum_{j=1}^{N} X_j \tag{4.2}$$

and the mean distance from the spectral centroid is:

$$M_1 = \frac{1}{N}\sum_{j=1}^{N} d(X_j, C) \tag{4.3}$$

where B = number of bands, N = number of pixel in the image, X_j = the spectral signature of the *j-th* pixel, and $d(X_j, C)$ = is the Euclidian distance between X_j and C.

*M_2: **The Mean of all values in the image**.* The mean of all values in the image across all pixels and all bands [97][95]:

$$M_2 = \frac{1}{N}\sum_{j=1}^{N} \sum_{i=1}^{B} X_j(i) \tag{4.4}$$

where B = number of bands, N = number of pixel in the image, $X_j(i)$ = the value of j-th pixel in i-th band.

M_3: _The Shannon entropy_. comes from field data and was calculated using the expression (4.5) [98]:

$$M_3 = Shannon(X) = -\sum_{i=1}^{Alpha} p(x_i)\log(p(x_i)) \qquad (4.5)$$

where X is the given image and $p(x_i)$ is the ratio between the number of pixels with sample x_i in the specific area, and total number of pixels in the image (see section 5.2).

4.3 Experiments Comparing Quadtree Region Partition Metrics.

4.3.1 Experiments with Fort AP Hill data.

In this section, we compare quadtree partitioning using the three metrics mentioned previously. The partitioning were obtained using two stopping criteria, the minimum level of the quadtree partition (64th part), or spectral variability in the tile lower than 90% of the global variability [90].
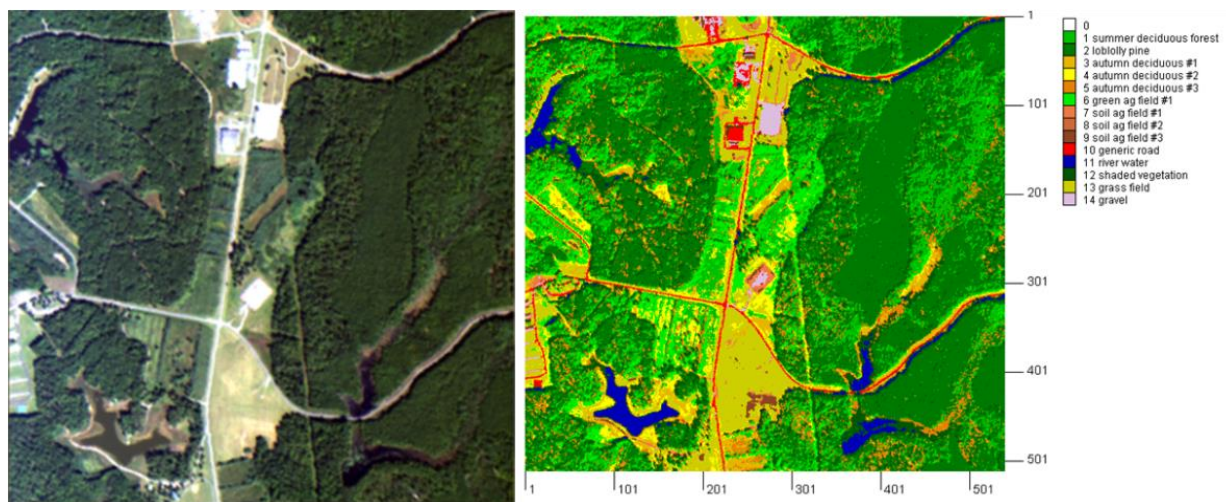
Figure 4-3. True color composite and classification map for AVIRIS image from Fort A.P. Hill AFB, VA [91].

72

The experiments were performed with the Fort A.P. Hill AVIRIS image (see Figure 4-3). This thematic map in Figure 4-3 is used later on to evaluate the proposed unmixing approach. Here we used the number of information classes in a tile as a measure of the spectral variability in the tile.

4.3.1.1   Partition and Classes resulting by different Metrics.

The partitions resulting from using the *mean distance from the spectral centroid (M1)* the *mean of all values in the image (M2)* and the *Shannon entropy (M3)*, can be seen in the Figures 4-4, 4-5 and 4-6 respectively.

Figure 4-4. Partitions using the mean distance from spectral centroid with global index M1 = 7.3298.

Figure 4-6. Partitions using norm of the Shannon Entropy with global index M3 = 9.7011.

Figure 4-7 shows the resulting partitioning for each criteria and it also shows the number of classes in each title. The average number of classes per tile for the mean distance from spectral centroid, the mean distance of all values in the image, and the norm of the Shannon entropy are 6.2, 5.1, and 4.3 respectively. We use the number of classes as an indicator of variability in the tiles. Shannon entropy resulted in the image partitioning with the lowest variability.
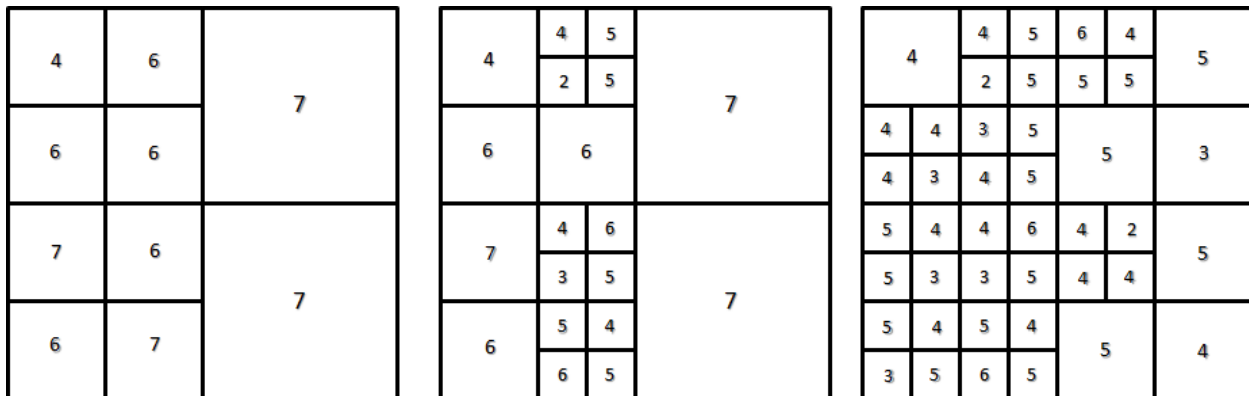
a) Average: 6.2   b) Average: 5.1   c) Average: 4.3

Figure 4-7. Number of classes per tile using: a) the mean distance from spectral centroid, b) the mean of all values in the image, c) the norm of the Shannon Entropy.

For the same three metrics, the resulting partitions for the Indian Pines image can be seen in Figure 4-8. The ground truth classification map for Indian Pines is show in Figure 2-8.

|a) M_5= 9.534|b) $M_3 = 0.426$|c) $M_1 = 6.835$|
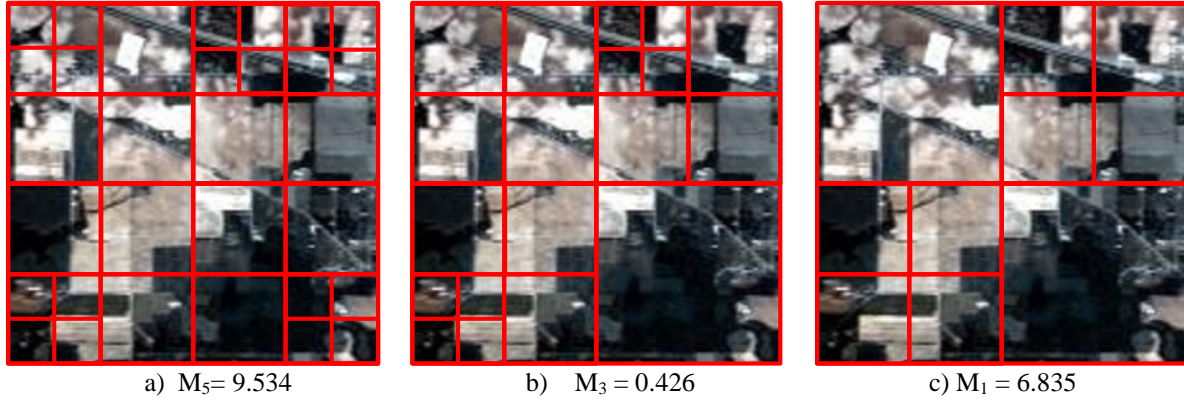
Figure 4-8. Number of divisions using: a) the norm of the Shannon Entropy, b) the mean of all values in the image, c) the mean distance from spectral centroid, from the AVIRIS Indian Pines data set.

The average number of classes per tile for the mean distance from spectral centroid, the mean distance of all values in the image, and the norm of the Shannon entropy are 5.9, 4.16, and 3.93 respectively. We use the number of classes as an indicator of variability in the tiles. Again the norm of the Shannon entropy resulted in the image partitioning with the lowest variability.

|a) Average: 3.93|b) Average: 4.16|c) Average: 5.9|
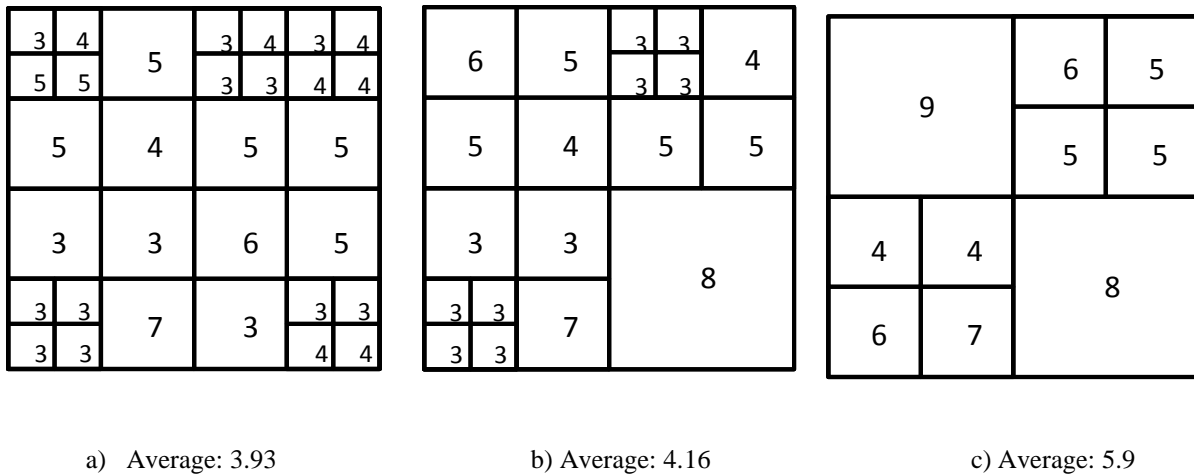
Figure 4-9. Number of classes per tile using: a) the norm of the Shannon Entropy, b) the mean of all values in the image, c) the mean distance from spectral centroid, from the AVIRIS Indian Pines data set.

4.3.1.2   Spectral Classes resulting by different Metrics.

The number of endmember classes was determined using validity indexes used in [43] and the hierarchical clustering use the Spectral Angle measure (SAM), and the Spectral Correlation measure as similarity metric to grouping the endmembers [85],[86]. The information classes are shown in the classification map for AP Hill shown in Figure 4-3 are 14. The number of endmember found for each tile varies between 4 and 7. The number of endmember was estimate using the fitting error curve which will be discussed in chapter 5. The total number of spectral endmembers for each of these three metrics were 49, 82 and 139 respectively.

When the endmembers from the tiles were clustered, 8, 10 and 11 endmember classes were identified using the hierarchical clustering method the number of the endmember classes found using the partition based of Shannon entropy was the closest to the number of classes from the classification map in Figure 4-3.

a).Summer deciduous forest.   b).Loblolly pine.   c).Autumn deciduous #2.   d). Soil agfield #1.

e). Generic Road.   f). River Water.   h). Grass field.   i). Gravel.
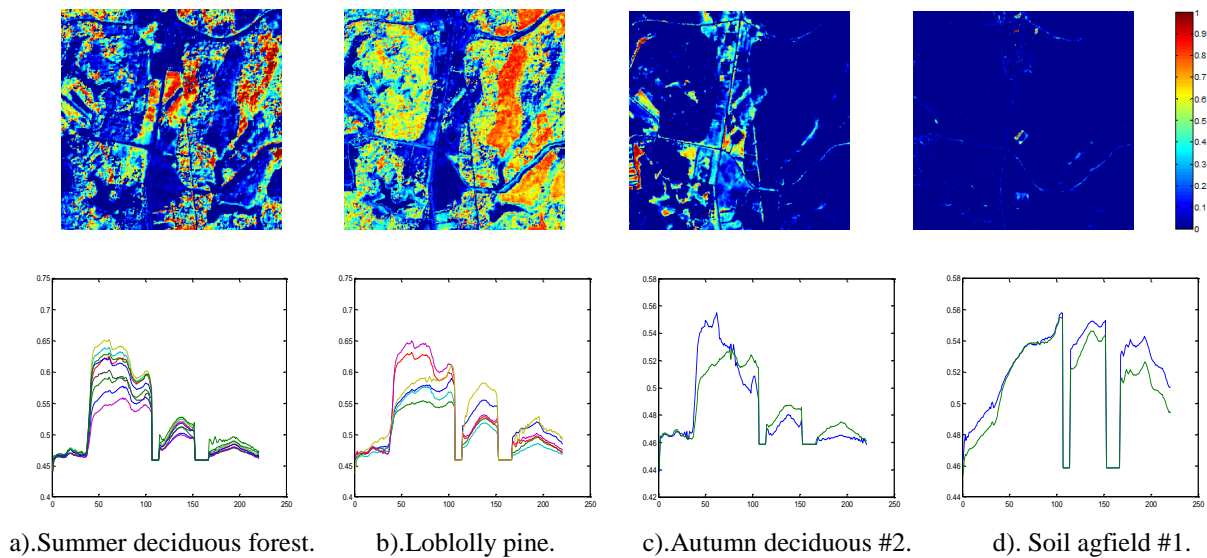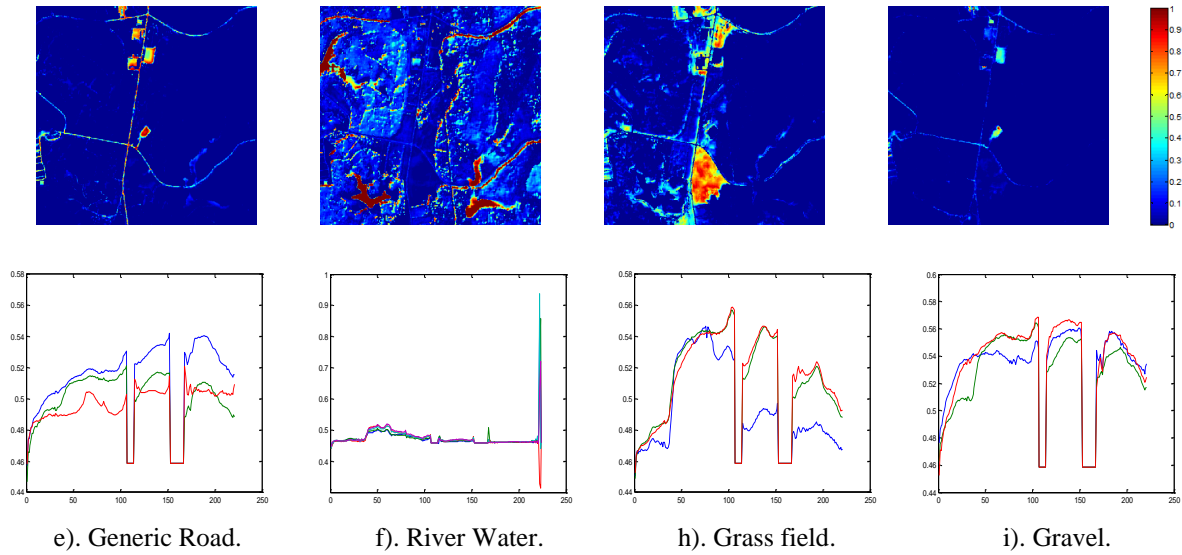
Figure 4-10. Endmember Classes resulting from the partitioning using the mean distance from spectral centroid for the AVIRIS APHill data set.

The thinner partition of the image allows identification of more endmember classes than what is possible by applying NMF to the full image by itself. The global analysis is showed in section 4.5 where were obtained 6 endmembers applying the NMF to the full image, mixing classes that appear separate in the local analysis.

a). Summer deciduous forest.   b). Loblolly pine.   c). Autumn deciduous #1.   d). Autumn deciduous #2**.**

e). Autumn deciduous #3. f). Soil agfield #3. g). Generic Road. h). 11. River water.

i). Grass field. j). Gravel.
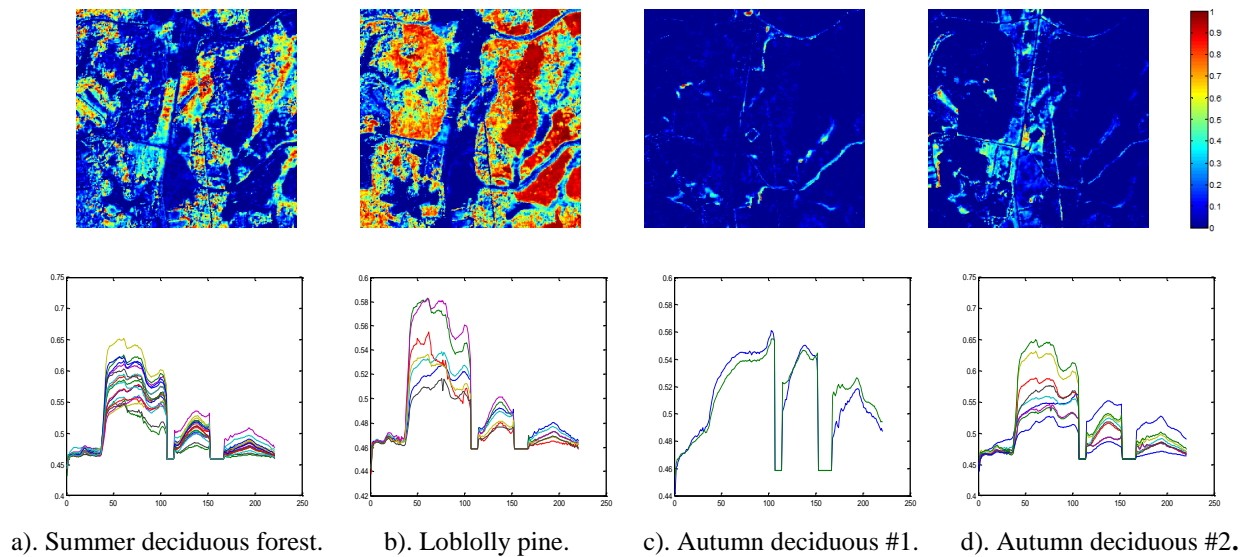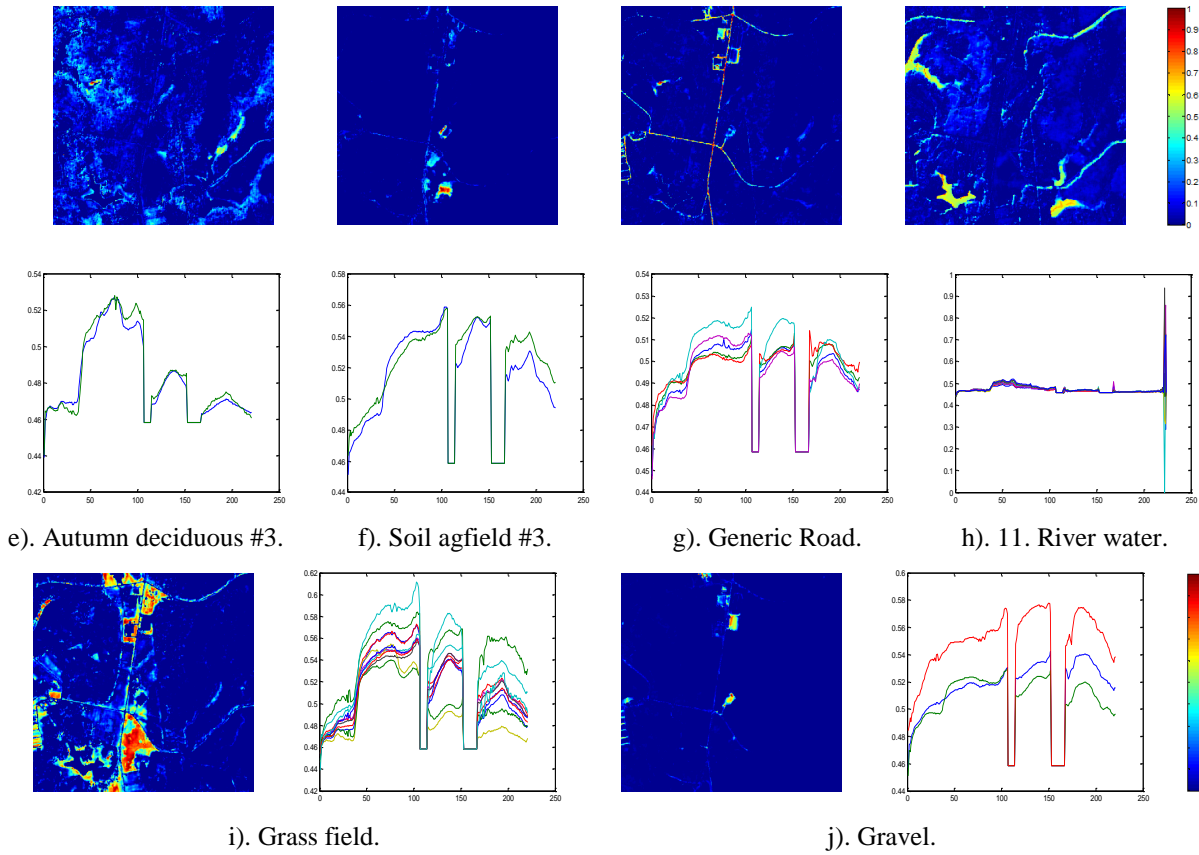
Figure 4-11. Endmember Classes resulting from the partitioning based on mean of all values in the image for the AVIRIS AP Hill data set.

a). Summer deciduous forest. b). Loblolly pine. c). Autumn deciduous #1. d). Autumn deciduous #2.

e). Autumn deciduous #3. f). Green agfield #1. g). Soil agfield #3. h). Generic Road.

i). River water. j). Grass field. k). Gravel.
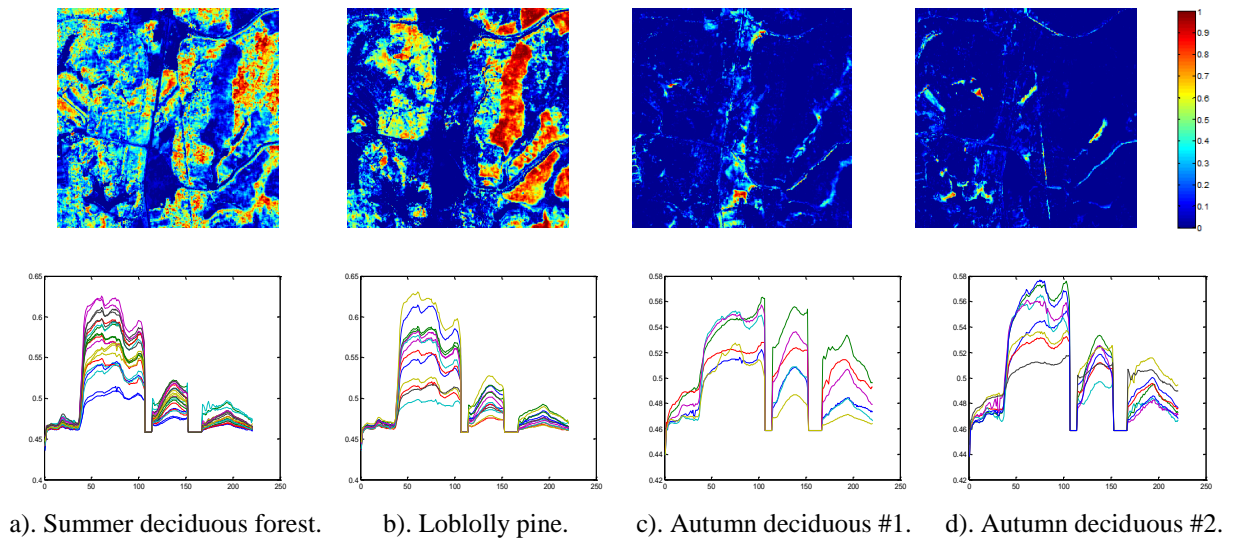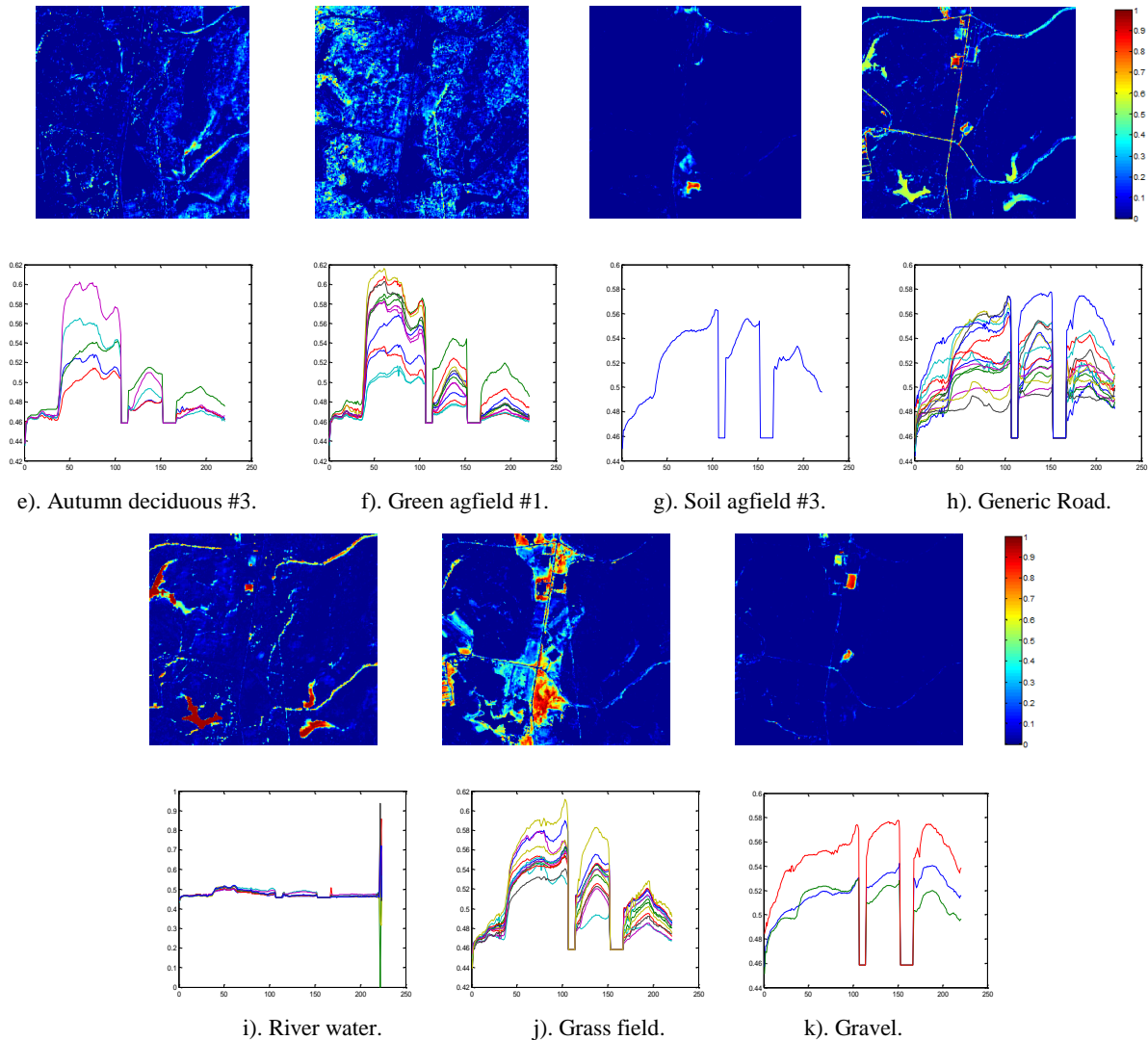
Figure 4-12. Endmember Classes resulting from the partitioning using the norm of the Shannon Entropy for the AVIRIS AP Hill data set.

The experimental results show that the Shannon entropy split the image in more tiles which enable extraction of more endmember classes than the other two metrics. The average number of endmembers obtained for the mean distance from spectral centroid, the mean distance of all values in the image and the norm of the Shannon Entropy are around 6, 5, and 4 respectively. The Shannon Entropy shows the fewest number of endmember per tile because it divides the image in more and smaller tiles, resulting in smaller number of classes per tile.
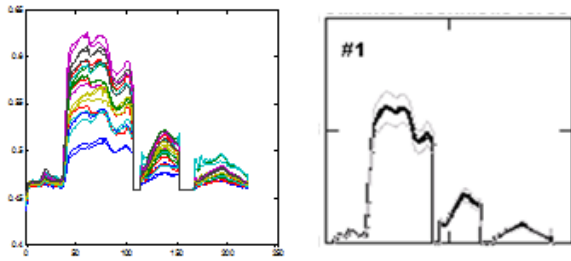
a). 1. Summer deciduous forest.
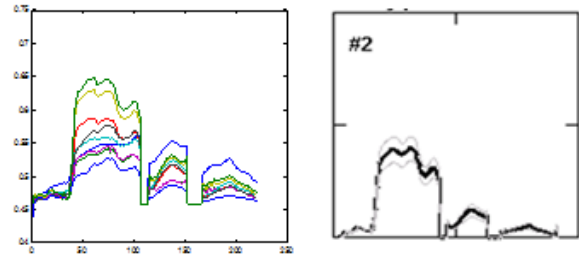
b). 2. Loblolly pine.
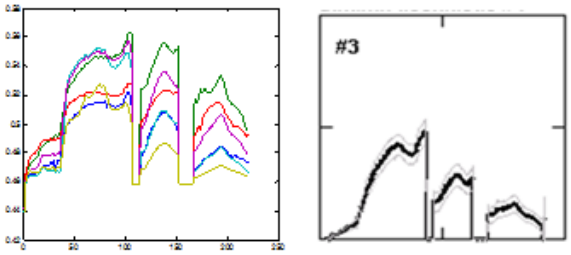
c). 3. Autumn deciduous #1.
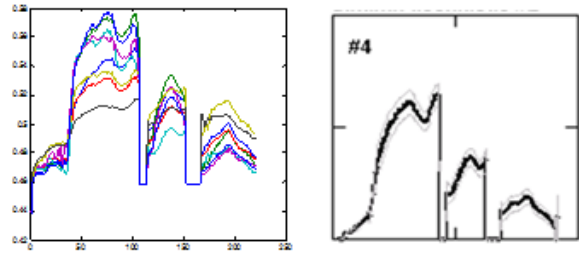
d). 4. Autumn deciduous #2.
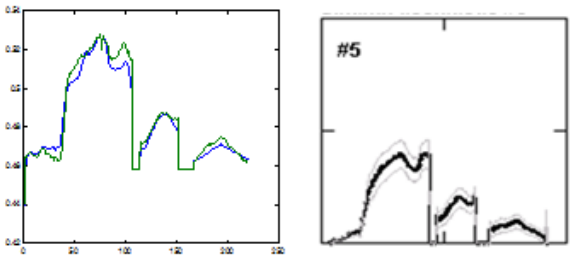
e). 5. Autumn deciduous #3.
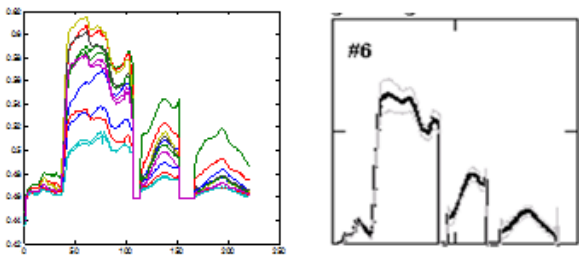
f). 6. Green agfield #1.
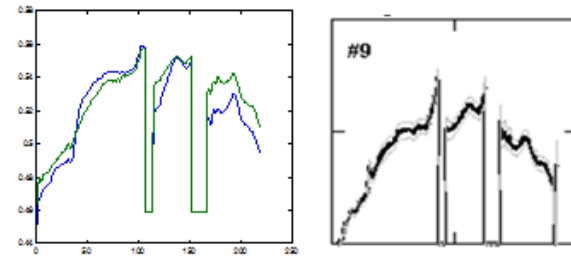
g). 9. Soil agfield #3.
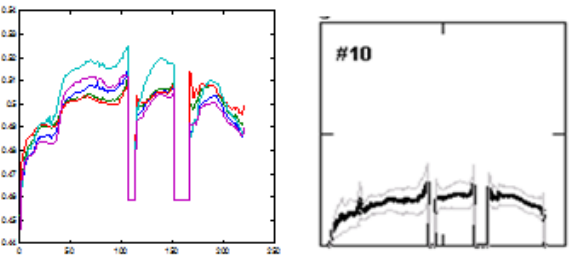
h). 10. Generic Road.
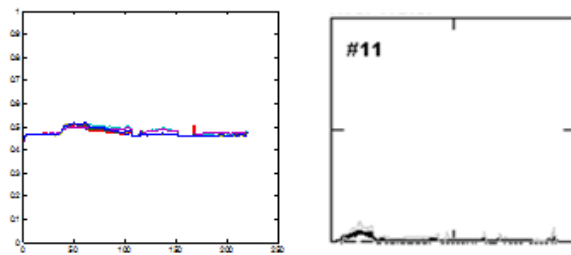
i). 11. River water.
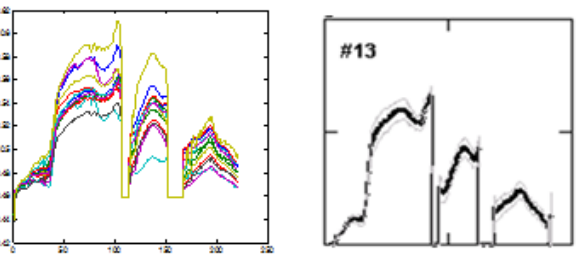
j). 13. Grass field.
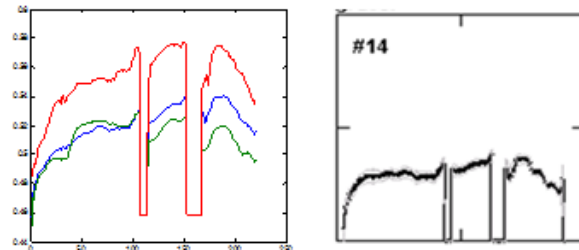
k). 14. Gravel.

Figure 4-13. Comparison between the spectral signatures of endmember classes resulting from the Clustering using norm of the norm of Shannon Entropy with publish ground true.

Figure 4-13 compares the endmember classes and spectral signatures obtained using the norm of

Shannon Entropy with the published spectral signatures for AP Hill [91].
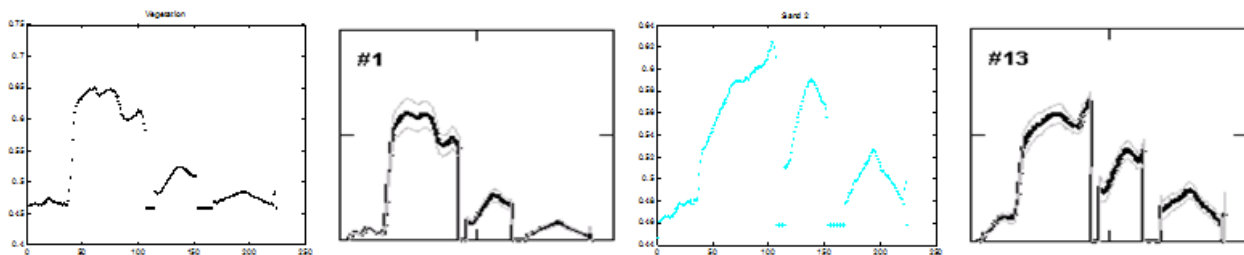
a). 1. Summer deciduous forest.

b). 13. Grass field.
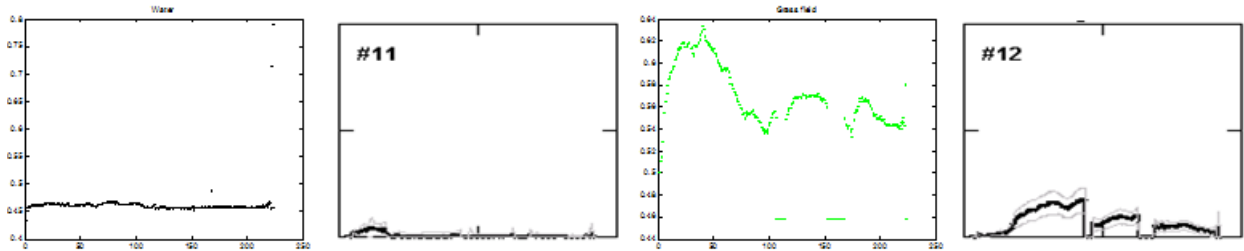
c). 11. River Water.

d). 12. Shaded Vegetation.
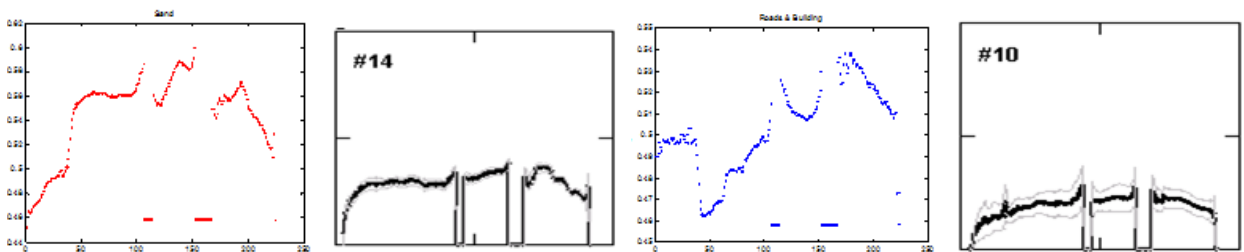
e). 14. Gravel.

f). 10. Generic Road.

Figure 4-14. Endmember resulting from the Global unmixing analysis using Nonnegative Matrix Factorization (NMF) with the ground true.

81

The results from the quadtree partitioning based unmixing agree more with published ground truth for the A.P. Hill [91] image than what was possible with the regular NMF. The endmembers obtained with the global approach fail to detect small details found in the image, which are detected with the local approach using various metrics.

4.3.2 Experiments with Indian Pines data.

Next we show analysis applied to the AVIRIS Indian Pines hyperspectral image. The results show 62 endmembers extracted with the mean from spectral centroid, 93 endmembers with the mean value, and 134 endmembers with the norm of Shannon entropy.

a). Background & Grass/ Woods.   b). Stone-steel towers   c). Hay-windrowed..   d). Background & Road.

e). Corn/Soybeans.

f). Corn-min/Soybeans-min.

g). Wheat.

h). Background &Wheat.

i). Background & Woods.
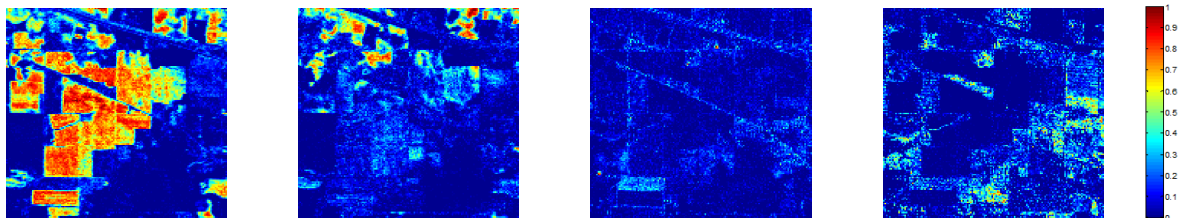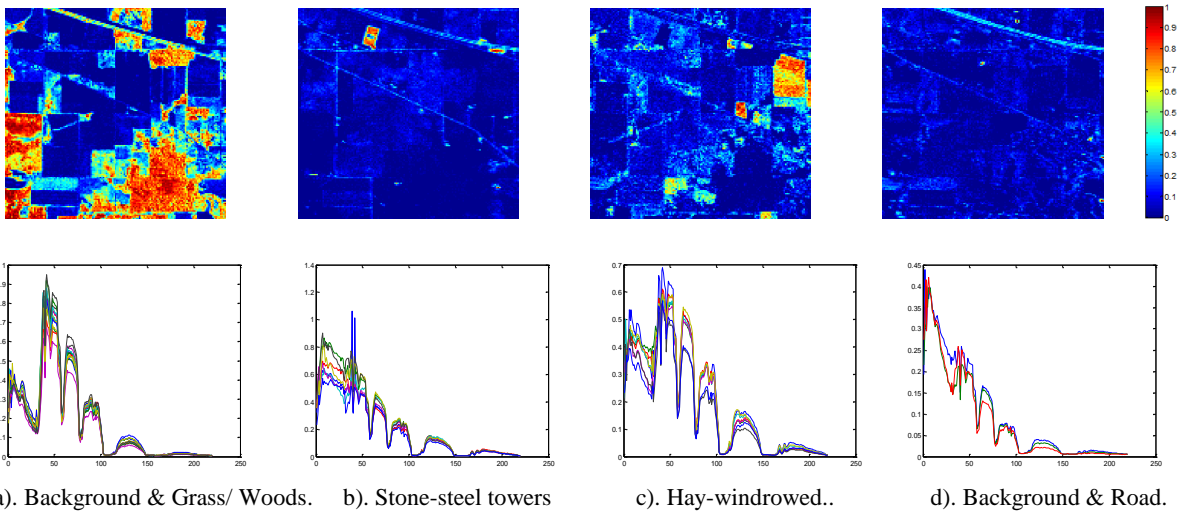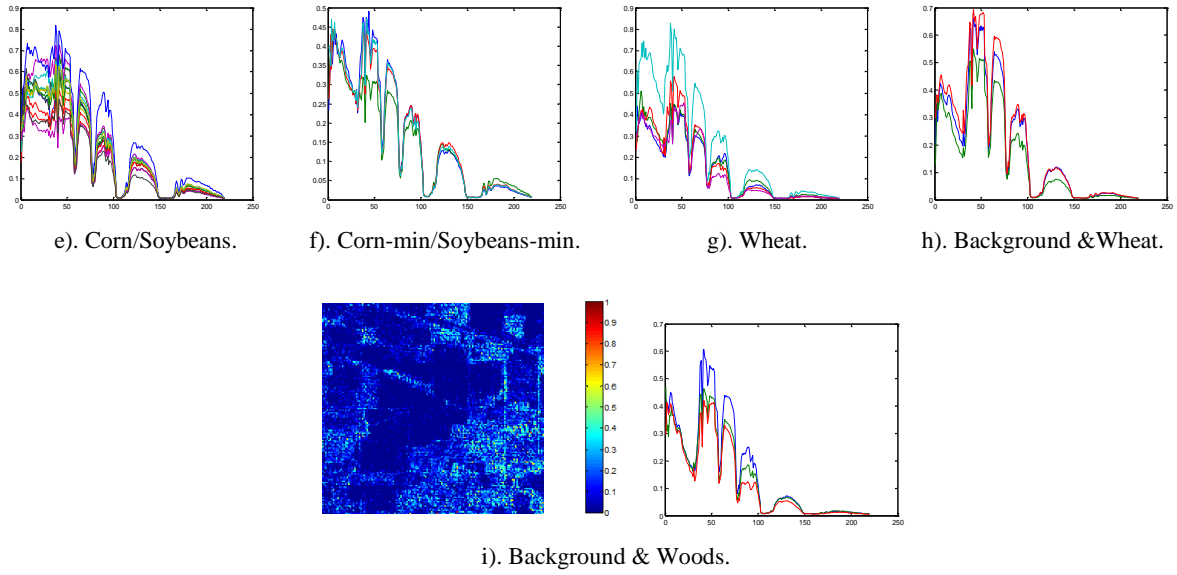
Figure 4-15. Endmember Classes resulting from the Clustering based on the partitioning using the mean distance from spectral centroid from the AVIRIS Indian Pines data set.

a). Background & Grass/ Woods.

b). Stone-steel towers

c). Hay-windrowed..

d). Background & Road.

e). Corn/Soybeans. f). Corn/Soybeans. g). Background & Grass Tree h). Background &Woods.

i). Background &Wheat. j). Wheat. & Road
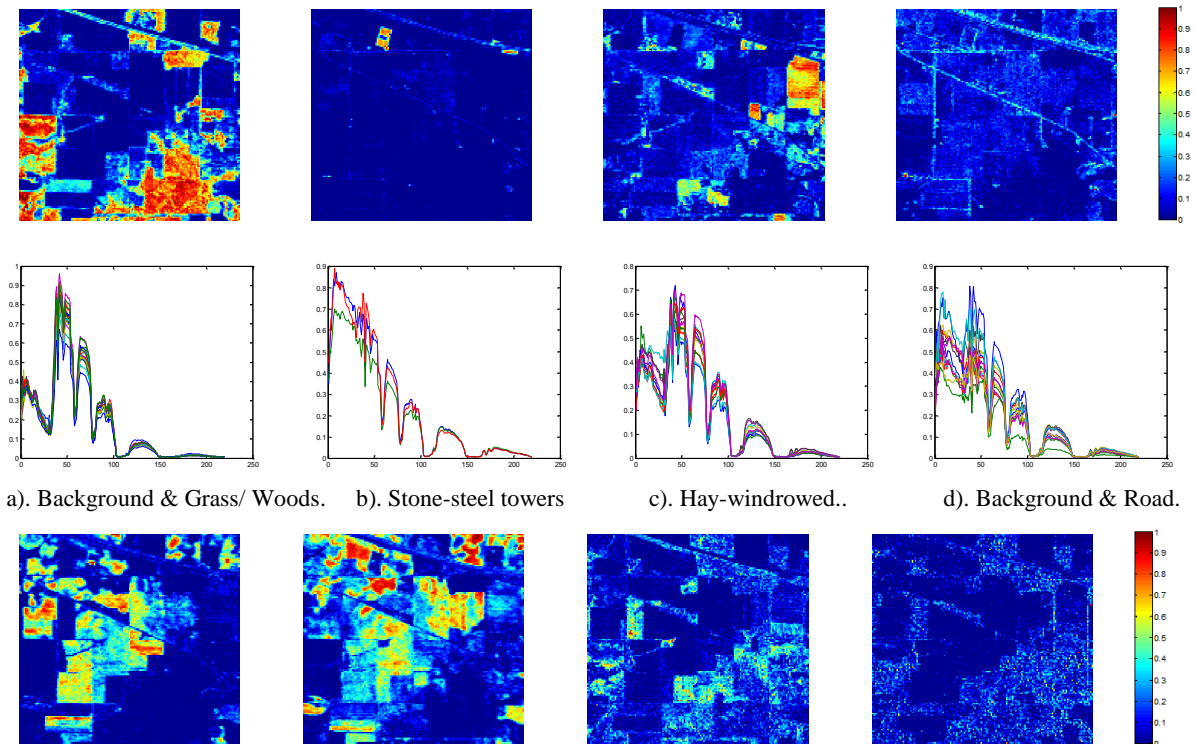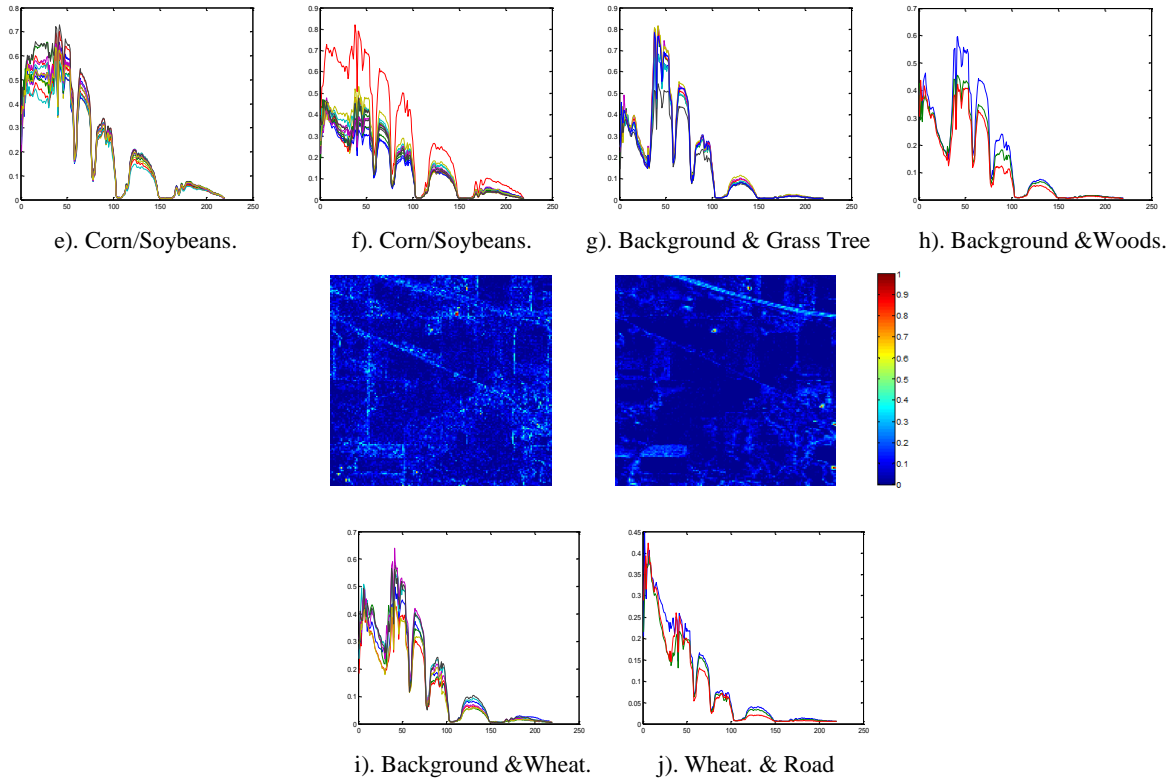
Figure 4-16. Endmember Classes resulting from the clustering for the partitioning based on mean of all values in the image from the AVIRIS Indian Pines data set.

a). Background & Grass/Trees. b). Background & Woods. c). Grass/Pasture & moved. d). Stone-steel towers.

84

e). Corn-notill. f). Alfalfa. g). Corn-min/Soybeans-min. h). Wheat.

i). Hay-windrowed. j). Soybeans-notill & min. k). 11. Soybeans-notill & clean. l). Others Background.
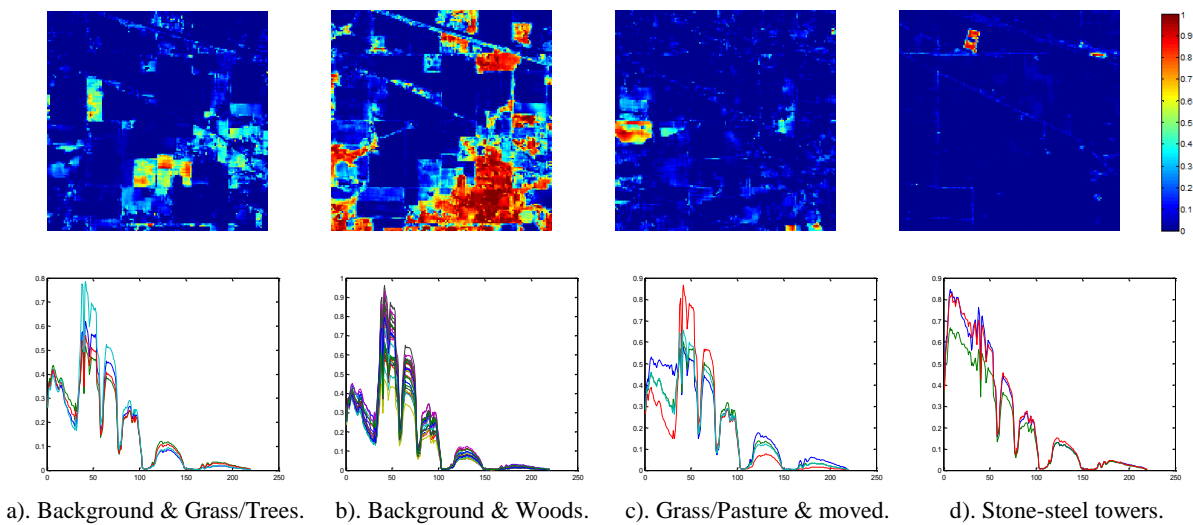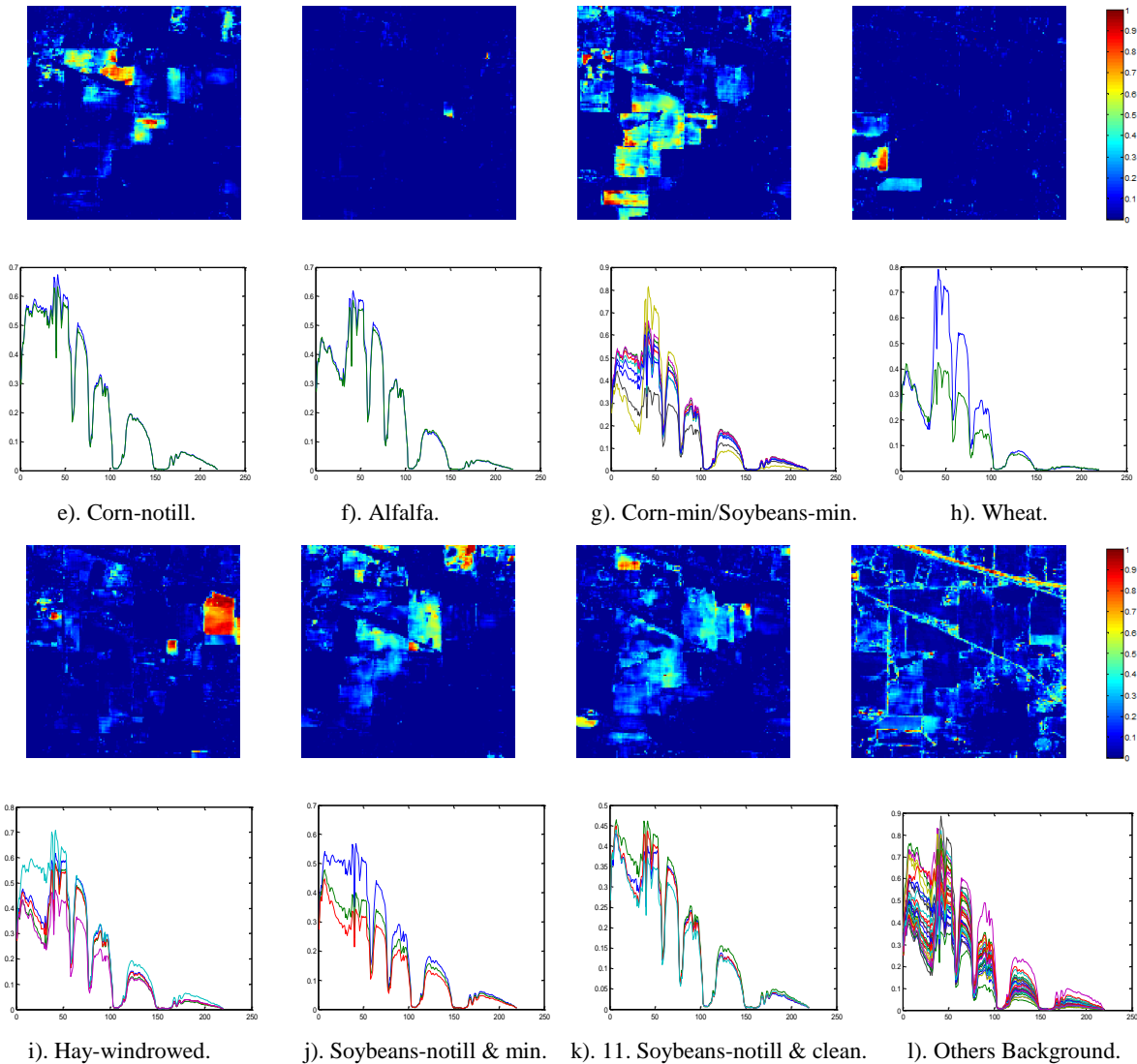
Figure 4-17. Endmember Classes resulting from the Clustering using norm of the Shannon Entropy from the AVIRIS Indian Pines data set.

Once more, the mean distance from spectral centroid is the metric that resulted in the fewest number of endmembers classes, while Shannon entropy resulted in the finest image partitions. The global analysis is shown in section 4.5 where were obtained 8 endmembers applying the NMF to the full image, mixing classes that appear separate in the local analysis.

The number of classes shown in the classification map for Indian Pines are 16. The number of endmember found for each tile varies between 3 and 10. The number of endmember was estimated using the fitting error curve. The number of spectral endmembers for each of these three

metrics were 62, 93 and 134 respectively. However, when the spectral endmembers were clustered, 9, 10 and 12 endmember classes were identified using the hierarchical clustering method. The number of the endmember classes found with the Shannon entropy was closer to the number of classes from the classification map in Indian Pines Ground truth (16 classes).

4.3.3 Comparing the sensitivity of different spectral metrics by varying the Partition Criterion.

As the partitioning criterion is changed, the obtained partitioning in the image can vary the number of endmember classes for the global image. Here too many tiles defeats the purpose of the quadtree partitioning and make more complex the endmember extraction process. However too large tiles may result in non convex regions as described in Chapter 3. Here we explore the effects of changing the stopping criterion in the partitioning. Different partitions were obtained with 100, 95, 90, 85, 80, and 75 percent of the global variability.
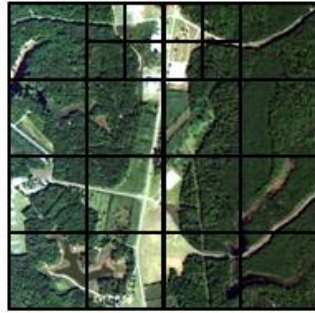
a) 100%   b) 95%   c) 90%

d) 85%   e) 80%   f) 75%

Figure 4-18. Resulting Partitions using the mean distance from spectral centroid for different percentages of global variability.
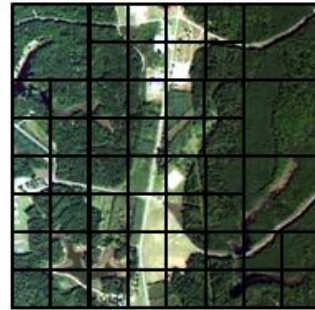
a) 100%   b) 95%   c) 90%

d) 85%   e) 80%   f) 75%

Figure 4-19. Resulting Partitions using the mean of all values in the image for different percentages of global variability.

a) 100%   b) 95%   c) 90%

<div align="center">

d) 85%   e) 80%
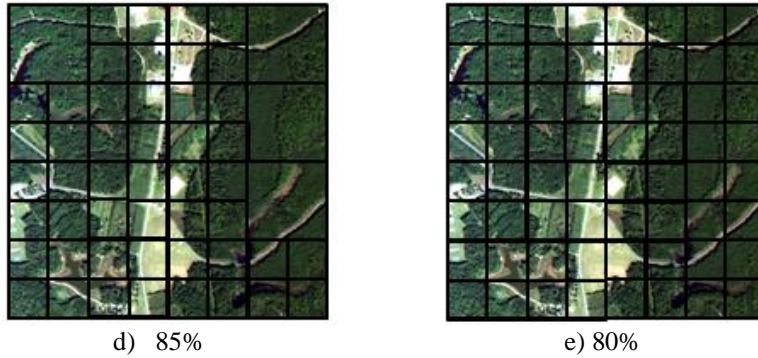
Figure 4-20. Resulting Partitions using the norm of Shannon Entropy for different percentages of global variability.

</div>

A criterion is sensitive to spectral variability if small changes in the criterion produces significant changes in the partition with small tiles for 90% level. It also reached the highest level of partitioning of 1/64 with 80%, while the other metrics never did.

<div align="center">

Table 4-1. Summary of the Values of different metrics for change the level of the quadtree.

</div>

INDEX	PARTITION	
	1/4 - 1/16	1/16 - 1/64
M1	96.78	82.31
M2	98.23	93.46
M3	–	96.68

Table 4-1 shows the criterion level for transitioning between partitioning levels. Again Shannon entropy reached finer partitioning with just 4% change from global. Experiment show that Shannon entropy is the most sensitive spectral variability metric.

4.4 Comparing Quadtree Region Partition Metrics with 64 parts divisions.

Cleary the finer the partitioning the more endmember classes we can identify. However finer partitioning results in more computational calculate. Here we compare endmember extraction results of our approaches with what possible with the finest partition.

4.4.1 Fort A.P. Hill Image Results.

Here show the results obtained when the APHill image is partitioned in 64 tiles and the corresponding unmixing results.
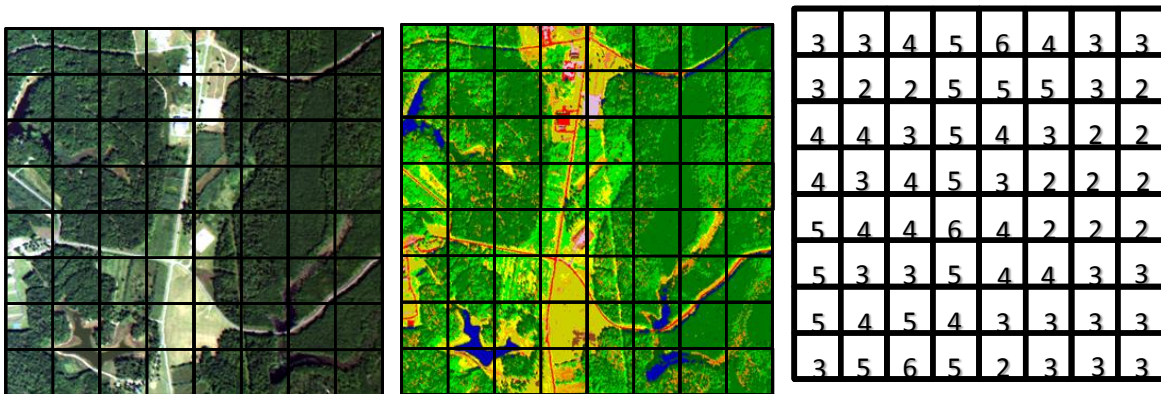
Figure 4-21 Number of endmembers per tiles for the 64 tiles partitioning for APHill image.

| a) Summer deciduous forest | b) Loblolly pine | c) Autumn deciduous #1 |

89
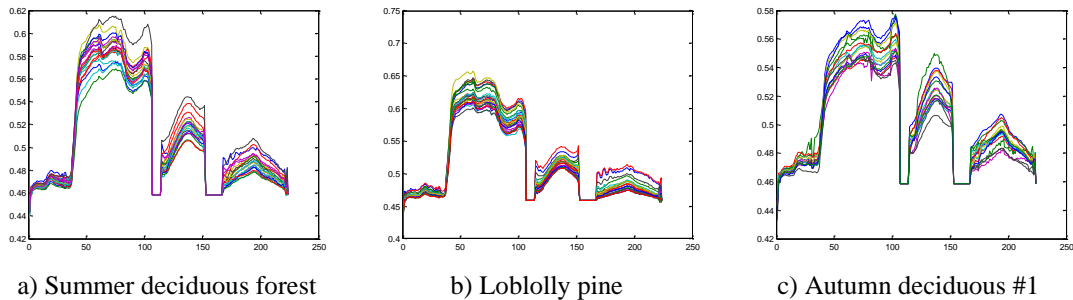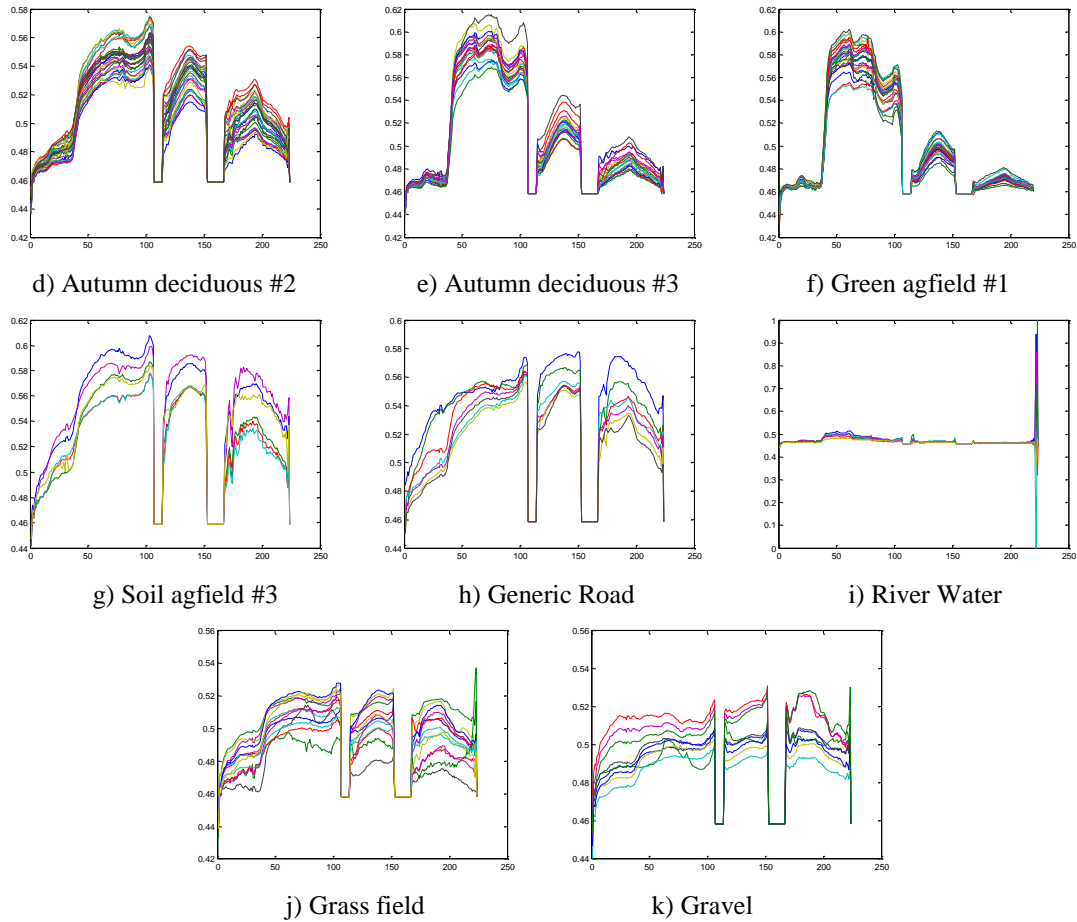
Figure 4-22 Endmember classes extracted from the 64 tiles for APHill image.

A comparison between the endmember classes extraction results obtained with the Shannon entropy partitioning for AP Hill, and the endmember classes obtained with partitioning of the image into 64 tiles, we find the same amount of endmember classes. Although the amount of the spectral endmembers is greater they capture the same endmember classes. That show that Shannon entropy obtain the endmember classes with a coarser partitioning of the image. The average of classes per tile is the 3.6 for 64 divisions compares with 4.3 for Shannon entropy.

4.4.2 Indian Pines Image Results.

Here we present similar analysis for Indian Pines.
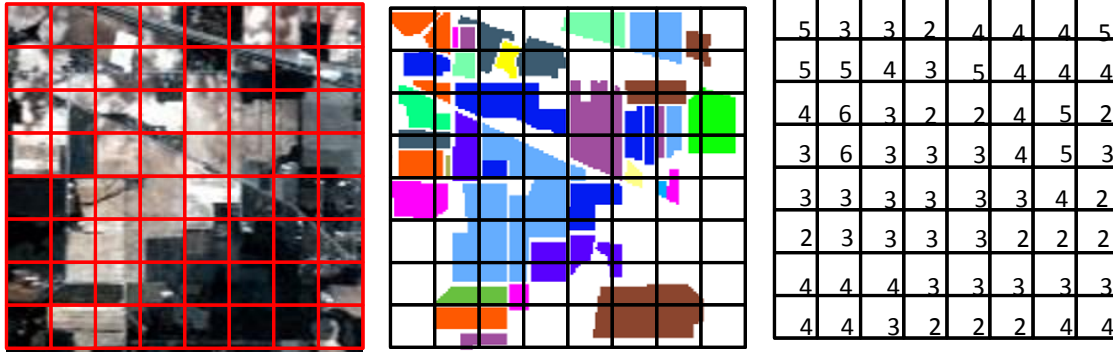
Figure 4-23 Number of Endmember extracted per tile using 64 tiles for Indian Pines.

a). 1. Background & Grass/Trees.

b). 2. Background & Woods.

c). 3. Grass/Pasture & Grass/Pasture moved.

d). 4. Stone-stell towers.

e). 5. Corn-notill.

f). 6. Alfalfa.

g). 7. Corn-min/Soybeans-min.

h). 8. Wheat.

i). 9. Hay-windrowed.

j). 10. Soybeans-notill & min.

k). 11. Soybeans-notill & clean.

l). 12. Roads Background.

m). 13. Other Background.   n).11. Nothing.
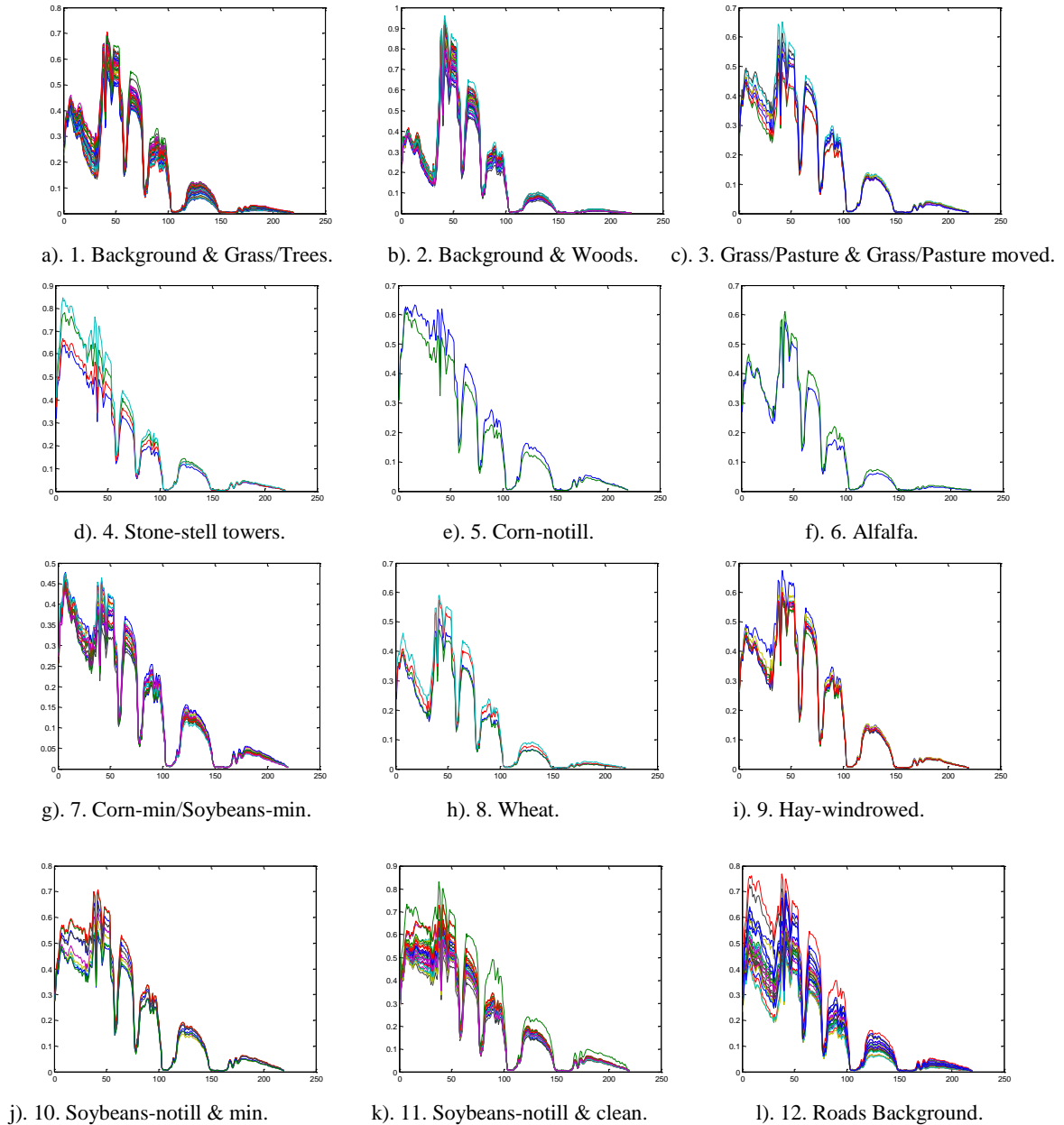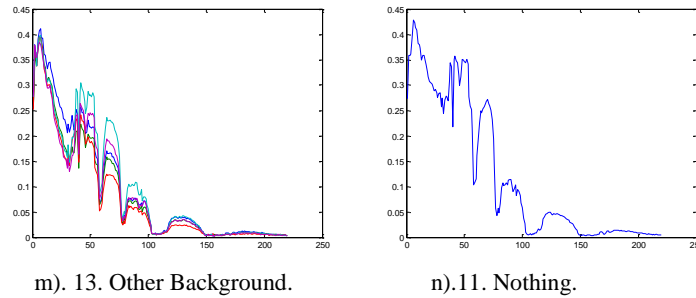
Figure 4-24 Endmember classes extracted for the 64th tiles partitioning for Indian Pines.

Again comparing the results endmember classes obtained with Shannon entropy, and the endmember classes obtained with the 64 tiles, we find two more classes with the 64 tiles than the endmember classes found with Shannon entropy. The two extra endmember classes found, are included into the others background by the Shannon entropy. However, the main endmember classes are separated by the Shannon entropy well. It has problem with background that being to be compose of several spectral classes.

4.5   Comparing Results of Endmember Extraction using sacNMF and Quadtree with full cNMF.

Next show the results obtained by applying cNMF for unmixing of the full AP Hill and Indian Pines hyperspectral images. The number of endmember was determined using the fitting error curve, obtaining 6 and 8 endmembers for APHill and Indian Pines image, respectively.

a).1. Summer deciduous forest.

b). 13. Grass field.

c). 11. River water & loblolly pine

d).3. autumn deciduous t.

e). 9. soil ag field.

f). 10. generic road & gravel.
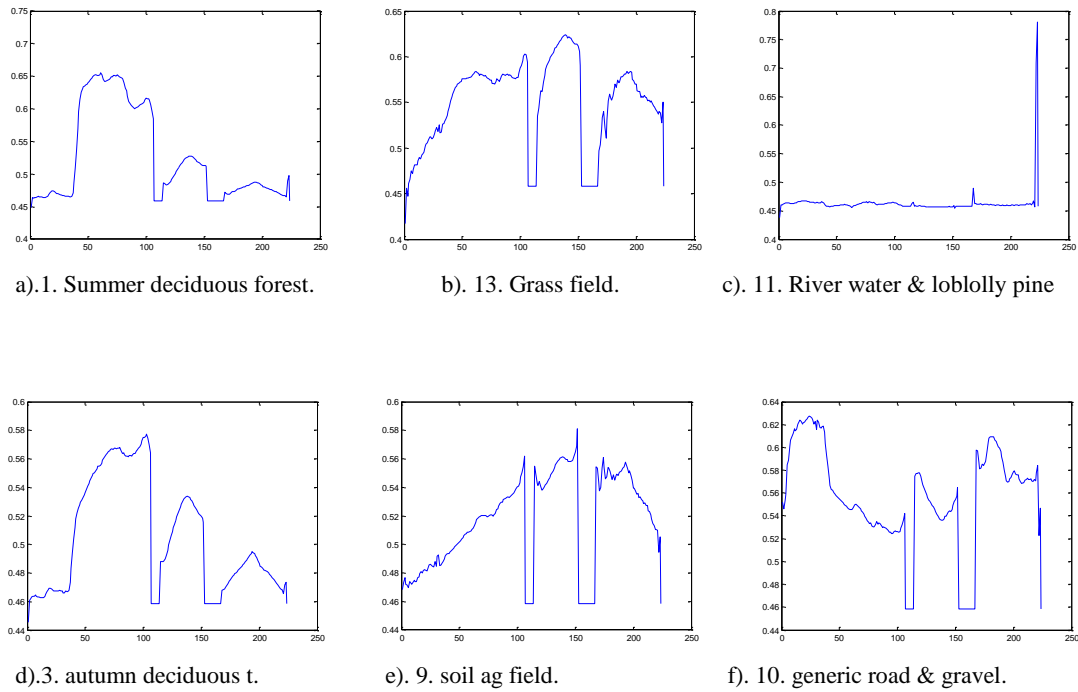
Figure 4-25. Endmember extracted using global unmixing analysis using cNMF with the ground true for APHill image.

The extracted spectral signatures and abundance maps are shown in Figures 4-25 and 4-26 for AP Hill and Figures 4-28 and 4-29 for Indian Pines.

a).1. Summer deciduous forest.

b). 13. Grass field.

c). 11. River water & loblolly pine

d).3. autumn deciduous t.

e). 9. soil ag field.

f). 10. generic road & gravel.
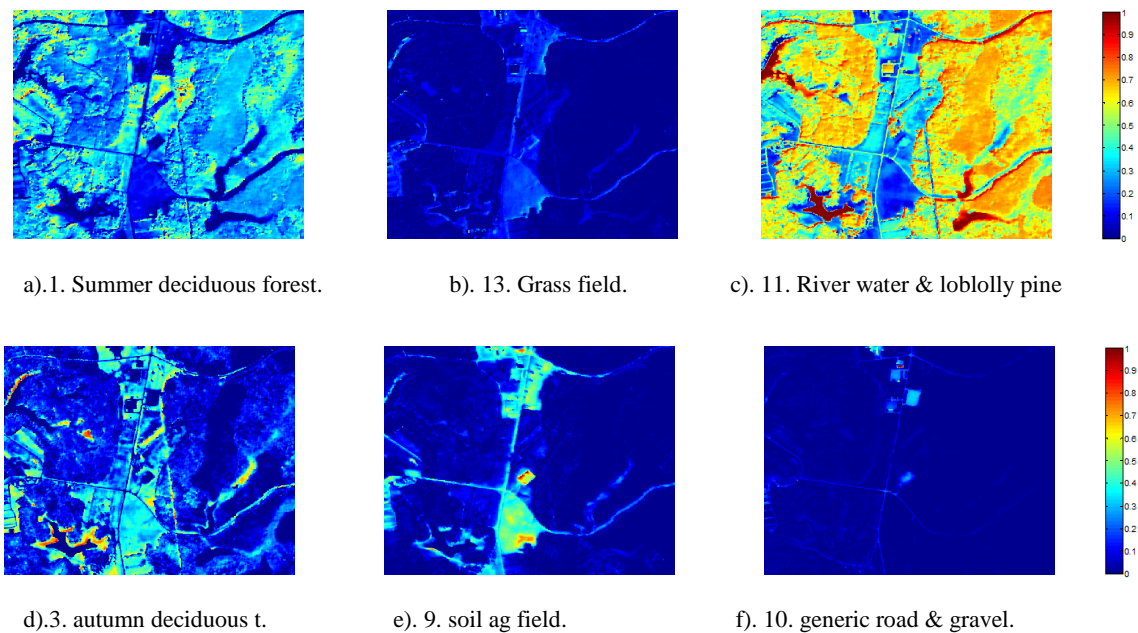
Figure 4-26. Abundances resulting from global unmixing s using NMF for APHill image.

The unmixing results using the quadtree partitions agree more with published ground truth for the A.P. Hill image than what was possible with the regular cNMF. The endmembers obtained by the cNMF fail to detect small details (see Figure 4-27) found in the image, that are detected with the local approach using various metrics. The river water is mixed with vegetation, the generic road with the gravel and the soil ag field (Figure 4-27).
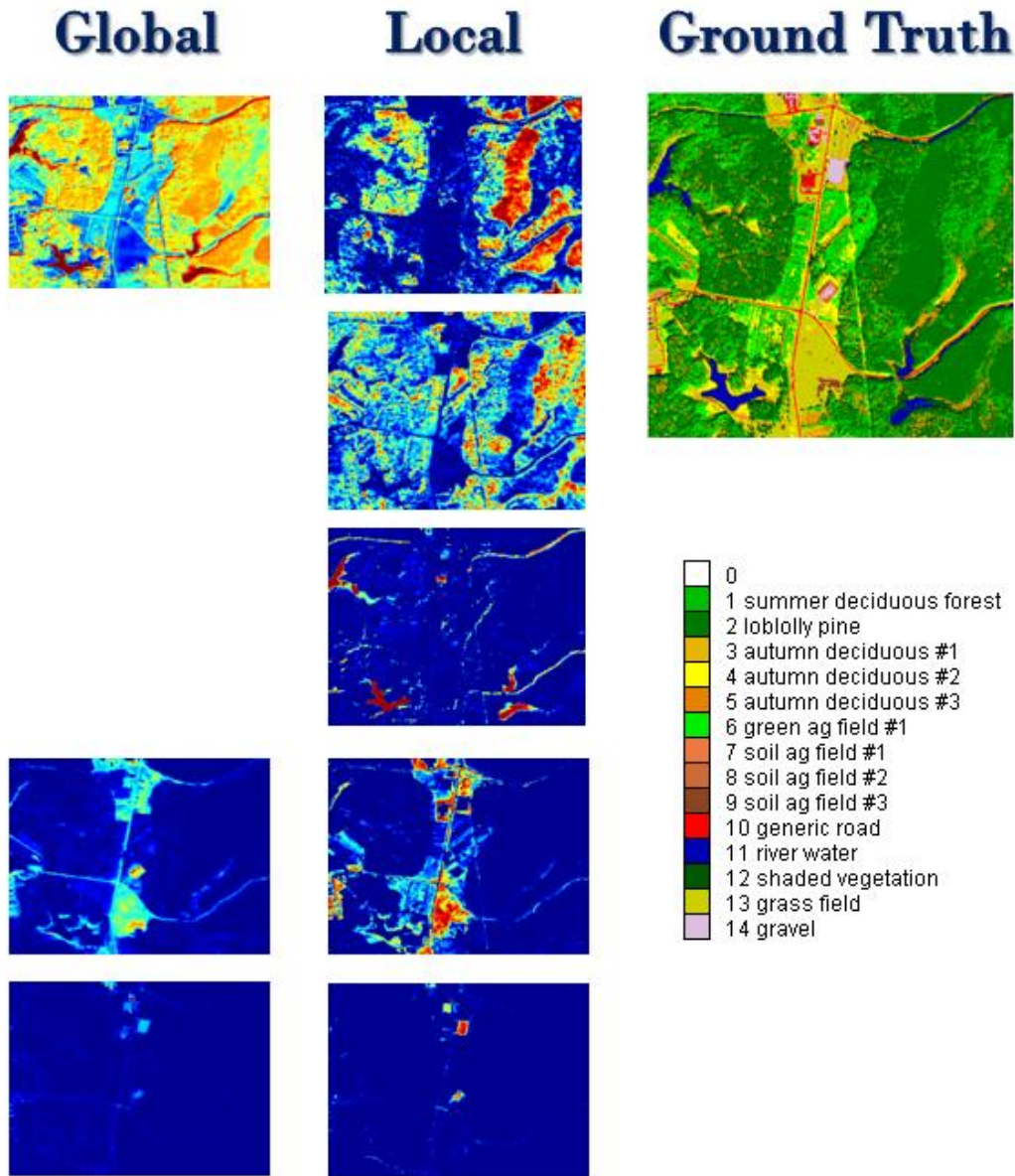
Figure 4-27. Abundances of Endmember classes resulting from the Local unmixing analysis using Nonnegative Matrix Factorization (NMF) and clustering with the ground true for APHill image.

94

Table 4-2 Comparison between cNMF and sacNMF methods using APHill image.

APHill Image Class	cNMF	sacNMF
1	vegetation (1,2,3,4,5,6,12)	summer deciduous
2		loblolly pine
3, 4, 5		autumn deciduous
6		green ag field
12		shaded vegetation
10	10,11	generic road
11	11	river water
14	10, 11	gravel
7, 8, 9	7,8,9,13	soil ag field
13		grass field

In Figure 4-27 comparing the global results with their local results. We show how the Local process highlight some existent classes in the global result, and can separate classes that appear mixed in the global results. In table 4-2 is shown a summary of the results between cNMF and sacNMF methods.

a). Soybeans & Corn.

b). Hay-windrowed & Grass/Trees.

c). Background & Woods & Grass/Pasture

d).Grass / Tree

e). Background.

f). Wheat & Grass Pasture.

g). Stone-steel towers & roads   h). Other Background.
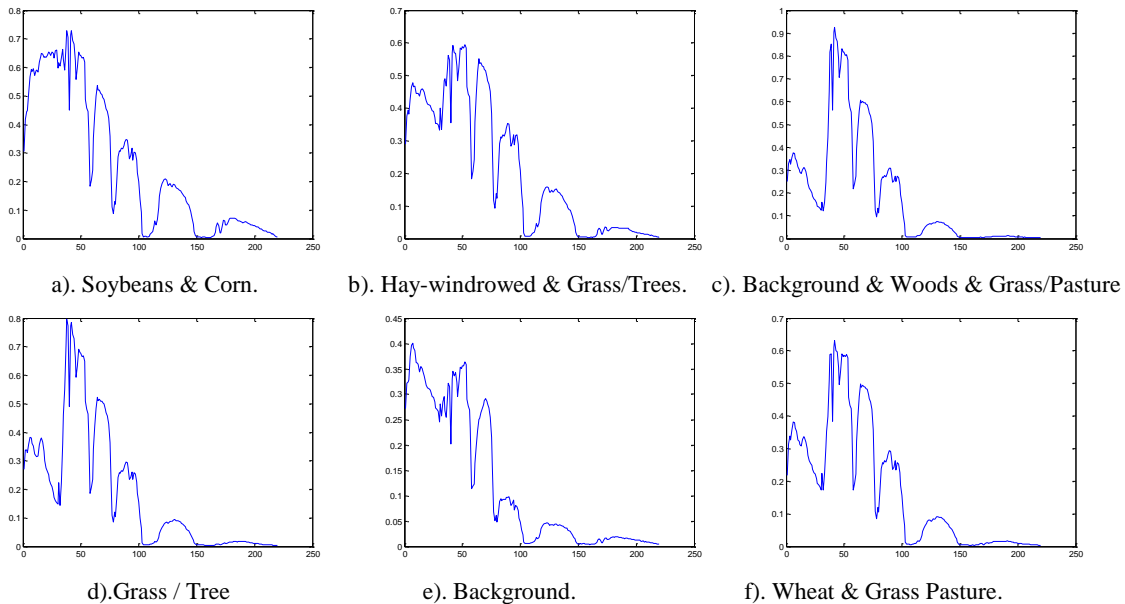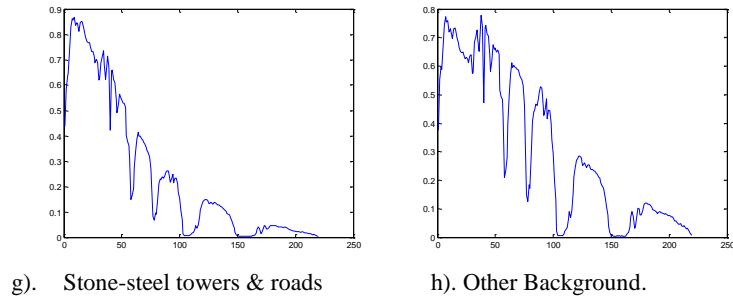
Figure 4-28. Endmember extracted using cNMF for Indian Pines image.

a). Soybeans & Corn.   b). Hay-windrowed & Grass/Trees.   c). Background & Woods & Grass/Pasture

d). Grass / Tree.   e). Background.   f). Wheat & Grass Pasture.

g). Stone-steel towers & roads   h). Other Background.
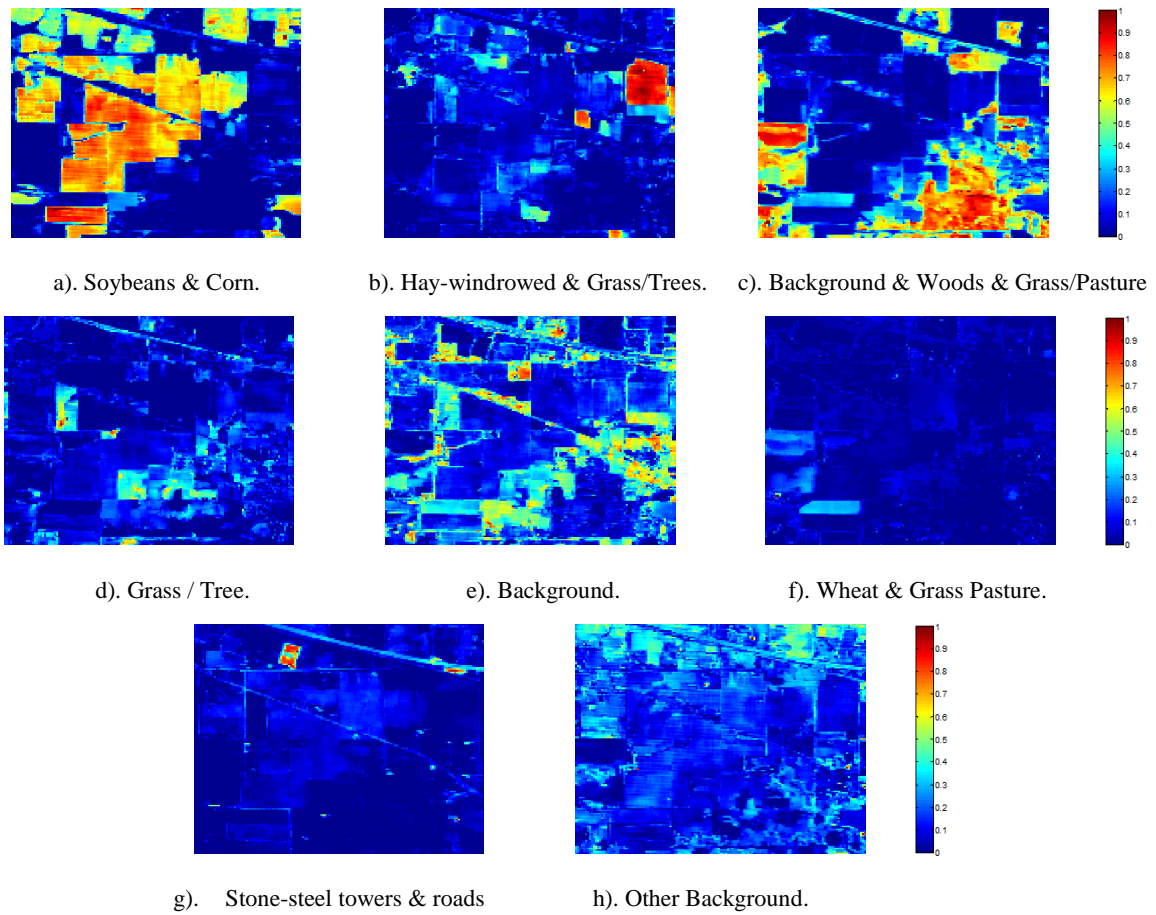
Figure 4-29. Endmember Abundances using cNMF for Indian Pines image.
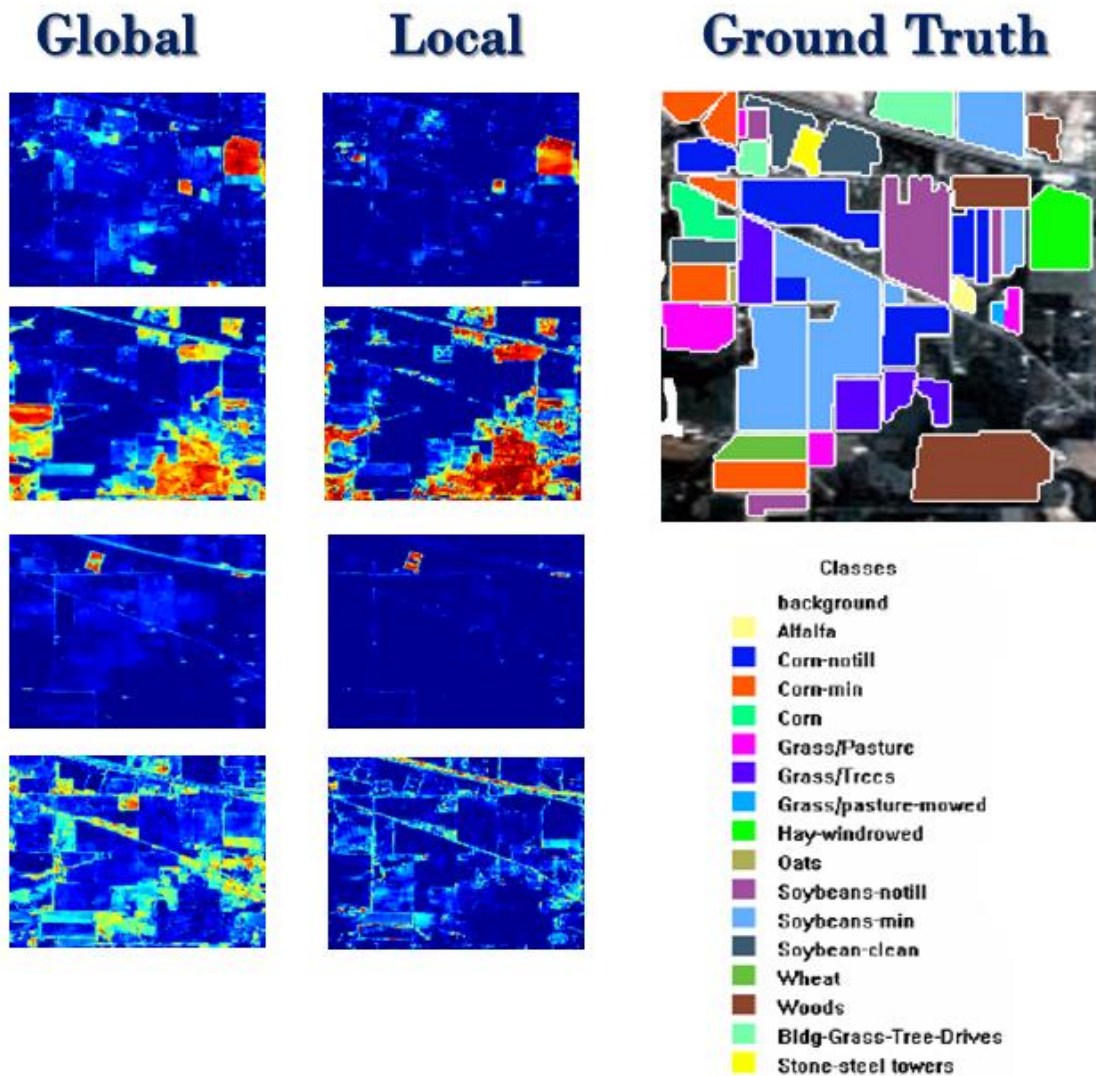
Figure 4-30. Abundances of Endmember classes resulting from the Local unmixing analysis using Nonnegative Matrix Factorization (NMF) and clustering with the ground true for Cuprite image.

The obtained results from the proposed approach with published ground truth for the Indian Pines image are more agree than the results with the regular cNMF. Again, the endmembers obtained with the cNMF cannot detect details found in the image and mix then (see Figure 4-31). While these detail are detected with the local approach. The Soybeans & Corn are mixed, the woods with background and grass pasture, the hay-windrowed with the grass and trees (see Figure 4-30 and 4-31).
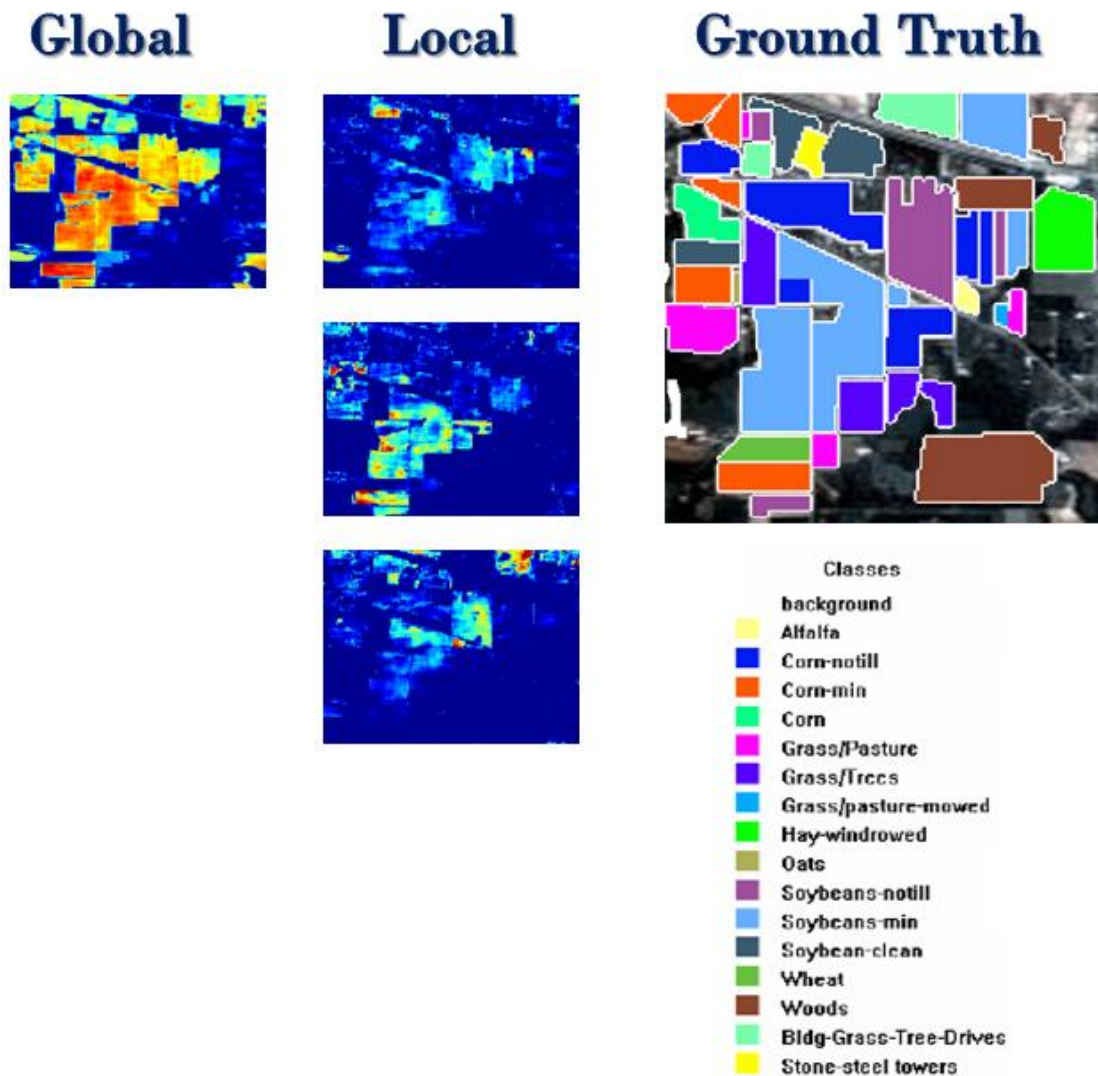
Figure 4-31. Abundances of Endmember classes resulting from the Local unmixing analysis using Nonnegative Matrix Factorization (NMF) and clustering with the ground true for Cuprite image.

Initially we show three specific classes for APHill image and then show five specific classes in Indian Pines image. In the APHill Image we select the vegetation that in global process, mixing the water class with the vegetation class, while in local process can separate, the summer deciduous forest, loblolly pine and the river water classes. And also detect same classes in the image but with higher abundance level, like a grass field and gravel.

98

In Figures 4-26 and 4-29, can be observed that in the local analysis more independent materials can be detected in the unmixing process. The global process mixing the classes Soybean notill, mean and clean with corn notill, min and clean, while in the local process can separate the group names, like Soybean and Corn. Also the local process can filter as the best manner other material detected for the global process (see Figures 4-30 and 4-31).

4.6 Summary.

In this chapter, we showed how quadtree partitioning can be combined with cNMF for endmember extraction. First, we studied quadtree region partitioning based on three region partitioning criteria to measure spectral uniformity (the mean distance from spectral centroid, the mean value, and the norm of Shannon entropy). The most sensitive results were obtained using the norm of Shannon entropy.

Endmember classes obtained from clustering spectral endmembers extracted from the partitioning obtained with the norm of the Shannon entropy are the closest to the available ground truth of the images. These results are compared with the standard cNMF, showing that the local analysis extracts more materials than global analysis.

We further compare unmixing results with unmixing based on a fine image partitioning and the Shannon entropy provided the closest results.

We conclude then that spatial subsetting improve our capability to extract endmember classes. Shannon entropy results in the best partitioning where tiles have the fewest endmembers and capture more of the image classes. The proposed approach for unmixing builds from these two important results.

5. THE SPATIALLY ADAPTIVE cNMF.

Figure 4-1 depicts the different components of the proposed spatially adaptive cNMF (sacNMF) algorithm for hyperspectral image unmixing.
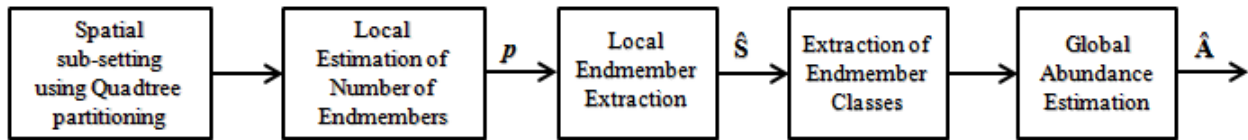
Figure 5-1. Proposed unmixing Approach

5.1 Overview

This algorithm is an unsupervised hyperspectral unmixing process (see Figure 5-1) that is based on the constrained non negative matrix factorization (cNMF), and taken advantage of the spatial information at the image. The proposed algorithm looks at local information to extract local spectral endmember information and merge then into endmember classes to develop an accurate description of the scene under study.

5.2 Spatial Subsetting using Quadtree Partitioning.

The image is divided into spectrally uniform regions or quadrants resulting from the quadtree partitioning (see Section 4.1). The endmember extraction is performed on each individual tile and is based on the empirical results shown in Chapter 3 that uniform regions follow better the linear mixing model.

Furthermore, spatial subsetting makes, the approach more sensitive to endmembers present in small areas when compared to a global approach that assesses the full image at once. To determine the appropriate number and size of the spatial subsets for a given image, we use two splitting

criteria. First, is the maximum level of the quadtree partition (64 parts). Second, reduction below

90 percent of the value of the spectral variability metric for the full image (see Section 4-2) [86].

Based on results reported in Chapter 4, we decided to use the Shannon entropy as spectral

variability metric.

The following procedure is used to calculate the Shannon entropy. Initially the hyperspectral

image is loaded and converted of 3D to 2D dimensions matrix (pixel per bands), using reshape. In

the next step, clustering is accomplished through the rows of the 2D matrix (pixels in the 3D

image), grouping the similar areas. Then counting the pixels in each group, calculate the value of

the Shannon entropy of the image. Below is showed the pseudo code for the Shannon entropy

algorithm:

```
Load image
[m n o] = size (image);
2dimage = reshape (image, m*n, o);
T= clusterdata(2dimage,'maxclust',Index,'linkage','ward','distance','cosine');
for i=1: Index
    Counts (i) = find (T==i)
    Total = sum (Counts);
    q = Counts. /Total;
    Entropy = -sum (q.*log (q));
end
```

5.3   Local Estimation of Number of Endmembers.

After quadtree partitioning, the next step is to extract the endmembers from each tile. Most

endmember extraction methods assume the number of endmembers as known, for this reason the

estimation of the number of endmember also has to be considered as part of the unmixing problem

solution. Approaches commonly followed in hyperspectral unmixing to determine the number of

endmembers were described in Chapter 2.

The extraction of endmember is performed on each tile using the constrained non-negative

matrix factorization algorithm (cNMF) [22]. That algorithm does not assume that there are pure

pixels in the image. Given the number of endmember p, the cNMF determines the endmember matrix $\hat{S}$ and abundance matrix $\hat{A}$ by solving the approximation problem:

$$\hat{S}, \hat{A} = argmin_{S_{ij}>0, A_{ij}>0, \sum_{i=1}^{p} a_i = 1} \|X - SA\|_F^2 \tag{5.1}$$

5.3.1 Fitting Error Curve.

The estimation of the number of endmembers in each tile is performed by using the fitting error curve, as a function of p which is given by:

$$E_p = \frac{\|X - SA\|_F^2}{\|X\|_F^2} \tag{5.2}$$

The number of endmembers is selected as the value of p immediately after the knee on the fitting error curve [92]. The estimated number of endmembers for each partition will be different. For example in Figure 5-2 we can see two fitting error curves where in Figure 5-2 (a) the number of endmembers is $p = 6$ and in Figure 5-2 (b) the number of endmembers is $p = 5$. In the algorithm (see pseudo code bellow), the value of p is selected when the error value is less than the threshold error around 0.000005.

```
Load image
[m n o] = size (image);
2dimage = reshape (image, m*n, o);
for i=2:20
    End2 (i) = svdss (2dimage, i);
    Endmembers (i) = 2dimage (:,End2(i));
    [Abd new(i), End new(i)]= cNMF (2dimage, Endmembers (i), iter);
    Imgnew (i) = End new (i)* Abd new (i);
    Error(i)=((norm(2dimage-Imgnew(i),'fro'))^2)/((norm(2dimage, 'fro'))^2);
    if Error(i) <= 0.000005
        p = index (Error (i));
    end
end
```
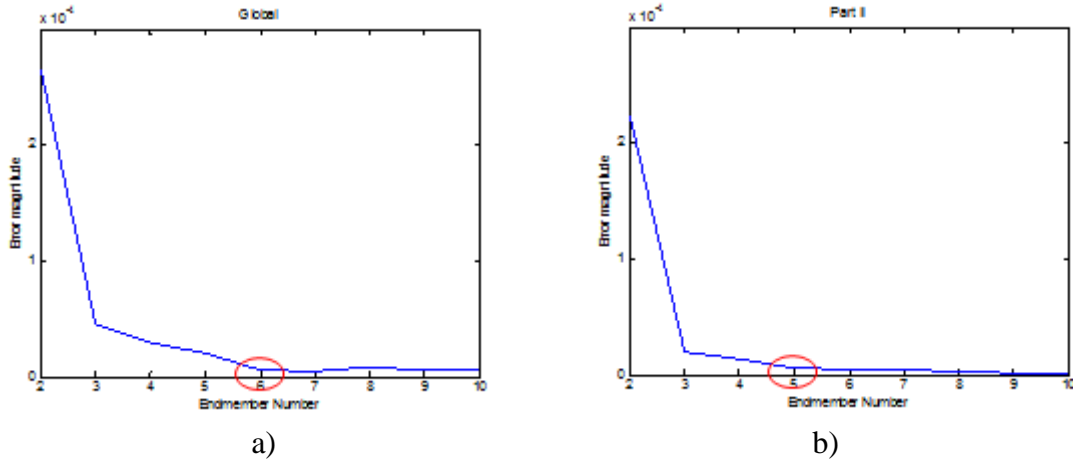
Figure 5-2. Examples of fitting error curves for the full image and specific tile 2. a) *p = 6*, **b)** *p = 5.*

5.4   Endmember Classes Extraction.

In multi and hyperspectral image classification, information classes are associated with categories of interest to the user, while the spectral classes refer to pixels with similar spectral signatures [34]. A spectral class may be composed of several spectral signatures [38]. Spectral variability in spectral classes may result from differences in moisture content, soil type, underlying vegetation, topographic influences, among others. The variability of spectral classes can be modeled using clusters or probability distributions. Information classes can be composed of several spectral classes. It is not unusual to find several spectral classes for the same soil information class, for the same apparent type of vegetation, and so on for other cover types in a scene.

Endmember classes are defined in a fashion similar to spectral classes. Endmember classes are built by clustering spectral endmember signatures.

To build the spectral endmember classes, clustering techniques are used to group spectral endmembers signatures into sets with similar spectral features to represent the same material.

103

Clustering techniques are widely used in different areas such as patter recognition, machine learning, data mining, statistical analysis and many other applications. Specifically, in hyperspectral image processing applications, clustering techniques are used in classification, detection, segmentation, and unmixing [102]. In sacNMF we use *hierarchical clustering*,(see Sec 2-7) based on results presented in [43].

Hierarchical clustering (see Chapter 2 for more details) finds a family of grouped partitions of the data based on specific threshold condition. The principal advantage of these kinds of algorithms is that they not need specific number of clusters, because the data can be broken by levels obtaining different partitions of the data [104].

In our implementation, we use MATLAB implementation of hierarchical clustering algorithms available in its Statistic Toolbox. The computational complexity of hierarchical clustering is $O(n^2)$ for the three linkage criterions (*single, complete* and *average*) [103], where *N* is the number of samples. These algorithms are very inefficient for large datasets. But, for the current application, it is expected that the computational cost of hierarchical algorithms not to be significant since the number of spectral endmembers is a relatively small dataset of few hundred signatures.

5.4.1 Estimation of the number of Endmember Classes.

The estimation of the number of spectral classes is performed as the estimation of the number of the clusters using the validity index (Davies and Bouldin Index) [43]. The clusters are calculate using the hierarchical method, which use the Spectral Angle measure (SAM), the Spectral Correlation measure, and the Spectral Information Divergence [85]. This process is automatically

performed by statistically toolbox of MatLab, selecting complete linkage, hierarchical and spectral commands.

5.5   Global Abundances Estimation.

Once the endmember classes are determined, the next step is to estimate their abundances. The abundances are computed by solving the abundance estimation problem AEP (see Section 2.5) using all spectral endmember signatures.

The abundance of an endmember class is the sum of the abundances of the spectral endmember signatures in that class. Constrained least squares or sparse regression are used to compute the abundance depending on whether or not there are more spectral endmember than bands as described in Section 2.5.

5.6   Analysis of Algorithm and Complexity.

The proposed computing system to implement follow, the steps depicted in Figure 5-1. Each step performs specific task, and must be analyzed separately. The first stage is the spatial subsetting using quadtree partition (see pseudo code for the partitions algorithm below). The second stage is the local estimation of the number of endmembers. The third stage is the local endmember extraction. The fourth stage is the extraction of endmember classes (clustering), and the last stage is the global abundance estimation.   This section present a complexity analysis of sacNMF.

Pseudocode for partition extraction:

```
Load image
Level = 1;
M = get Entropy (image);
[I1 I2 I3 I4] = split image (image);
```

```
M1 = get Entropy (I1);
for i=1:4
    if M1 >= M && Level ~= 3
        [Ii1 Ii2 Ii3 Ii4] = split image (I(i));
        Level = Level+1;
    end
end
```

Pseudocode for the Endmember Extraction:

```
Load partition
[m n o] = size (partition);
2dimage = reshape (partition, m*n, o);
End2 = svdss (2dimage, number);
Endmembers = 2dimage ( : , End2);
[Abd new, End new]= cNMF (2dimage, Endmembers, iter);
```

We analyze first the quadtree partitioning. When we compare the value of the Shannon entropy metric for the image and the value of the partition, the bulk of the operations are to calculate the value of the Shannon entropy (Equation 3.7). For each partition, what is limited by the other condition of the quadtree level. Therefore this part of the algorithm would be performed on a running time of $O(n)$ in the worst case [103]. But the Shannon entropy is calculate for each partition in the image and use clustering as preprocessing to calculate it. The clustering have a computational cost of $O(n^2)$. Below the pseudocode of the entropy.

Pseudocode for the Entropy Extraction:

```
Load image
[m n o] = size (image);
2dimage = reshape (image, m*n, o);
T= clusterdata(2dimage,'maxclust',Index,'linkage','ward','distance','cosine');
for i=1: Index
    Counts (i) = find (T==i)
    Total = sum (Counts);
    q = Counts. /Total;
    Entropy = -sum (q.*log (q));
end
```

In the next stage of the algorithm, we use the fitting error curve (Equation 5.2) to estimate the number of endmembers for each leave of the quadtree. In this case, we need to calculate the fitting error 20 times. The fitting error compute the Frobenious norm applied to matrix multiplications that would be performed on a running time of $O(n^3)$ in the worst case.

Pseudo code for fitting error curve:

```
Load image
[m n o] = size (image);
2dimage = reshape (image, m*n, o);
for i=2:20
    End2 (i) = svdss (2dimage, i);
    Endmembers (i) = 2dimage (:,End2(i));
    [Abd new(i), End new(i)]= cNMF (2dimage, Endmembers (i), iter);
    Imgnew (i) = End new (i)* Abd new (i);
    Error(i)=((norm(2dimage-Imgnew(i),'fro'))^2)/((norm(2dimage, 'fro'))^2);
    if Error(i) <= 0.000005
        p = index (Error (i));
    end
end
```

For local endmember extraction, we use the non-negative matrix factorization (cNMF) which is an optimization problem. Here, also we use the Frobenious norm applied to matrix multiplications that would be performed on a running time of $O(n^3)$ [103].

In extraction of the endmember classes, we use hierarchical clustering. The implementations of hierarchical clustering algorithms found in MATLAB as part of the Statistic Toolbox are used in here. The computational complexity of hierarchical clustering (including single, complete and average linkage) is $O(n^2)$ [30], where *n* is the number of samples. These algorithms are very inefficient for large datasets. But for the current application, it is expected that the computational cost of hierarchical algorithms not to affect the overall performance of the sacNMF since the obtained spectral endmembers is a small dataset of few hundred signatures.

Finally, the last part is to calculate the abundances. We use constrained least square or sparse regression using all the spectral endmembers. This involves matrix multiplications and the Frobenious norm, that would be performed on a running time of $O(\text{n}^3)$ in the worst case if the data is the dimensions m*n*o the running time will be $O(\text{m*n*o})$. As this algorithm is performed in sequential form, the running time resulting of each part is $O(\text{n}^3)$. This step is the most expensive of the process since it requires solve an optimization problem for each pixel in the image.

5.7 Summary.

This chapter described the proposed sacNMF and presented a complexity analysis. The next Chapter shows more experimental results.

6. EXPERIMENTS WITH HYPERSPECTRAL DATA.

In this chapter we present a quantitative assessment of the performance of the proposed approach. The AP Hill, Indian Pines and Cuprite images are used. Also, the Guanica for two different resolution will be analyzed, to see the effect of the change in resolution in the algorithm performance. The quantitative methodology of [43] is used here to analyze the results of the unmixing. We also compare our approach with other published methods.

In Section 6.1 we evaluate the performance of sacNMF. In section 6.2 we compare our approach using a quantitative analysis, in the section 6.2 we compare our approach with the unsupervised unmixing based on Multiscale representation (UUMR) [43], and the Spatially Adaptive Hyperspectral Unmixing (SAHU)[81] and Piece-wise convex Endmember Detection (PCE) [80]. The section 6.3 is a summary of the results.

6.1 Comparison with the existing Ground truth.

In this section we compare quantitatively with the ground truth AP Hill and Indian Pines images and include new analyses for Cuprite and Guanica PR for two resolutions. Initially we describe the quantitative results using the confusion matrix of each image, next comparing results with another methods and comparing analysis with two resolution images.

6.1.1 Methodology, Quantitative Validation for Different Images.

To assess the performance of unmixing we use the procedure similar to develop of [43]. The comparison consist of making a count (using masks) of the highlighted pixels by the abundance of each endmember class and compare it with pixels that are labeled in the ground truth for each class. With this procedure, we determine the pixels in the abundance that match with the

ground truth (true positive), pixels in the abundance but are not labeled in the class map (False positive), and the pixels that belong to the class but have zero abundance (False negative). We first compare the abundance map with the class mask. In the second comparison, a classification map is derived where each pixel is assigned to the class with the highest abundance. Confusion matrices and Kappa statistic are used to compare the maps.

We show the confusion matrices obtained for each image processed. The values of the matrices help as to calculate the overall accuracy and the Kappa statistic. We use the published class maps as ground truth and do a pixel by pixel comparison.

The tables 6-1, 6-2 and 6-3 show the classification results for AP Hill, Indian Pines and Cuprite images compared with the given ground truth, and the Tables 6-4, 6-5 and 6-6 show the number of labeled samples in each map for AP Hill, Indian Pines and Cuprite scenes.

For the APHill image the summer deciduous, loblolly pine, soil ag field, river water, grass field and gravel classes have a good results in the classification accuracy around 86.23% that is similar to the overall performance of the classification in the entire image. The behavior of the approach to detecting classes in the image was close in the percent of accuracy for each class, comparing the values obtained with the Unsupervised Unmixing based on Multiscale representation method [43]. The total pixels in the AP Hill image were 262,144 and the highest percentage of the detection were the grass field with 96.75%, and river water 95.38%. The lowest percentage were the generic road with 59.67% and shaded vegetation with 65.58%. The value of the Kappa statistic was 0.496 that mean the results have a moderate regular level. The value of the Kappa coefficient mean: values < 0 indicate no agreement and 0–0.20 slight, 0.21–0.40 fair, 0.41–0.60 moderate, 0.61–0.80 substantial, and 0.81–1 almost perfect agreement.

APHill Image											
Overall Accuracy:	86.46%										
Kappa Coefficient:	0.496										
Class	1	2	3,4,5	6	7,8,9	10	11	12	13	14	Total
1	86920	7436	142	2652	12	4	76	89	8	2	97341
2	9123	53284	76	1350	18	8	84	142	5	3	64093
3,4,5	1120	89	7001	2130	320	34	62	560	620	12	11948
6	1525	834	45	10957	3	5	2	5	8	2	13386
7,8,9	5	9	68	15	7449	2	16	18	356	2	7940
10	0	3	17	2	2	4136	13	20	967	7	5167
11	83	6	9	21	10	2	14909	365	3	1	15409
12	1624	863	460	896	128	12	18	11210	32	15	15258
13	142	12	231	274	83	2	0	0	25362	7	26113
14	10	8	17	8	2	1	11	0	0	5432	5489
Total	100552	62544	8066	18305	8027	4206	15191	12409	27361	5483	262144

Table 6-1. Confusion Matrix for the APHill Image.

Indian Pines												
Overall Accuracy:	82.69%											
Kappa Coefficient:	0.432											
Class	1	2,3,4	5,6,7	8	9	10,11,12	13	14	15	16	17	Total
1	28	0	0	13	0	0	0	0	0	0	14	55
2,3,4	0	2112	13	0	0	108	29	0	123	0	89	2474
5,6,7	0	8	715	0	0	24	0	0	58	0	45	850
8	24	0	0	455	0	0	0	0	0	0	27	506
9	0	0	0	0	4	0	0	0	0	0	2	6
10,11,12	52	63	13	0	0	3576	35	0	0	0	93	3832
13	0	83	0	0	0	63	137	0	0	0	32	315
14	0	0	0	0	0	0	0	1156	0	0	463	1619
15	0	23	145	0	0	0	0	0	97	0	64	329
16	0	0	0	0	0	0	0	0	0	91	35	126
17	124	234	321	41	3	324	123	685	31	12	9015	10913
Total	228	2523	1207	509	7	4095	324	1841	309	103	9879	21025

Table 6-2 Confusion Matrix for the Indian Pines Image.

Cuprite Image								
Overall Accuracy:			81.91%					
Kappa Coefficient:			0.421					
Class	1	2	3	4	5	6	7	Total
Kaolinite	7328	1578	883	569	824	1640	274	13096
Chalcedony	10	5958	531	234	186	162	531	7612
Calcite	28	346	9127	347	158	125	118	10249
Musc+Chlor	16	1737	2520	35554	3341	196	238	43602
Kaoli+Smec	123	1563	967	2018	17686	183	161	22701
Alunite	1632	608	632	69	1354	27556	185	32036
Rocks	63	467	1246	312	426	351	27839	30704
Total	9200	12257	15906	39103	23975	30213	29346	160000

Table 6-3. Confusion Matrix for the Cuprite Image.

#	Class	Samples
1	Summer deciduous forest	98304
2	Loblolly pine	58982
3, 4, 5	Autumn deciduous_1, 2, 3	9175
6	Green ag field	15826
7, 8, 9	Soil ag field_1, 2, 3	7864
10	Generic road	6932
11	River water	15632
12	Shaded vegetation	17093
13	Grass field	26214
14	Gravel	6122

Table 6-4. Ground truth classes for the APHill image and corresponding number of samples.

#	Class	Samples
1	Alfalfa	46
2	Corn-notill	1428
3	Corn-min	830
4	Corn	237
5	Grass-pasture	483
6	Grass-trees	730
7	Grass-pasture-moved	28
8	Hay-windrowed	478
9	Oats	20
10	Soybean-notill	972
11	Soybean-min	2455
12	Soybean-clean	593
13	Wheat	205
14	Woods	1265
15	Blgds-Grass-Trees-Drives	386
16	Stone-Steel-Tower	93
17	Background	10776

Table 6-5. Ground truth classes for the Indian Pines image and corresponding number of samples.

#	Class	Samples
1	Kaolinite	11968
2	Chalcedony	7040
3	Calcite	14080
4	Muscovite+Chlorite	45056
5	Kaolinite+Smectite	19712
6	Alunite	30976
7	Rocks	31168

Table 6-6. Ground truth classes for the Cuprite image and corresponding number of samples.

Class	Name	True Positive	False Positive	False Negative
1	summer deciduous	88.42%	54.23%	10.50%
2	loblolly pine	90.34%	36.51%	16.22%
3, 4, 5	autumn deciduous	76.31%	18.21%	20.96%
6	green ag field	69.24%	44.85%	29.51%
7, 8, 9	soil ag field	94.72%	23.52%	2.60%
10	generic road	59.67%	21.34%	33.58%
11	river water	95.38%	16.45%	3.45%
12	shaded vegetation	65.58%	45.13%	29.61%
13	grass field	96.75%	12.67%	3.12%
14	gravel	88.73%	33.15%	8.63%

Table 6-7. Agreement between class mask and abundance maps for AP Hill.

Class	Name	True Positive	False Positive	False Negative
1	Alfalfa	61.23%	10.23%	6.57%
2, 3, 4	Corn-min, notill, clean	84.63%	33.28%	10.25%
5, 6, 7	Grass/pasture, tree, moved	57.63%	10.64%	45.32%
8	Hay windrowed	95.34%	10.20%	3.45%
9	Oats	18.33%	72.30%	44.63%
10, 11, 12	Soybean-min, notill clean	88.96%	28.65%	16.54%
13	Wheat	66.78%	41.91%	12.56%
14	Woods	91.36%	68.23%	53.21%
15	Bldg-Grass-Tree-Drive	25.12%	13.25%	56.34%
16	Stone-stell towers	98.30%	8.23%	2.15%
17	Background	83.65%	33.25%	23.59%

Table 6-8. Agreement between class mask and abundance maps for Indian Pines.

Class	Name	True Positive	False Positive	False Negative
1	Kaolinite	61.23%	30.32%	37.98%
2	Chalcedony	84.63%	58.18%	11.15%
3	Calcite	64.82%	57.23%	35.41%
4	Muscovite + Chlorite	78.91%	40.32%	18.19%
5	Kaolinite + Smectite	89.72%	62.58%	10.13%
6	Alunite	88.96%	38.45%	12.33%
7	Rocks & Others	89.32%	8.15%	13.47%

Table 6-9. Agreement between class mask and abundance maps for Cuprite.

For the Indian Pines image, the corn-min-notill-clean, hay windrowed, soybean-min-notill-clean, woods, stone steel tower, and background classes had good results in the classification around 82.69% of the overall performance of the classification in the entire image. The behavior of the approach to detecting classes in the image was close in the percentage of accuracy for each class comparing the values obtained with the Spatially Adaptive Hyperspectral Unmixing method, if only compare the based on the classes used for this method that were 6 classes, basically the bare soil class include all the crops in the Indian Pines image, and the vegetation include the woods and background detecting individually in our approach.

This image has 21,025 pixels. The highest percentage of the detection were Stone Steel tower class with 98.30%, and the Hay windrowed class with 95.34%. The lowest percentage were the Oats class with 18.33% and the Bldg-Grass-Tree-Drive class with 25.12%.

In the Cuprite image as other following analysis, we could detect classes that did not appear in the ground truth (rocks) and is well defined in the local approach. The piece of image have a 160,000 pixels, the overall accuracy was 81.91%. The highest percentage were Kaolinite+Smectite with 89.72%, and Rocks with 89.32%. The lowest percentage were the Kaolinite single with 61.23% and Calcite with 64.82%

In the next section, we compare these results with other published methods apply to the same images.

6.2   Comparing with other Methods.

This section presents first the comparative analysis of the cNMF and sacNMF results for the Cuprite image. Then we compare the results with other methods and for other images. A qualitative comparison with two unmixing methods that take into account the spatial information other convex method that perform unmixing. Each method work with different images. To compare results using APHill and Cuprite image we use the Unsupervised Unmixing based on Multiscale Representation. For the Indian Pines image, we compare with Spatially Adaptive Hyperspectral Unmixing (SAHU) and Piece-wise Convex Endmember Detection (PCE).

6.2.1 cNMF and sacNMF results for Cuprite.

In this section, we analyze the Cuprite image to evaluate the behavior of the approach. Thus in an image of elevated complexity in the mixed classes. Figure 6-1 shows the quadtree partitioning using Shannon entropy, Thirty seven tiles was obtained. Figure 6-2 shows results with cNMF and Figure 6-3 with sacNMF.

Results in figures 6-2 and 6-3 show that sacNMF extracts more classes than the global analysis. With cNMF we detected 15 classes, and with the sacNMF we can extracted 18 endmember classes with 169 spectral endmembers. In Figures 6-4 and 6-5 we can see four examples of the endmember classes that are extracted with sacNMF the Rocks, Muscovite-Chlorite and Alunite and Chalcedony can be separate very well.
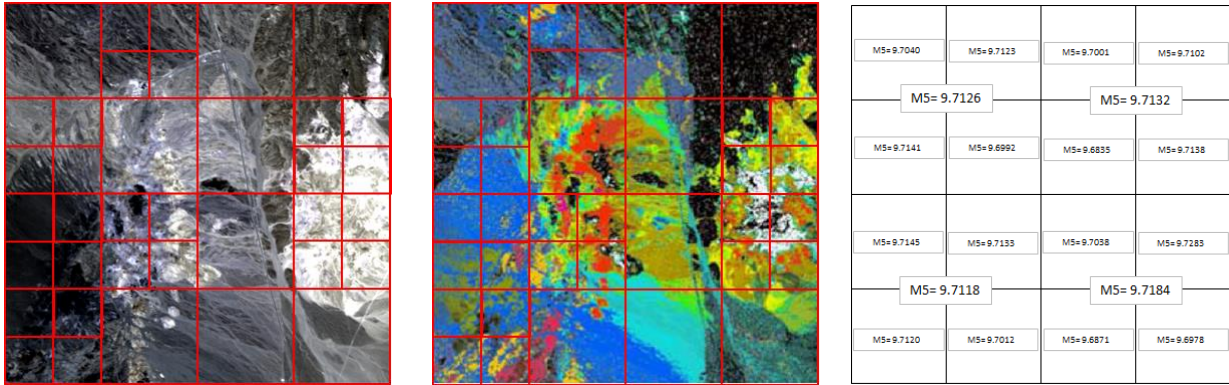
Figure 6-1. Cuprite quadtree Partitioning with norm of the Shannon Entropy. Global index M3 = 9.7103.

a) Class 1 b) Class 2 c) Class 3 d) Class 4

e) Class 5 f) Class 6 g) Class 7 h) Class 8

i) Class 9 j) Class 10 k) Class 11 l) Class 12

m) Class 13 n) Class 14 o) Class 15
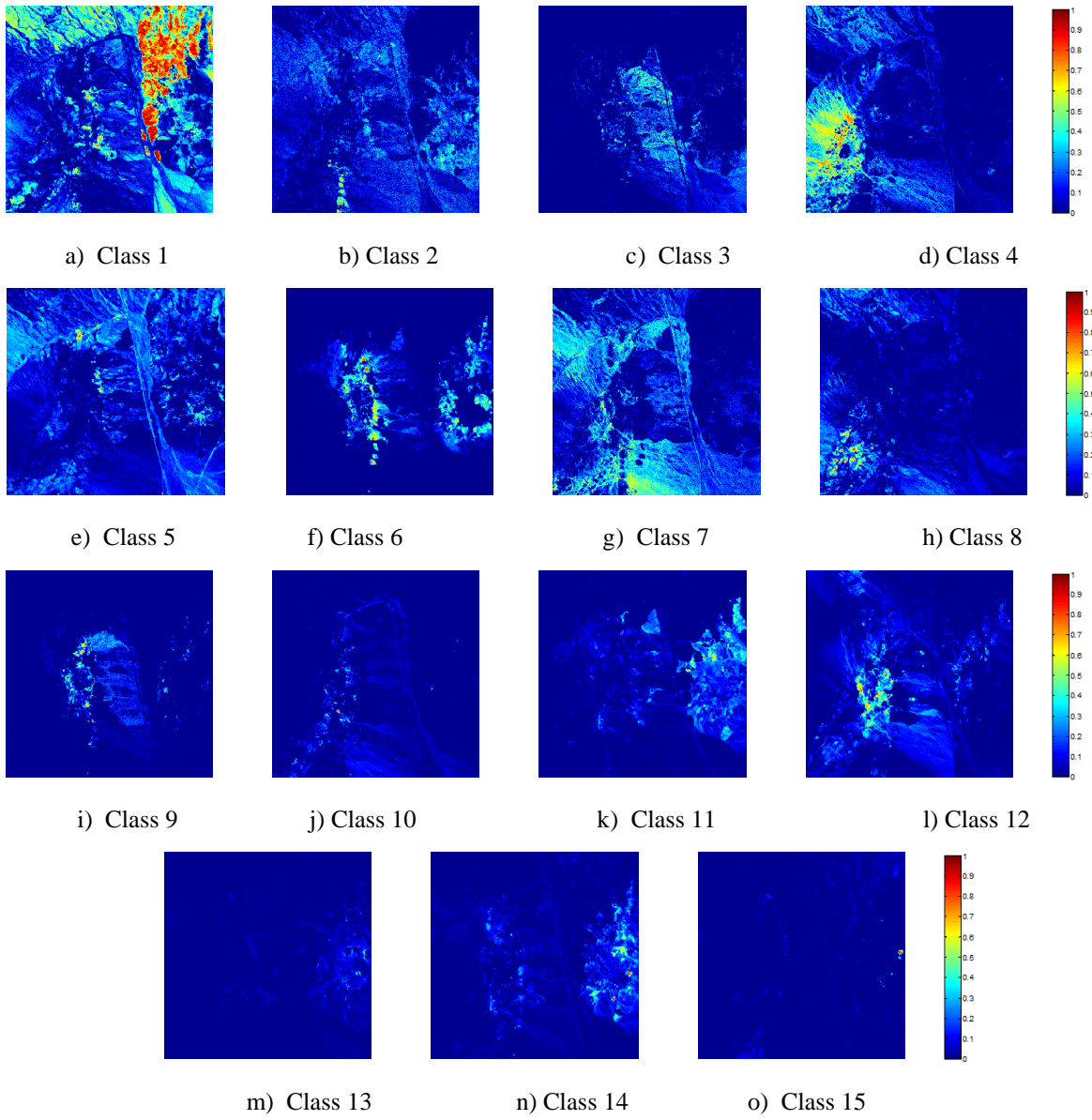
Figure 6-2. Abundances resulting from cNMF with the ground truth for Cuprite image.

a) Class 1   b) Class 2   c) Class 3   d) Class 4

e) Class 5   f) Class 6   g) Class 7   h) Class 8

i) Class 9   j) Class 10   k) Class 11   l) Class 12

m) Class 13   n) Class 14   o) Class 15
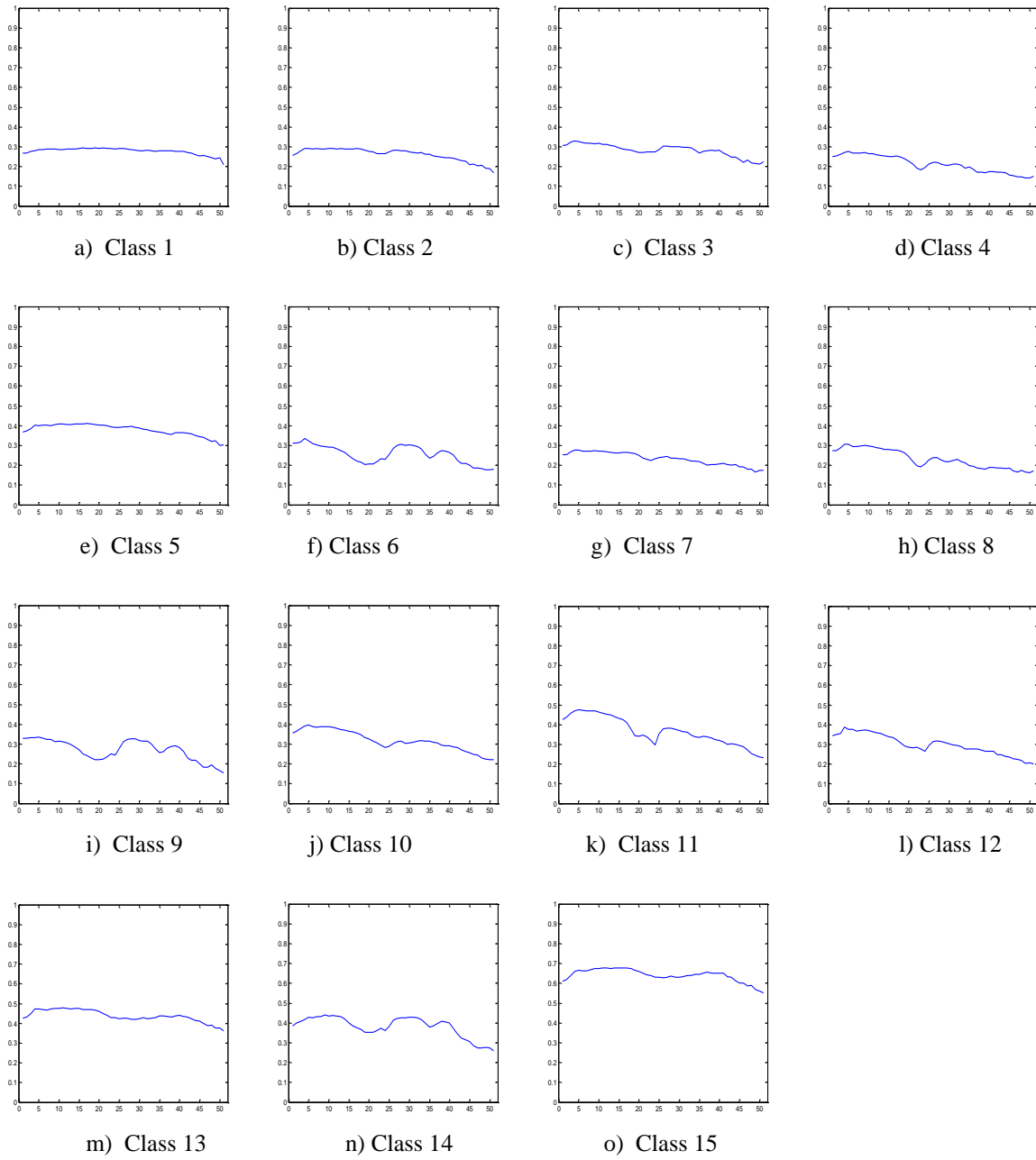
Figure 6-3. Endmember resulting from cNMF with the ground truth for Cuprite image.

a) Class 1   b) Class 2   c) Class 3   d) Class 4

e) Class 5   f) Class 6   g) Class 7   h) Class 8

i) Class 9   j) Class 10   k) Class 11   l) Class 12

m) Class 13   n) Class 14   o) Class 15   p) Class 16

q) Class 17   r) Class 18
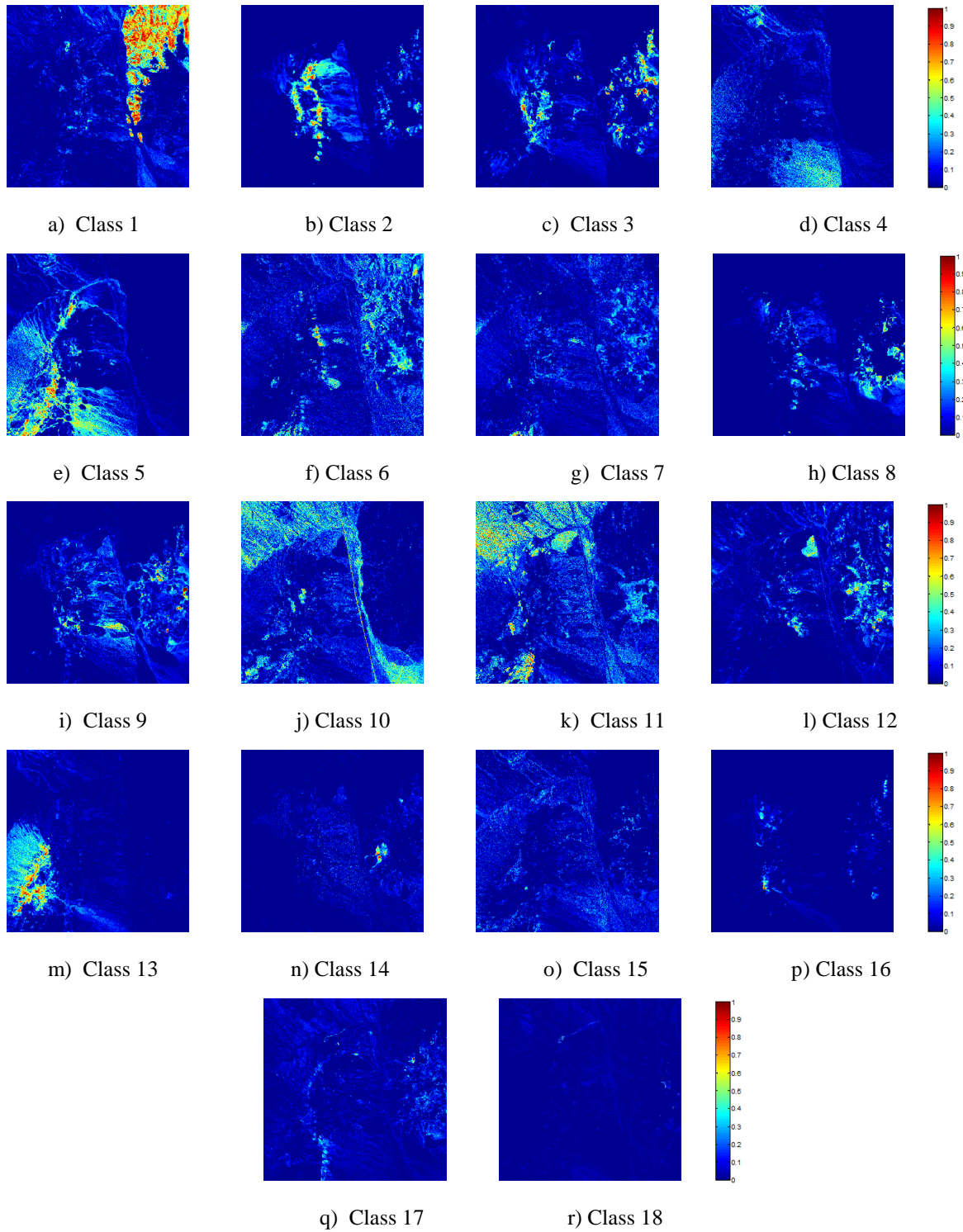
Figure 6-4. Abundances resulting from sacNMF and clustering with the ground truth for Cuprite image.

a) Class 1   b) Class 2   c) Class 3   d) Class 4

e) Class 5   f) Class 6   g) Class 7   h) Class 8

i) Class 9   j) Class 10   k) Class 11   l) Class 12

m) Class 13   n) Class 14   o) Class 15   p) Class 16

q) Class 17   r) Class 18
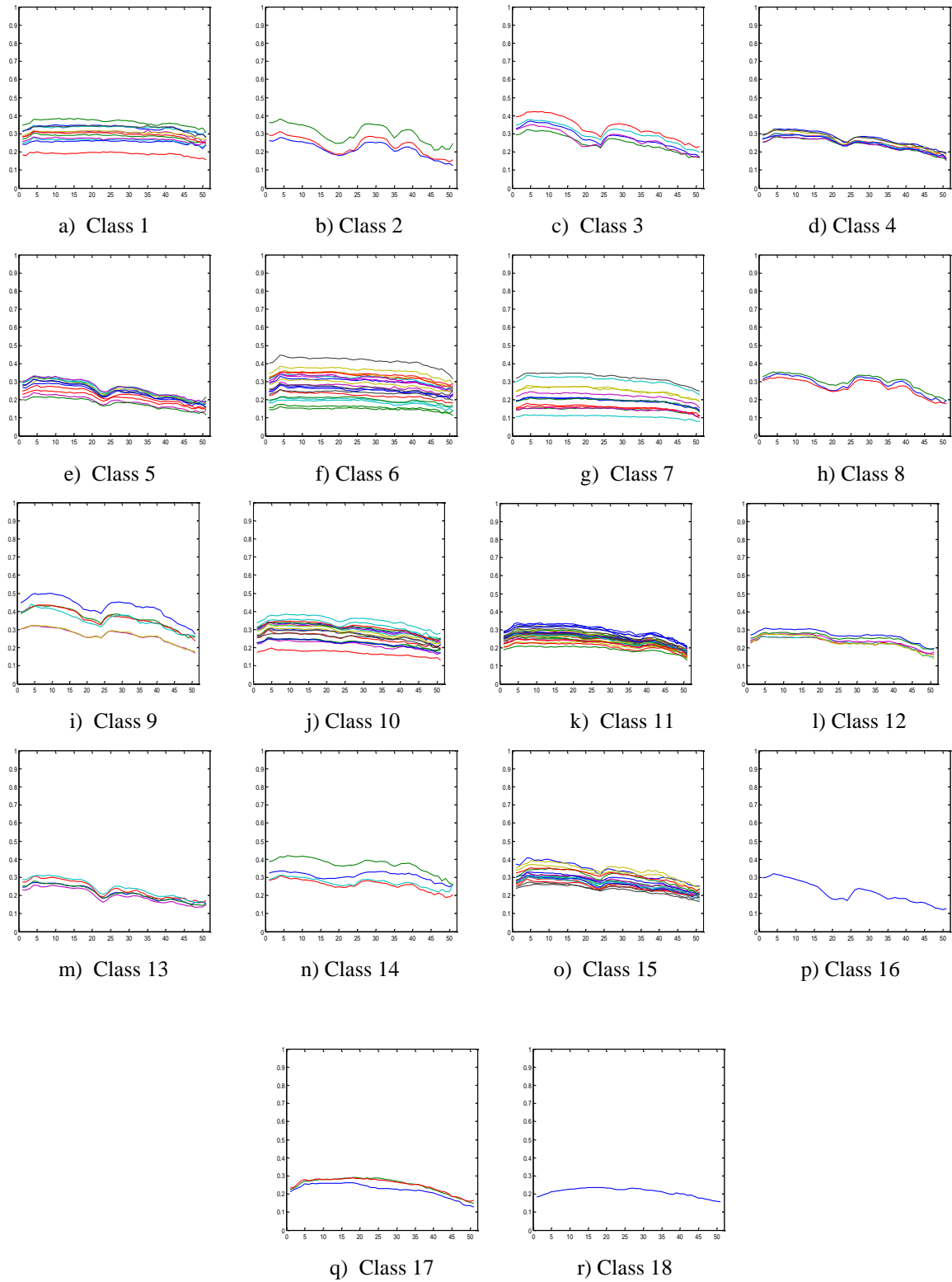
Figure 6-5. Endmember classes resulting from the sacNMF and clustering with the ground truth for Cuprite image.

120

Global   Local

**Rocks &
Muscovite
+Chlorite**

Cuprite, Nevada
AVIRIS 1995 Data
USGS
Clark & Swayze
Tetracorder 3.3 product

Sulfates
- K–Alunite 150c
- K–Alunite 250c
- K–Alunite 450c
- Na82–Alunite 100c
- Na40–Alunite 400c
- Jarosite
- Alunite+Kaolinite and/or Muscovite

Kaolinite group clays
- Kaolinite, wxl
- Kaolinite, pxl
- Kaolinite+smectite or muscovite
- Halloysite
- Dickite

Carbonates
- Calcite
- Calcite +Kaolinite
- Calcite + montmorillonite

Clays
- Na–Montmorillonite
- Nontronite (Fe clay)

other minerals
- low–Al muscovite
- med–Al muscovite
- high–Al muscovite
- Chlorite+Musc,Mont
- Chlorite
- Buddingtonite
- Chalcedony: OH Qtz
- Pyrophyllite +Alunite

2 km   N

**Alunite &
Kaolinite**

Figure 6-6. Abundances of Endmember classes resulting from the Global (cNMF) versus Local unmixing analysis (sacNMF) with the ground true for Cuprite image.

121

Global   **Local**   **Ground**

Muscovite +Chlorite

Alunite & Chalcedony

Cuprite, Nevada
AVIRIS 1995 Data
USGS
Clark & Swayze
Tetracorder 3.3 product

Sulfates
- K–Alunite 150c
- K–Alunite 250c
- K–Alunite 450c
- Na82–Alunite 100c
- Na40–Alunite 400c
- Jarosite
- Alunite+Kaolinite and/or Muscovite

Kaolinite group clays
- Kaolinite, wxl
- Kaolinite, pxl
- Kaolinite+smectite or muscovite
- Halloysite
- Dickite

Carbonates
- Calcite
- Calcite +Kaolinite
- Calcite + montmorillonite

Clays
- Na–Montmorillonite
- Nontronite (Fe clay)

other minerals
- low–Al muscovite
- med–Al muscovite
- high–Al muscovite
- Chlorite+Musc,Mont
- Chlorite
- Buddingtonite
- Chalcedony: OH Qtz
- Pyrophyllite +Alunite

2 km   ↑ N

Figure 6-7. Abundances of Endmember classes resulting from the Global (cNMF) versus Local unmixing analysis (sacNMF) with the ground true for Cuprite image.

6.2.2 Unsupervised Unmixing based in Multiscale Representation (UUMR).

This method proposed in [43] takes advantage of the sampling operation used to build the coarse grids in a multigrid diffussion method. The endmember extraction method exploits the multigrid structure at the selected scale to determine the spectral endmembers. This technique extracts spectral signatures and spectral endmember classes from hyperspectral imagery in an unsupervised fashion. The spatial-spectral unmixing approach obtains benefit of multiscale

representation for the determination of the spectrally uniform regions and their representative spectra avoiding the explicit segmentation of the hyperspectral image [43].

The results obtained with this method and published in [43] show similar results than the obtained with our approach. The resulting endmember classes in our method were 18 and the classes obtained with UUMR was 17 classes for the Cuprite Image (see Figures 6-8 and 6-9). For the AP Hill image, the classes obtained by our method was 11 (see Figures 6-11 and 6-12), while UUMR was 14.

These method, works in the same way using the clustering to grouping the obtained endmembers. The clustering problem is that sometimes fail to group the same classes, but the local information can extract a lot of the different material present in the scene. Both process can determinate the similar endmember classes in Cuprite image, but this endmember classes represent mix classes in the ground true image (Figure 6-1), and in the AP Hill image our method mix the soil and the autumn classes, while UUMR detects several classes by river water (Figure 6-3) and our results mix the summer deciduos forest with green ag field that is separate in Multiscale method.
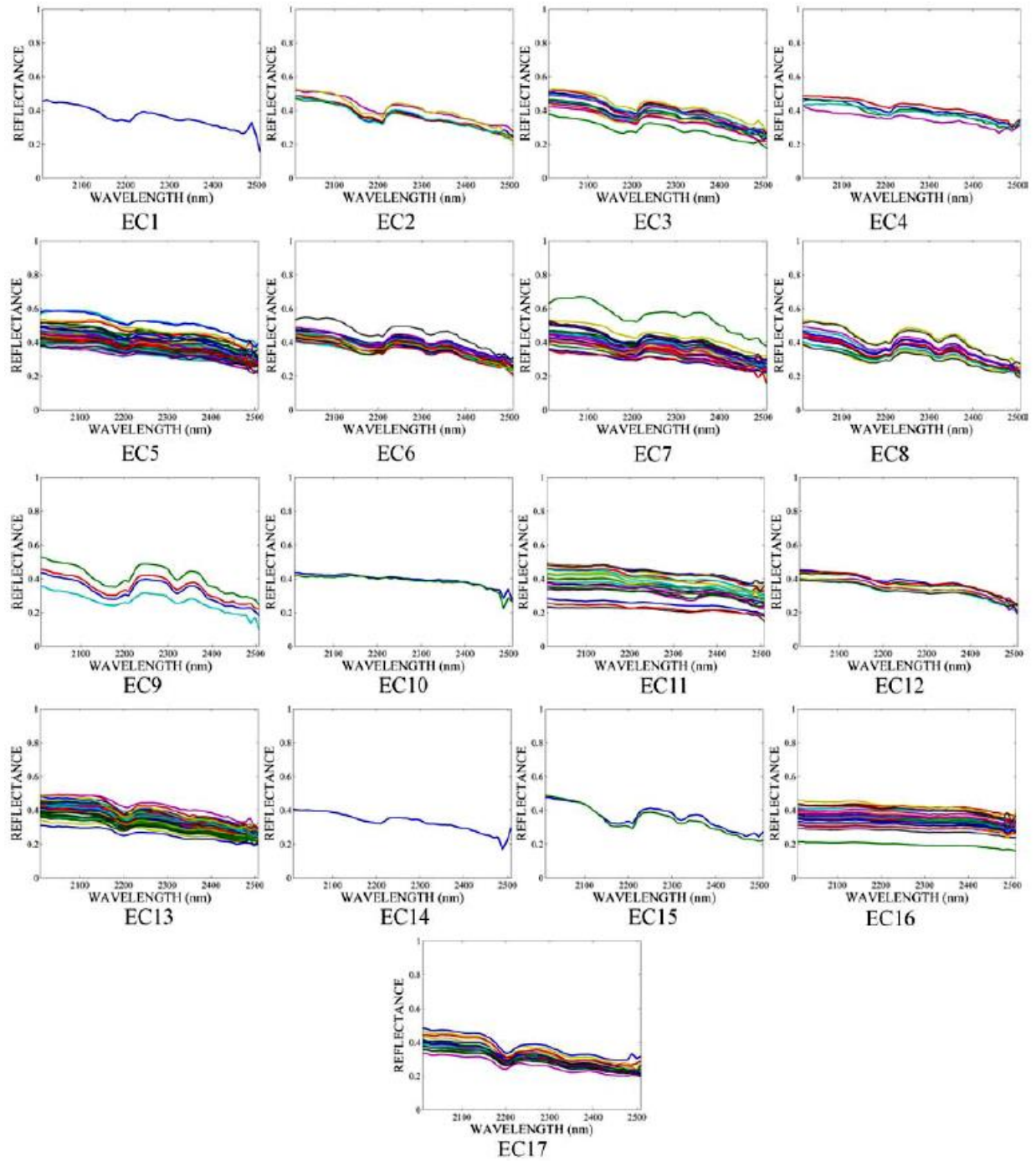
Figure 6-8. Endmembers classes resulting from Unsupervised Unmixing based in Multiscale Representation for Cuprite image [43].
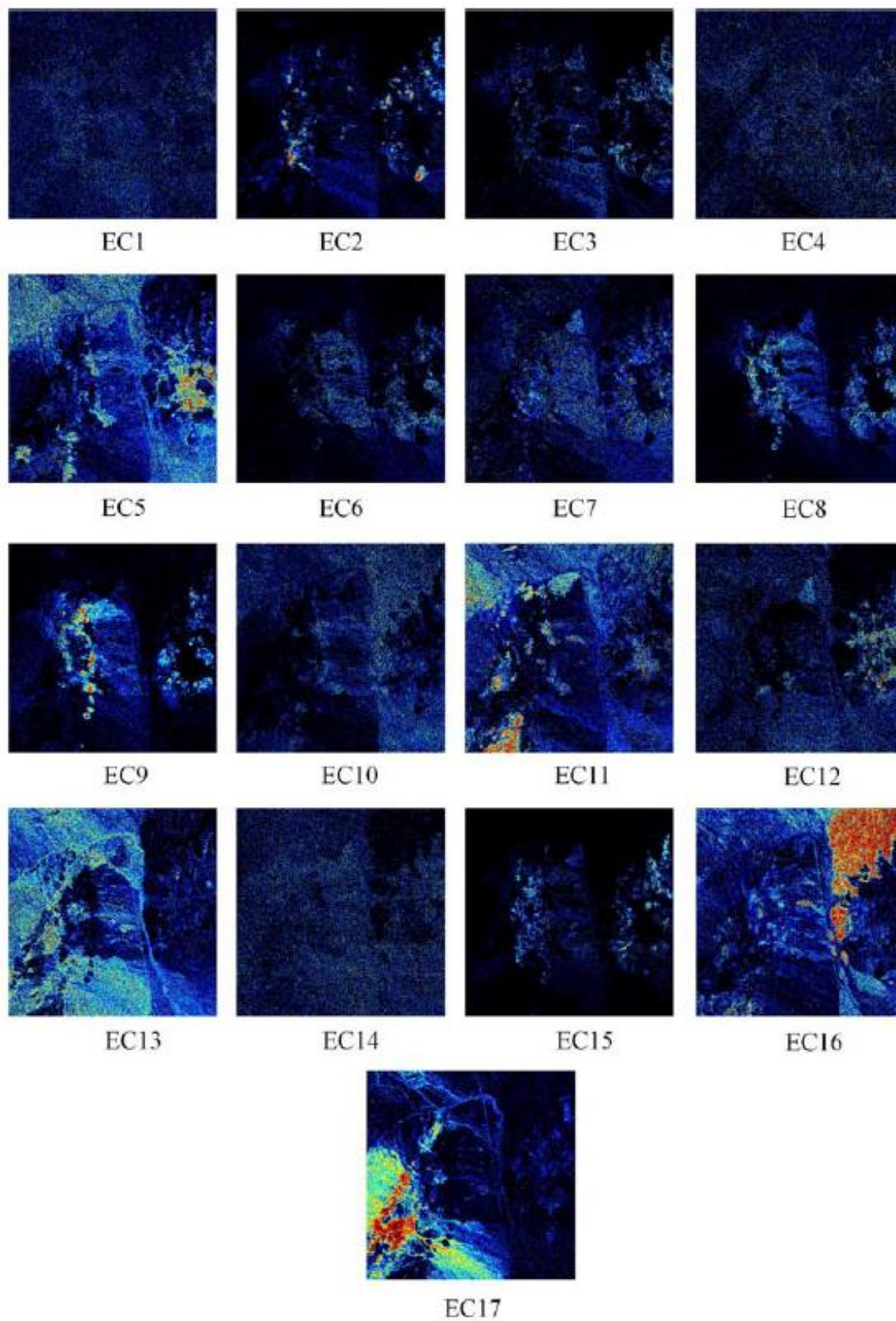
Figure 6-9. Abundances resulting from Unsupervised Unmixing based in Multiscale Representation for Cuprite image [43].

125
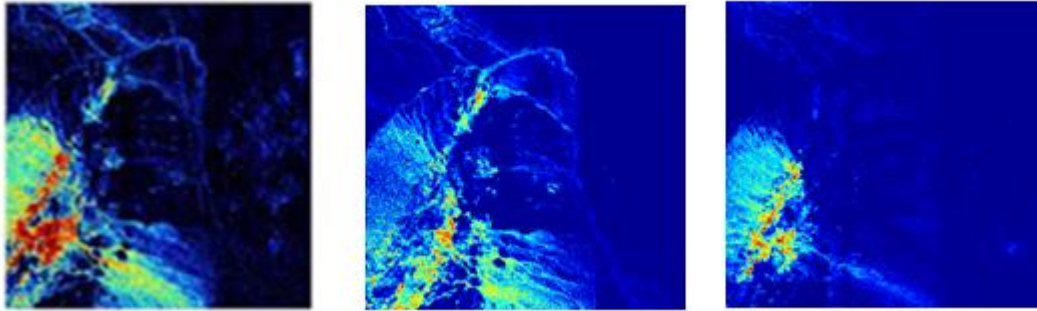
a) Calcite & Muscovite
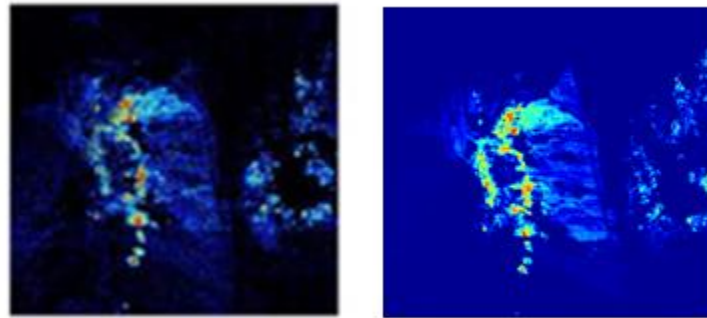
b) Alunite
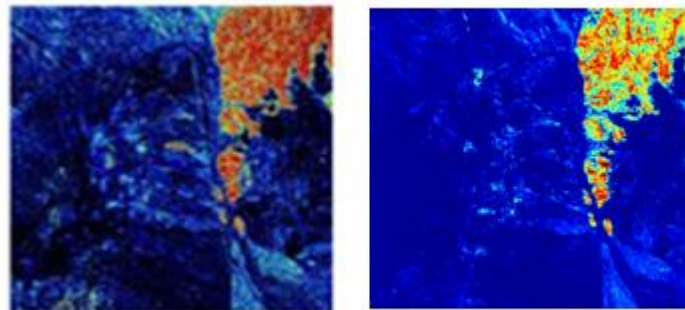
c) Rocks
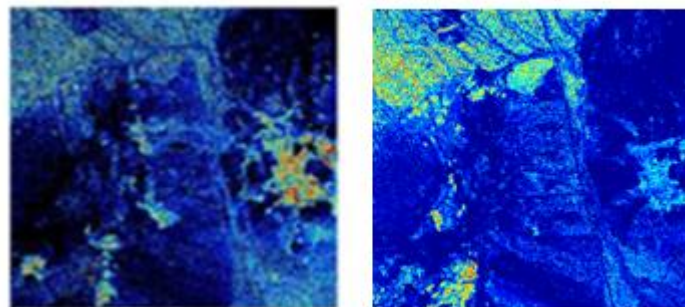
d) Chalcedony

Figure 6-10. Examples of comparison results between the UUMR and our approach. Calcite & Muscovite, Alunite, Rocks and Chalcedony [43].

In Figure 6-10, we can see how the two methods can separate the same classes and our method divide a same class in two clusters. The Cuprite image is a very complex image, but both methods obtain good results for unmixing. The overall accuracy for the UUMR in this image was 46.12%, and in our approach was 81.91%. These differences is a con sequence that our method separates more classes than the UUMR and we considered the rock class, in the calculus. On the other hand the specific accuracy per class are similar in all classes, Kaolinite (62.42% vs 61.23%), Chalcedony (87.45% vs 84.63%), Calcite (75.94% vs 64.82), Muscovite + Chlorite (76.09% vs 78.91%), Kaolinite + Smectite (88.70% vs 89.72%) and Rocks (our approach 89.32%, UUMR did not extracted).
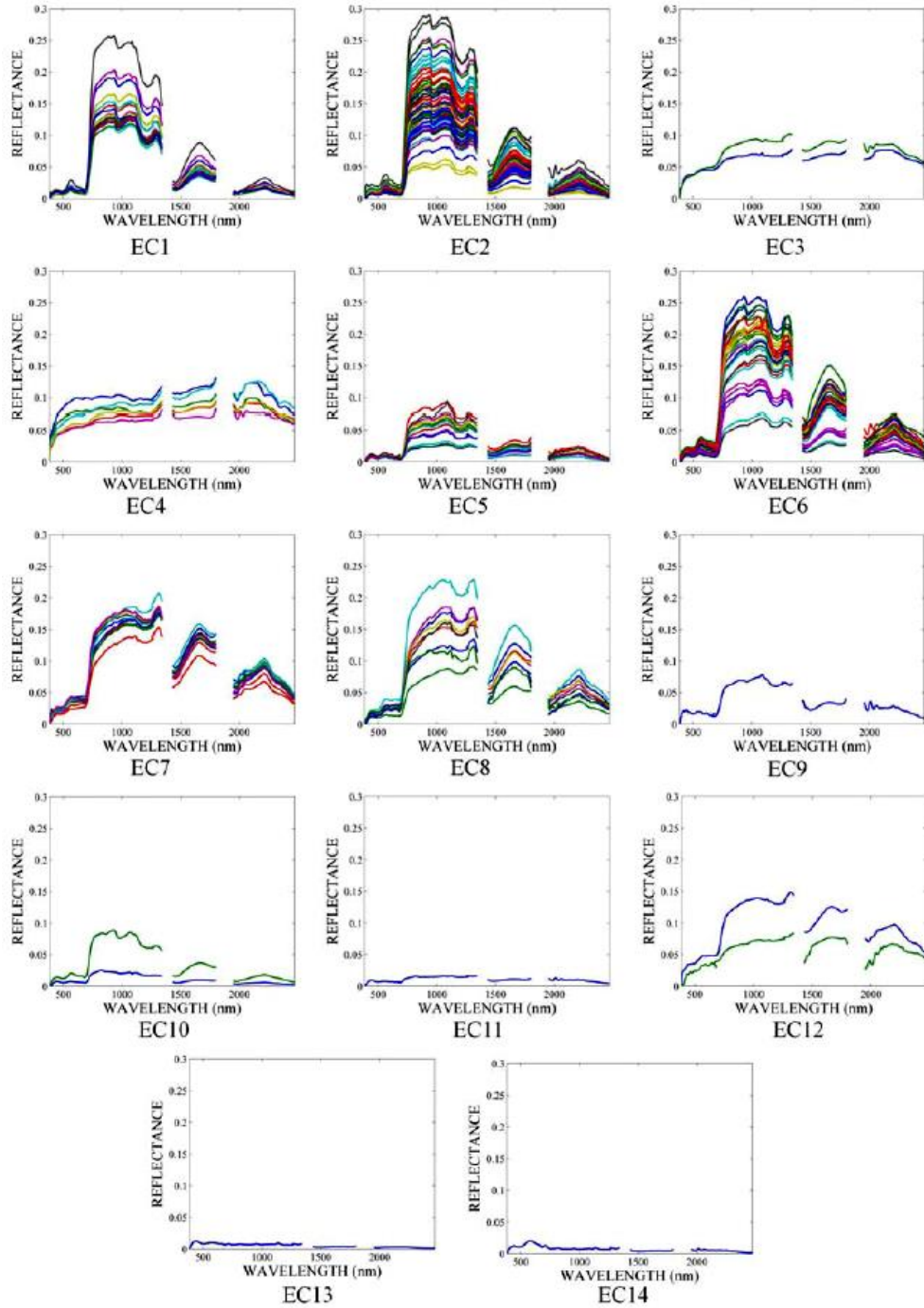
Figure 6-11. Endmember classes UUMR for APHill from [43].
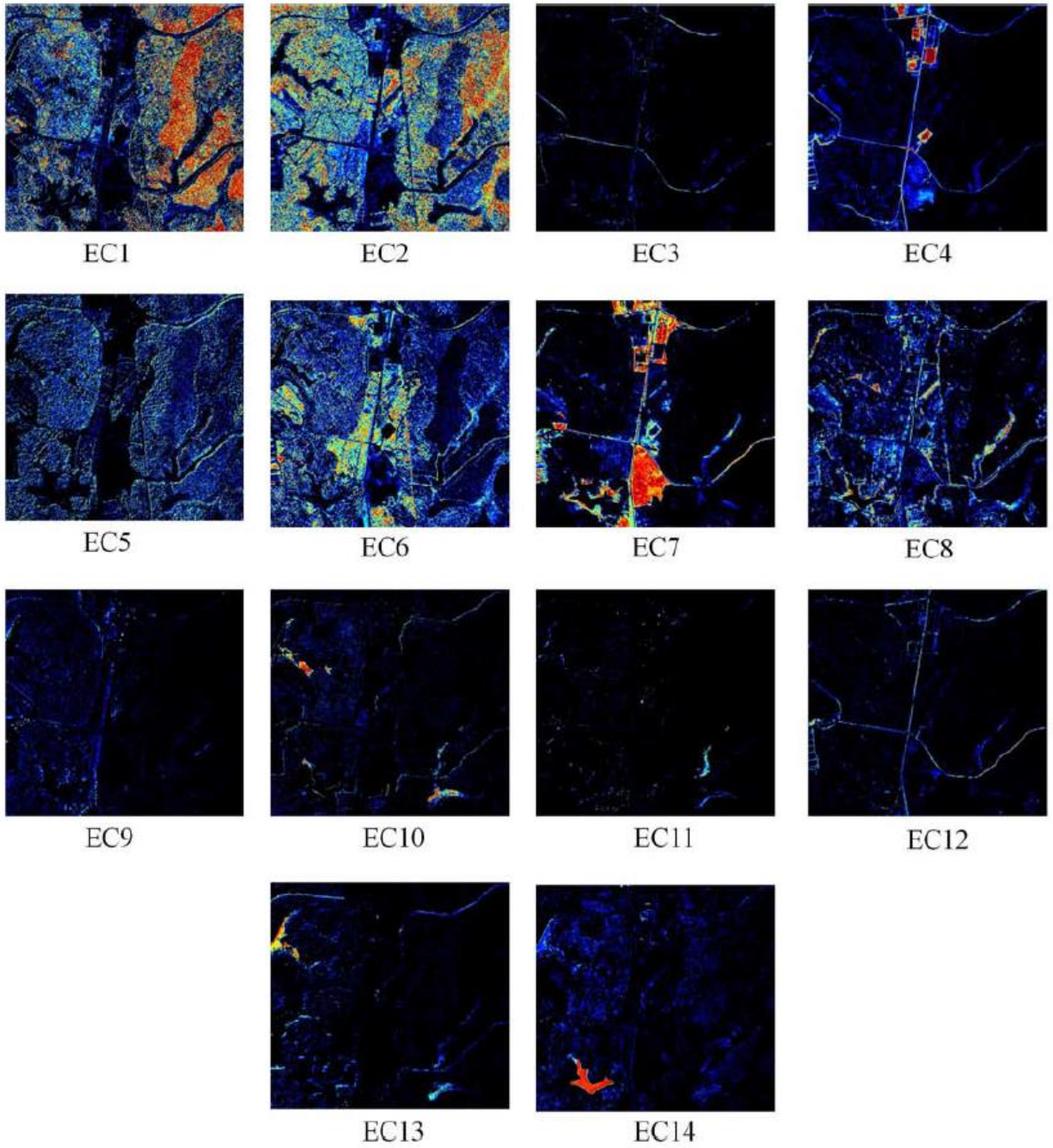
Figure 6-12. Abundances resulting from UUMR for APHill image from [43].
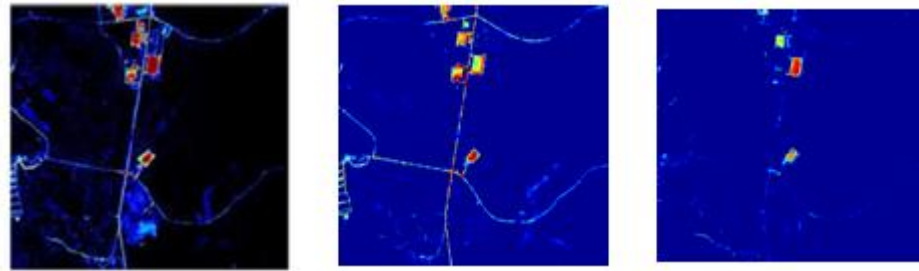
a) Roads & Gravel
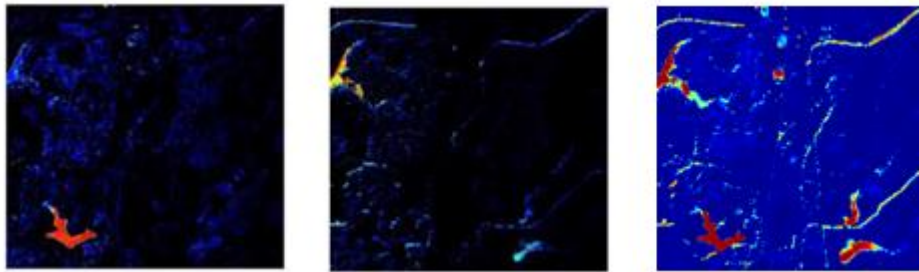
b) River Water
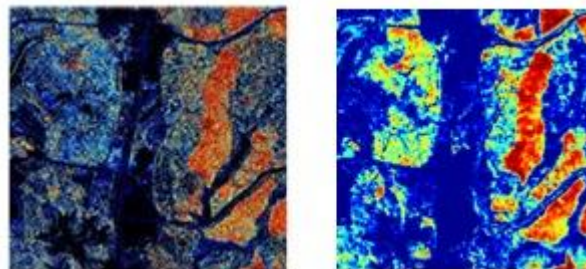
c) Loblolly pine
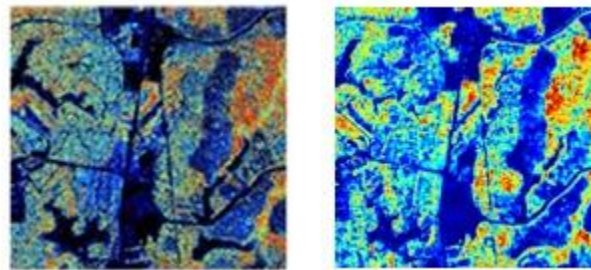
c) Summer deciduous forest

Figure 6-13 Comparison between the UUMR and our approach for, Roads & Gravel, River Water, Loblolly pine and Summer deciduous forest classes [43].

In Figure 6-13, we can see that the two methods can separate the same classes and our method divides the road class in two clusters, the road and buildings, and the gravel classes. The UUMR mixes these two classes. While for the river water class, the opposite occurs we detect only one cluster for it, but UUMR divided it in two clusters. Both methods obtain similar results for AP

Hill in the unmixing. The overall accuracy for the UUMR in this image was 50.5%, and in our approach was 86.46%. Our method can separate more classes than the other and we considered the rock class in the calculus. On the other hand, the accuracies in same class are similar in all classes, Loblolly pine (89.9% vs 90.34%), Summer deciduous (91.8% vs 88.42%), Autumn deciduous (74.8% vs 76.31), Green ag field (68.3% vs 69.24%), Soil (98.9% vs 94.72%), River water (97.3% vs 95.38), Grass field (97.6% vs 96.75), and Shaded vegetation (86.4 vs 65.58%).

6.2.3 Spatially Adaptive Hyperspectral Unmixing and Piece-wise Convex Endmember Detection.

In this section, we review published results of the Spatial Adaptive Hyperspectral Unmixing approach (SAHU) [81] and the Piece-Wise Convex Endmember (PCE) methods [80], and comparing with the obtained in our approach using the Indian Pines Image.

SAHU [81] performs spectral unmixing using a spatially adaptive approach, dividing a image in partitions (subsets) such that these partitions are used to identify local endmembers. Linear unmixing is performed per pixel with endmembers identified at the local level, but global abundance maps are created by clustering the locally determined EMs into common groups. This method uses the MaxD algorithm [21] for determination the local endmembers. Abundances are estimated in each partition using local endmembers, and similar endmembers are clustered to determine global abundances. The number of endmembers are estimated using a methodology based on the Gram matrix method [81]. For this method, 7 clusters are obtained where the abundances for these clusters mixes the background with woods (vegetation) or the background with roads (Pavement or gray bare soil), another class is bare soil that correspond to all crops in

the landscape, roof correspond, to the stone steel tower class, the wet bare soil correspond the area

of hay-windrowed and background, and specular reflection.
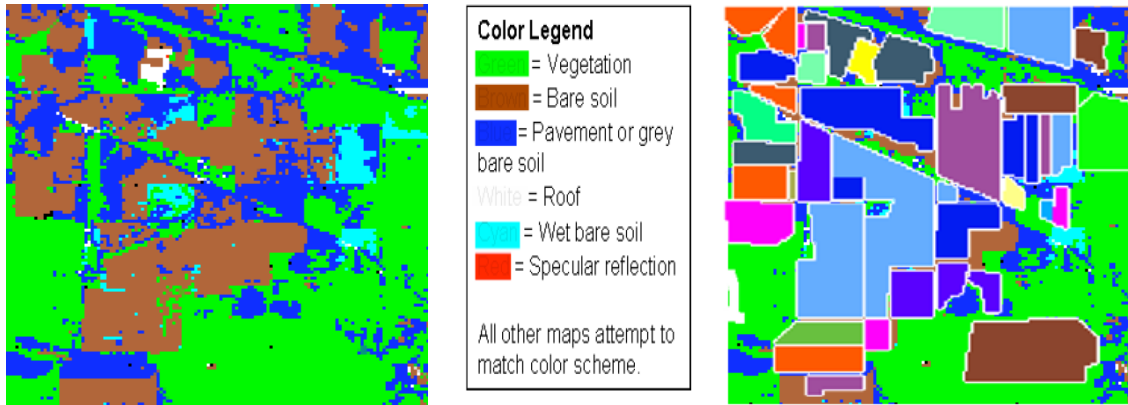
Figure 6-14. Results obtained using the spatially Adaptive Hyperspectral Unmixing from Indian Pines Image [81].

If we comparing the Indian Pines results with those from our approach the classification

performed by this method was focused on separating the global classes in the scene maintaining

similar classes toghether. In ours, we can obtain more details in the vegetation classes, bare soil

and background classes.

The PCE method [80] is an unmixing technique based on the partitioning of spectral data

into several convex regions. With this method, the 16 classes were found for the Indian Pines

image with a total of 14 endmembers. Combinations for the 14 endmembers with diferent percents

show the abundances result. The corn and soybean classes (notill, min and clean) for example, are

compossed by endmebers 2, 6, and 10 with different abundances. Other classes obtained by the

endmembers represent the asigned ground truth very well in more than 70%, and others

endmembers represent almost the 89% of the abundances (eg. Hay-windrowed, Oats and Wheat).

For the remaining classes, the abundances are mixtures for two o more endmembers.

a) Woods, Grass/Pasture and Tree b) Hay-windrowed, Alfalfa and Grass c) Corn & Soybean

d) Stone-steel towers e) Corn & Soybean f) Woods, Blgd-Grass/Tree/Drives
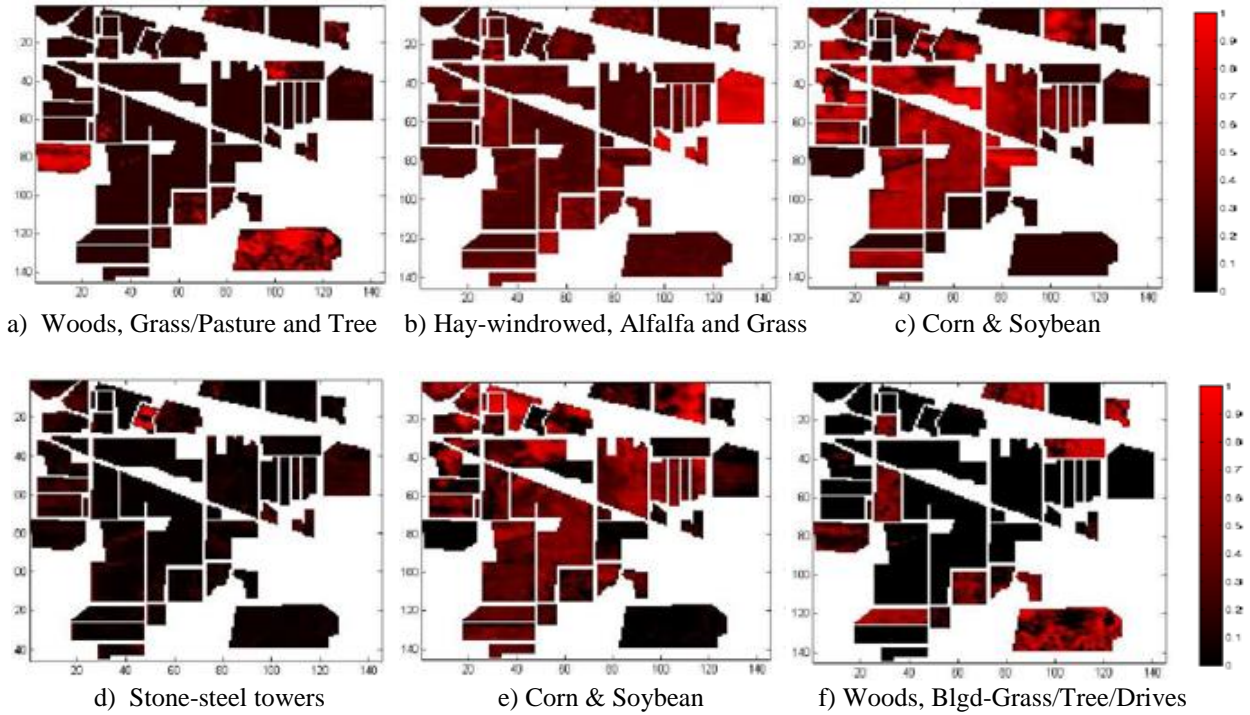
Figure 6-15. Results obtained using the Piece-wise Convex Endmember Detection from Indian Pines Image [80].

Table 6-10 Comparative Results for different methods.

Item	Class Name	Global NMF	saNMF	PCE	SAHU
0	Roads	3, 4, 7	12	-	Pavement
1	Background	1, 3, 4, 5, 8	1, 2, 12	14	Vegetation
2	Alfalfa	2	6	2, 7,8	Bare soil
3	Corn-notill	1, 2	5, 7	2, 6, 10	Bare soil
4	Corn-min	1, 8	7	2, 6, 10	Bare soil
5	Corn	1	7	2, 6, 7, 10	Bare soil
6	Grass/Pasture	3, 6	3	2, 3, 7, 10	Bare soil
7	Grass/Trees	4, 5	1	7, 10, 11	Bare soil
8	Grass/pasture-moved	2	3	8	Bare soil
9	Hay-windrowed	2	9	8	Wet baresoil
10	Oats	-	-	7	Bare soil
11	Soybeans-notill	1, 8	10, 11	2, 10	Bare soil
12	Soybeans-min	1, 8	7, 10	2, 6, 10	Bare soil
13	Soybeans-clean	1	11	2, 6, 10	Bare soil
14	Wheat	3, 5, 6	8	9	Bare soil
15	Woods	3	2	3, 5	Vegetation
16	Bldg-Grass-Tree-Drives	3	1	2, 3, 5, 7, 8, 9	Vegetation
17	Stone-steel towers	7	4	4, 6, 13	Roof
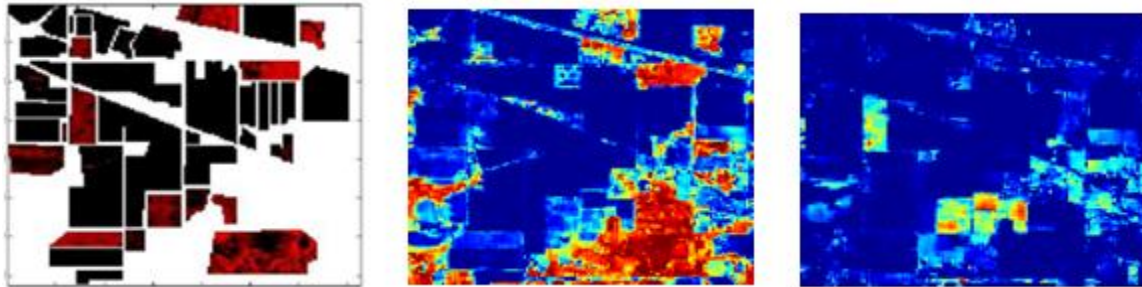
a) Woods, Wheat, Grass Tree & Bldg Grass Tree Drive.
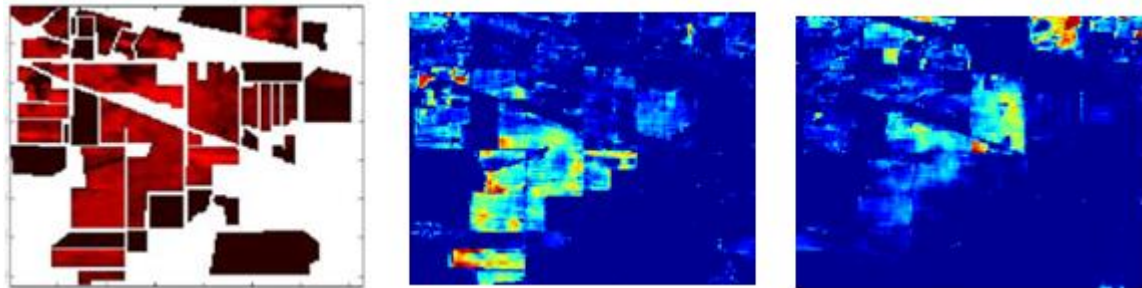
b) Corn & Soybeans.
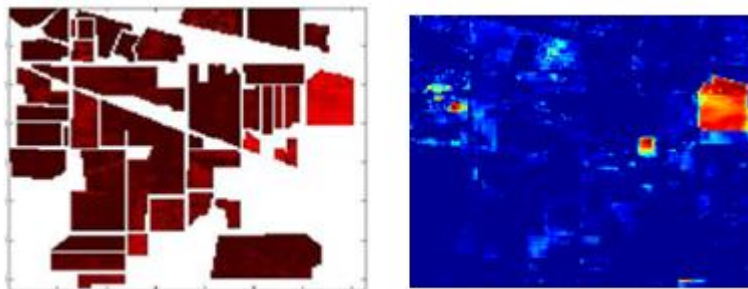
c) Alfalfa & Hay-windrowed
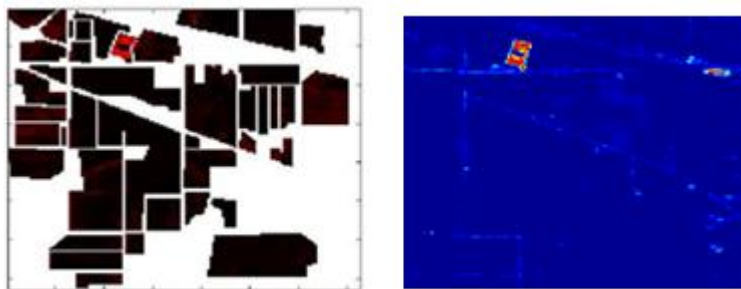
4) Stone Steel towers.

Figure 6-16. Comparison results between the Piece-wise Convex Endmember Detection and our approach in the Indian Pines image. 1) Woods, Wheat, Grass Tree & Bldg Grass Tree Drive. 2) Corn & Soybeans. 3) Alfalfa & Hay-windrowed. 4) Stone Steel towers [80].

In Table 6-10, we have a summary comparing PCE, SAHU, cNMF and our approach. Our approach identify more endmember classes in the entire image including classes not taken into account by the ground truth like roads and other background. In the Figure 6-16 we have four comparison between the PCE method and our approach. Again our method can detect more classes than the other and separate then during clustering.

Table 6-11. Comparison with other methods for APHill Hyperspectral Image [43]

APHill Image	True Positive Rate (%)				False Positive Rate (%)			
Class	sacNMF	UUMR	SMACC	RBSPP	sacNMF	UUMR	SMACC	RBSPP
summer deciduous	88.42	91.8	99.6	100	54.23	67.3	88.3	74.7
loblolly pine	90.34	89.9	97.9	89	36.51	37.7	53.7	42.4
autumn deciduous	76.31	74.8	no detect	no detect	18.21	20.8	no detect	no detect
green ag field	69.24	68.3	96.9	no detect	44.85	52.9	48.1	no detect
soil ag field	94.72	98.9	99.9	99.8	23.52	22.3	58.1	17.1
generic road	59.67	in soil	in soil	in soil	21.34	in soil	in soil	in soil
river water	95.38	97.3	57.2	87.1	16.45	19.1	56.6	1.4
shaded vegetation	65.58	86.4	13.8	18.5	45.13	39.7	16.8	1.2
grass field	96.75	97.6	99.6	100	12.67	14.1	26.4	97.5
gravel	88.73	in soil	in soil	in soil	33.15	in soil	in soil	in soil

In the table 6-11 we can see the results when we compare our method with other methods presented in [43].

6.3 Effects of Spatial Resolution.

Unmixing results for two hyperspectral images from the Guanica Forest (see Section 2.10) are used to evaluate the performance with respect to spatial resolution.

6.3.1 Testing Guanica Image for different Resolutions.

Applying the algorithm to Guanica images at 1m and 4m, the results for cNMF and sacNMF are observed below. Initially the resulting partitions are showed followed by the obtained abundances and endmembers. The image was divided in 16 tiles, using the norm of the Shannon entropy as split criterion, and 9 endmember classes (51 spectral endmembers) were obtained by sacNMF versus 7 endmembers using cNMF.

Figure 6-17. Quadtree partitioning using norm of the Shannon Entropy with global index M5 = 8. 5589 for Guanica at 4m resolution.

a) Building & Road

b) Road

136

c) Building & Road   d) Low Vegetation

e) Grass Field   f) Tall Vegetation

g) Tall Vegetation
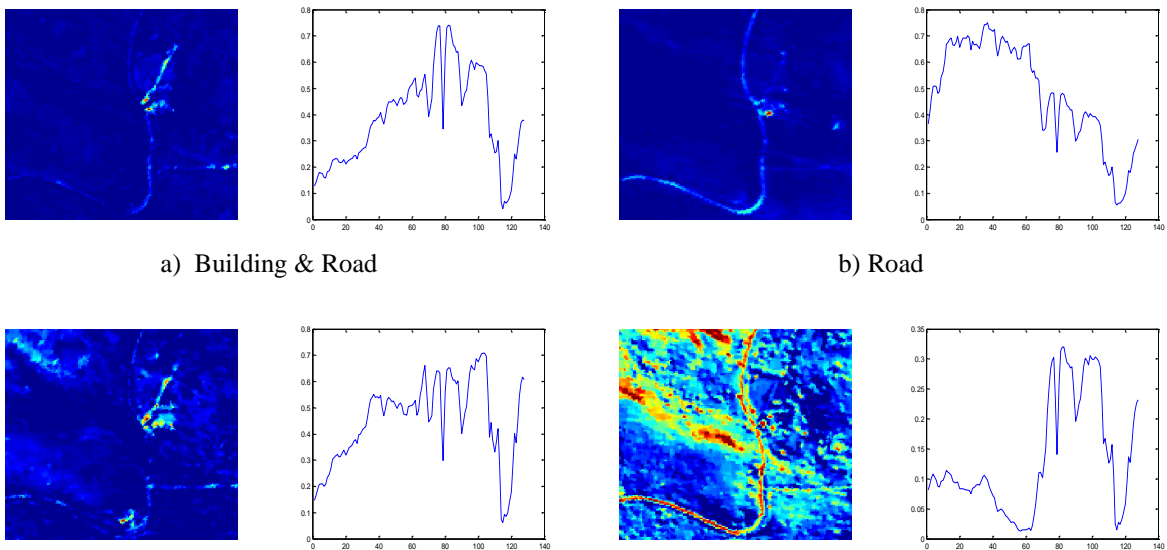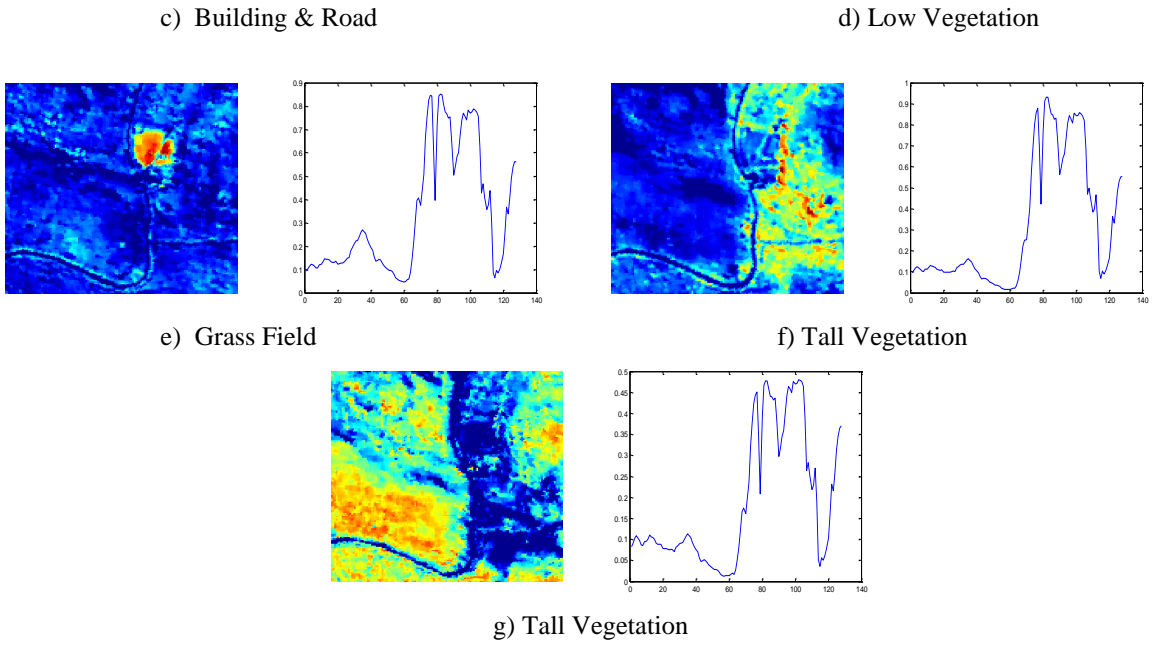
Figure 6-18. Abundances and Endmember resulting from cNMF using for Guanica at 4m.

a) Vegetation & Road   b) Road

c) Building & Road   d) Dirty Road

e) Low Vegetation

f) Building

g) Dirty Road

h) Tall Vegetation

i) Grass Field
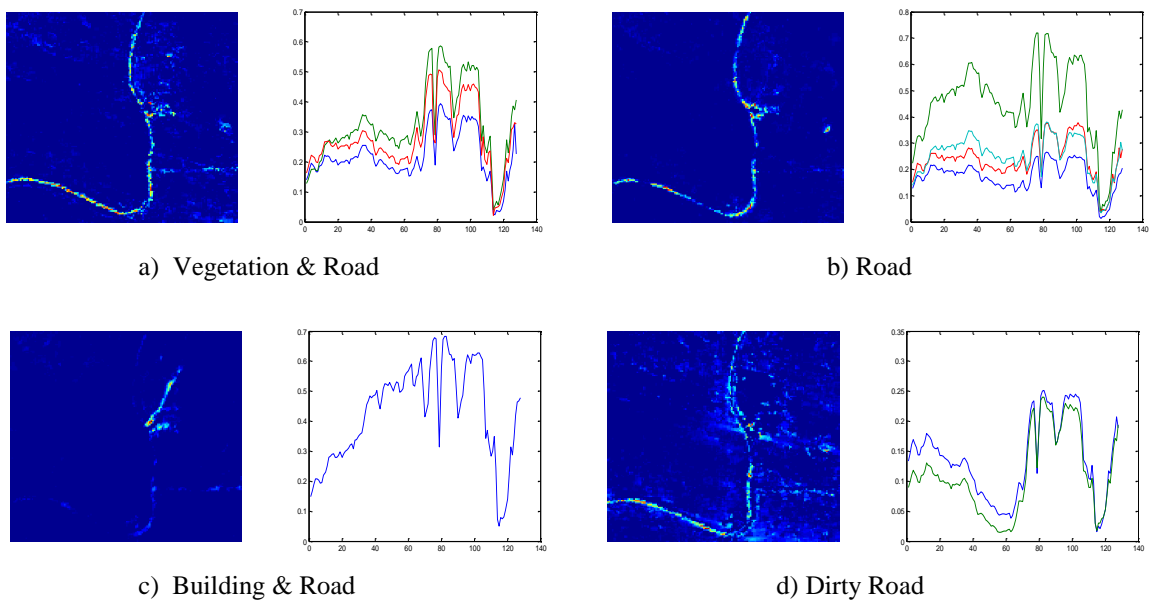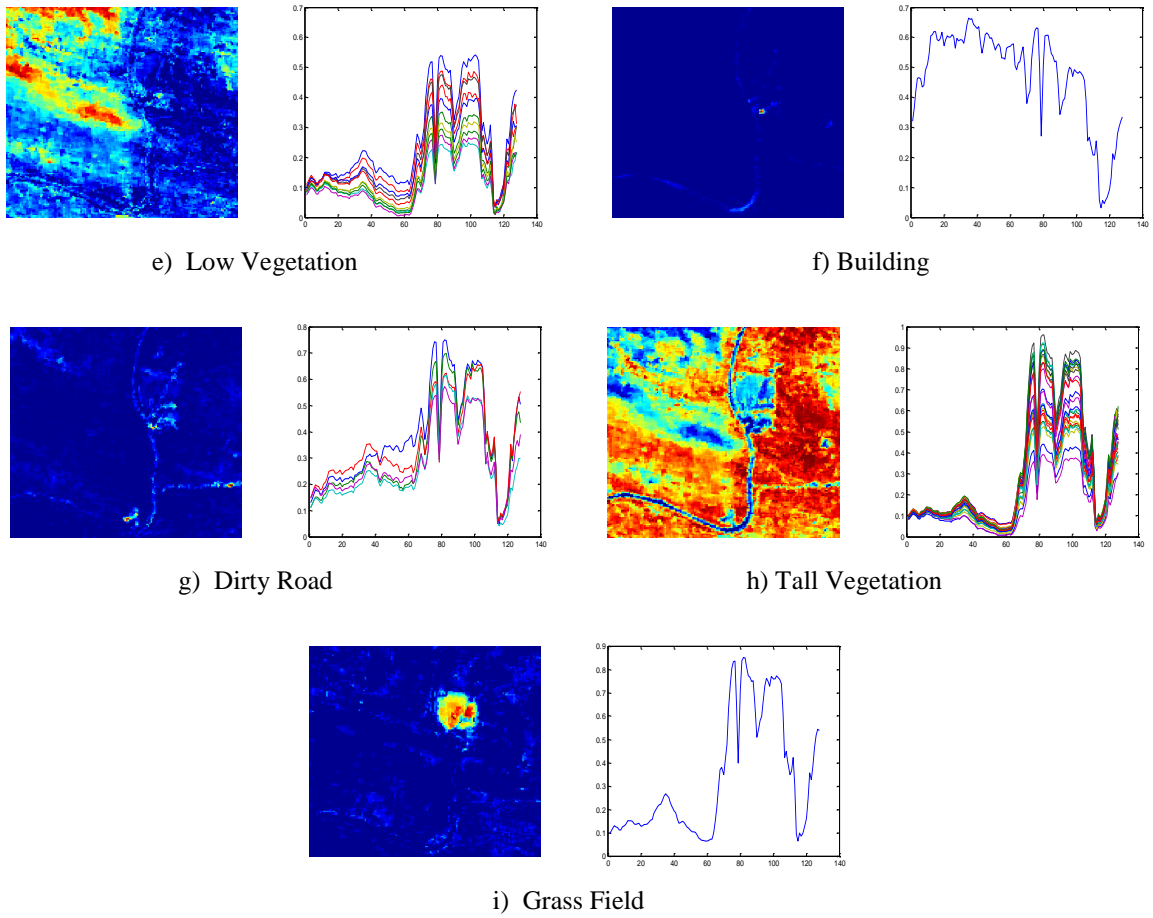
Figure 6-19. Abundances and Endmember classes resulting from sacNMF for Guanica at 4m.
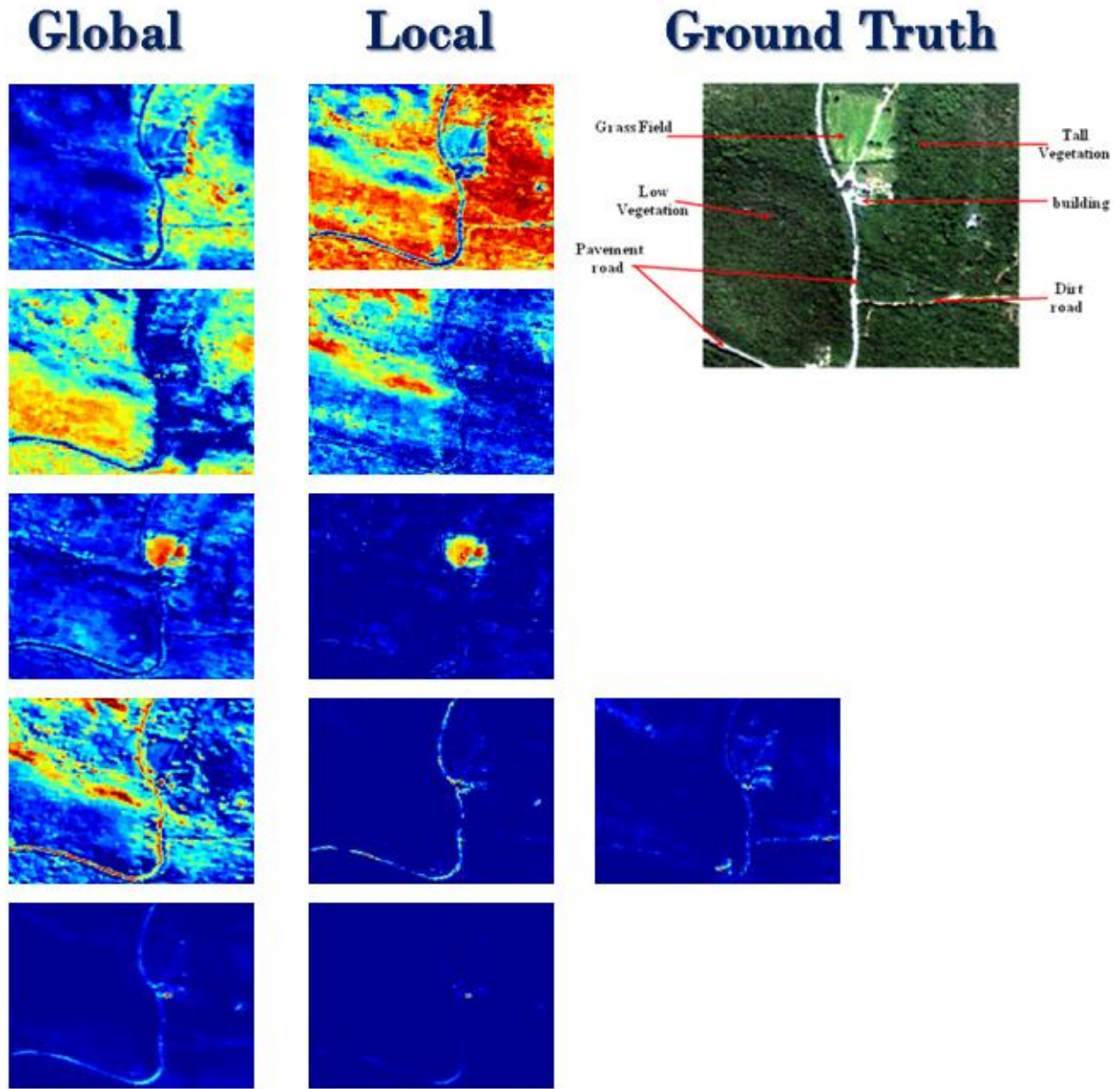
Figure 6-20. Comparisons Abundances from the cNMF and sacNMF for Guanica at 4m.

In Figure 6-20 shows how sacNMF better helps us to detect small materials in the image, compared to cNMF. cNMF mix classes like the road and the low vegetation while sacNMF separate them.

Applying sacNMF to the 1m image the resulting partitions are showed in Figure 6-21 followed by the abundances and endmembers obtained in the processing. The image was divided

139

in 37 tiles, using the norm of the Shannon entropy as split criterion, eleven endmember classes

(108 spectral endmembers) were obtained using sacNMF versus 8 endmembers using cNMF.
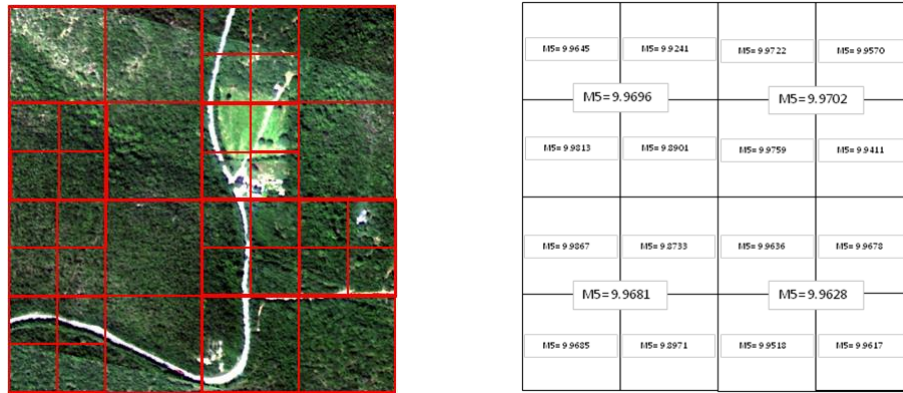
Figure 6-21. Quadtree partitioning using norm of the Shannon Entropy with global index M5 = 9. 9613 for Guanica at 1 m.

a) Building and Road

b) Tall Vegetation

c) Tall Vegetation

d) Grass Field and Dirty Road

e) Vegetation

f) Grass Field and Tall Vegetation

g) Vegetation   h) Vegetation
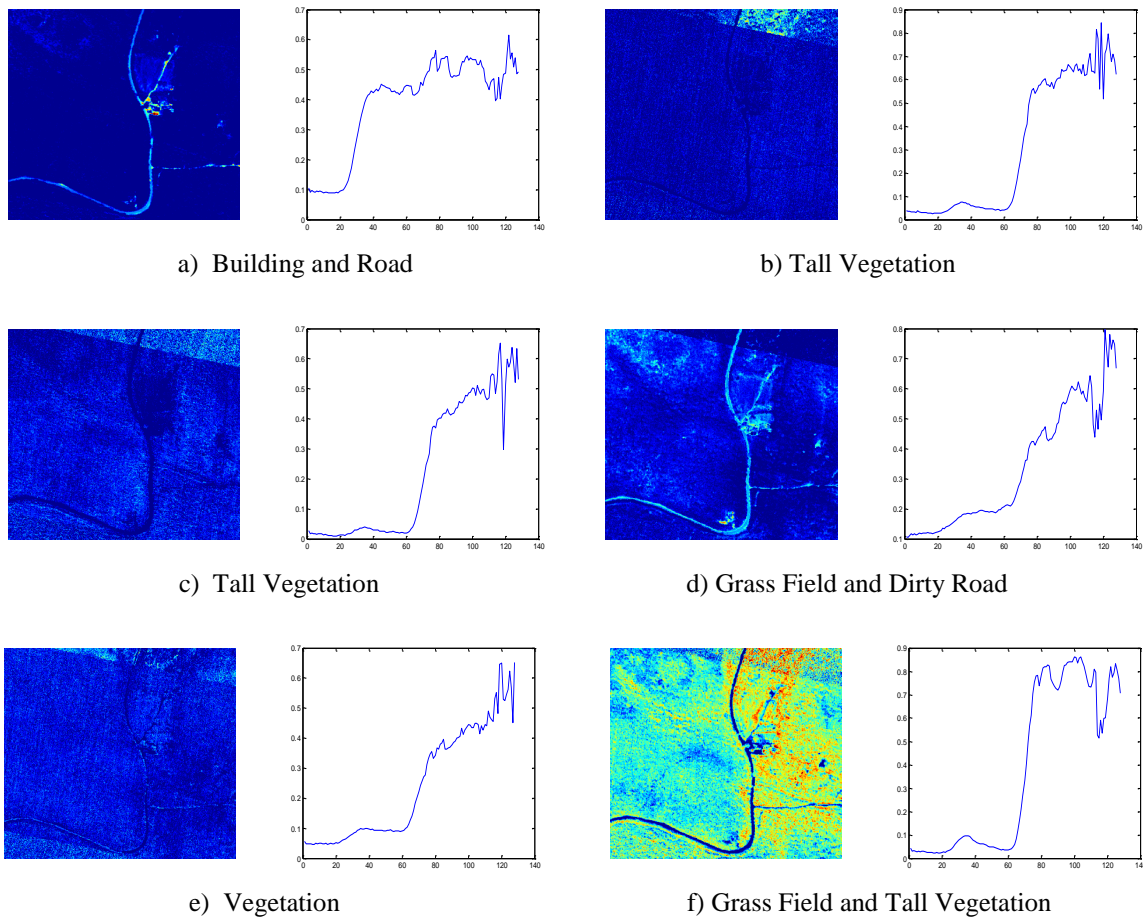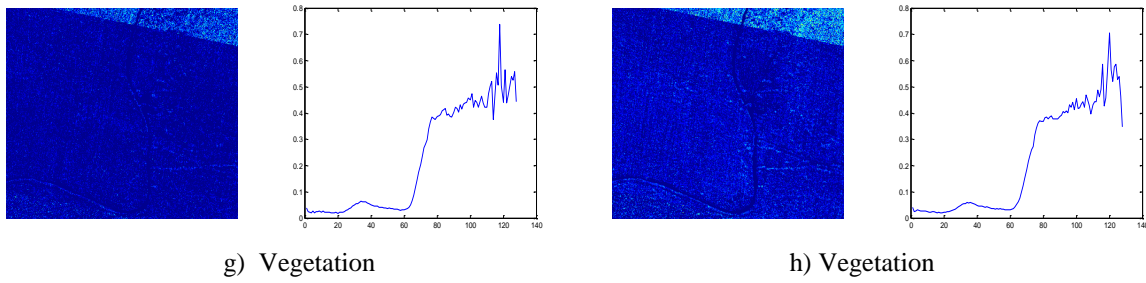
Figure 6-22. Abundances and Endmember resulting from cNMF for Guanica at 1m.

a) Road   b) Grass Field

c) Grass Field   d) Low vegetation and Dirty Road

e) Low vegetation   f) Tall vegetation

g) Dirty Road   h) Building

141

i) Road

j) Road and Building

k) Road
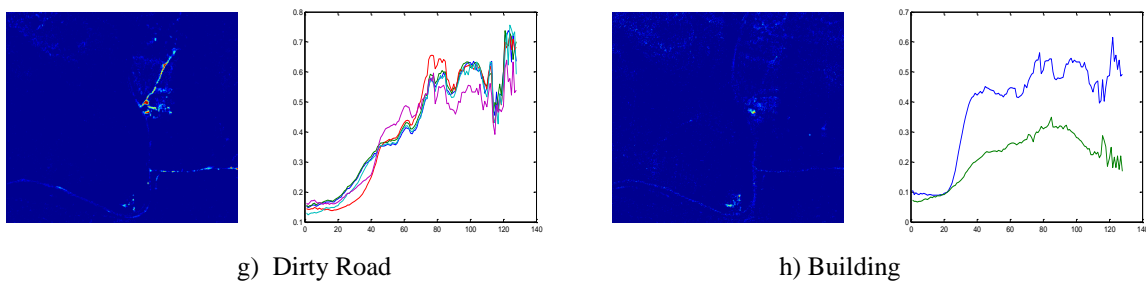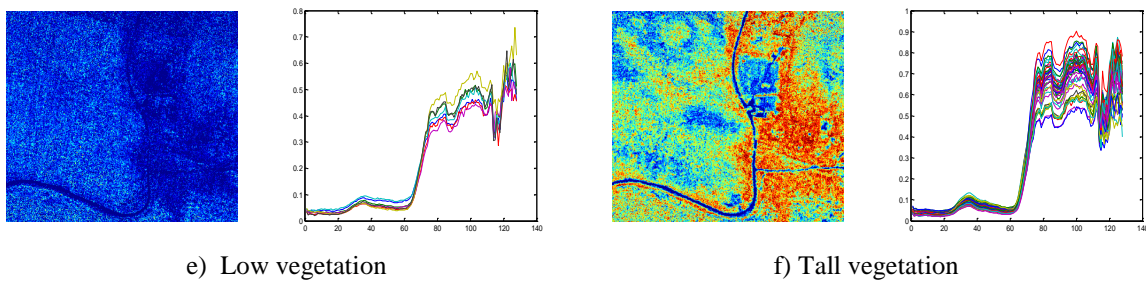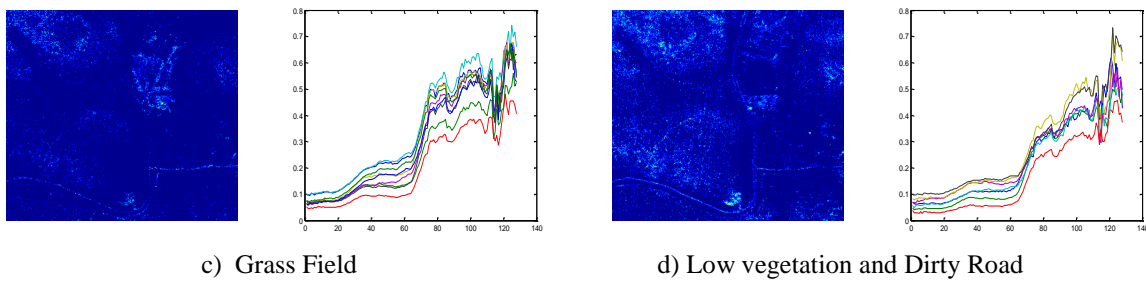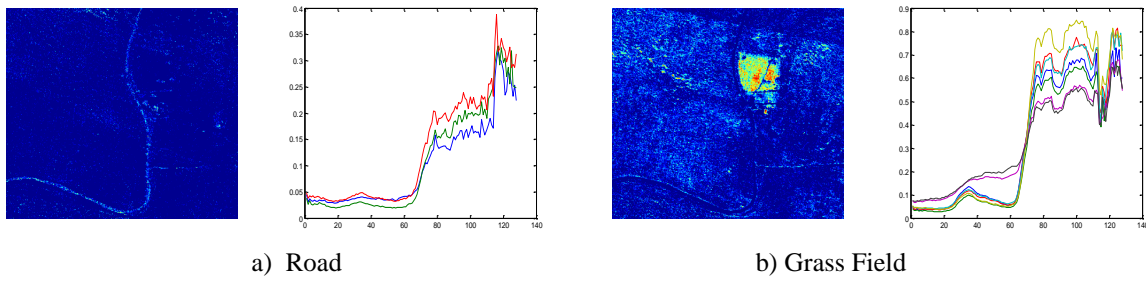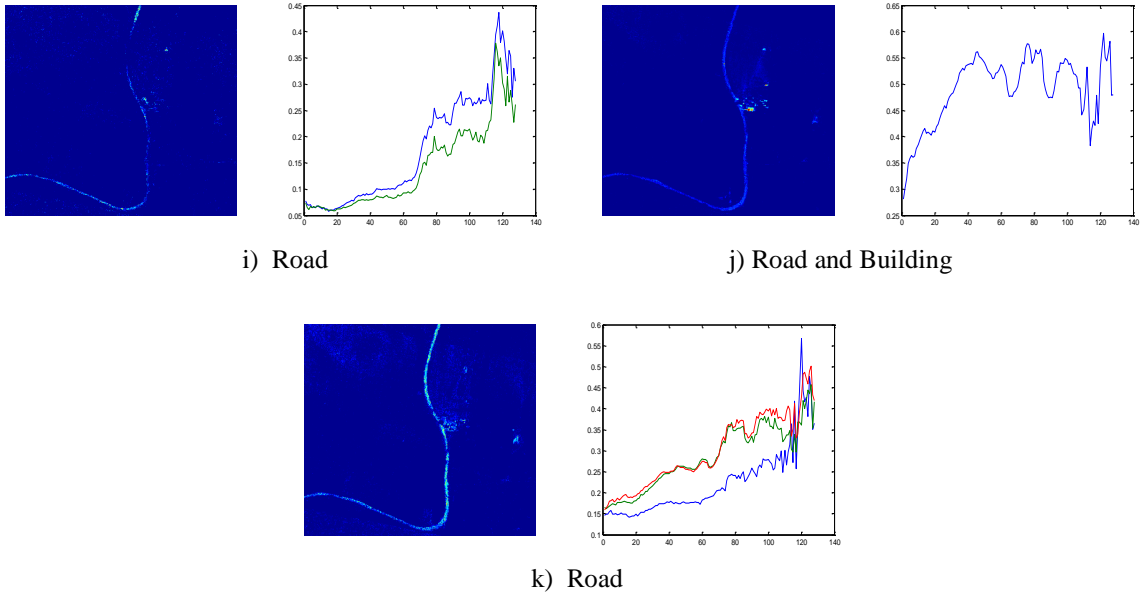
Figure 6-23. Abundances and Endmember classes resulting sacNMF for Guanica at 1m.
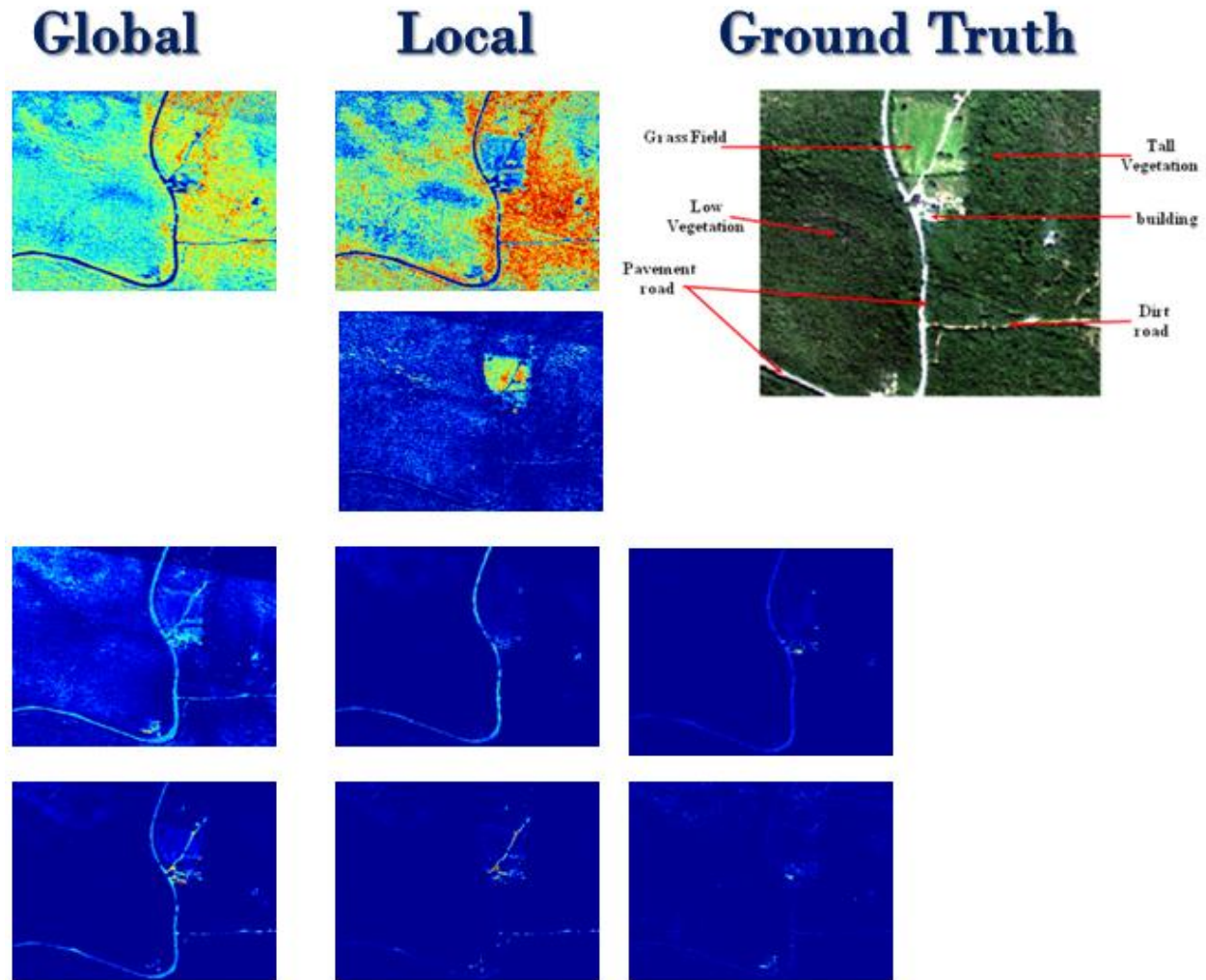
Figure 6-24. Comparison Abundances resulting from cNMF and sacNMF for Guanica at 1m.

Figure 6-24 shows how sacNMF helps us to detect small materials in the image, compared to cNMF. cNMF mixes the grass field and tall vegetation class and sacNMF can separate the dirty road and the pavement road.

The results obtained using the norm of the Shannon entropy shows that the entropy is more sensitive when the image have high resolution partitioning into more divisions. The performace of the approach work in the same manner for both images, obtaining the expected results. In the next Table we can see a summary of the analysis of these images.

143

Table 6-12. Comparative results between the two Guanica resolution images.

Guanica Image	sacNMF			cNMF
Resolution	# End	#End Classes	Classes Average	#End
4 meters	51	9	3.18	7
1 meter	108	11	2.91	8

6.3.2 Comparing Partitions and Classes per Partition.

In this section, we study the partitions of the two resolutions images for Guanica. The number of spectral endmembers obtained for the 1 meter resolution was of 108, and for the 4 meter resolution was 51. The classes per partition can be seen in Figures 6-25 and 6-26. According to the results, the 1 meter resolution image presents more divisions than the 4 meters resolution image. This behavior is presented by the elevated number of pixel in the image that can indicates a high level of variability The value of the norm of Shannon entropy for 1m was 9.961, and for 4m was 8.558.

Figure 6-25. Classes per Partition resulting from the Local unmixing analysis using Nonnegative Matrix Factorization (NMF) for Guanica Dry Forest 1meters image.

144

On the other hand, the 4m resolution image presents a low number of partition in the image. This behavior might be acceptable, as the variability increases with higher resolution.

Figure 6-26. Classes per Partition resulting from the Local unmixing analysis using sacNMF for Guanica at 4m.

6.4   Summary.

This chapter complement the analysis presented in Chapter 4. In addition, experiments with two additional images (Cuprite and Guanica Dry Forest) are presented in addition to visual analysis we used the quantitative analysis method of [43] to evaluate our algorithm. Also, we compared the results obtained with our approach with two other approaches, comparing the APHill with UUMR results and the Indian Pines with SAHU and PCE detection.

Finally, an analysis of the results of two images of the same area (Guanica Dry Forest) with different resolutions was showed, and the behavior of the partitions resulting for each different resolution image were studied. The resulting endmember classes was similar in both analysis 8 for 4 meters resolution image and 11 for 1meter resolution image, but the main materials was detected in both.

7. ETHICAL ISSUES IN REMOTE SENSING.

Ethics is the discipline dealing with what is good and bad and with moral duty and obligation: a branch of philosophy dealing with what is morally right or wrong [81], also ethics is a set of moral principles or values. Sometimes you will hear someone refer to "computing and information ethics", which is a whole range of ethical questions surrounding computer and information science and the use of the computing and information.

Since the field of this dissertation the focus will be on showing the main ethical issues which is required in this type of research. During the preparation of this dissertation we touched important borders where ethical issues are strongly required and clearly appear. When a literature review is done in a PHD research we need to look at others work in the same interesting area. Researcher should be sincere enough to avoid repetition of work and especially in evaluating others work. Without being aware of this point one of very important ethical rules could be broken and then the research will be wrongly structured.

Another important issue in this research is the honesty in the research results. Accuracy in results analysis is important and should be carried over by a big responsibility and honesty, if not as time passes inaccurate research environment will be growing and this will be reflected negatively on the quality of research. Giving credit to other people for using part of their work is important issue also. You as a researcher can use the available information in your research but you cannot be in any way the owner of that work.

It is very important to include that we should ensure a proper and achievable goals and objectives for this research. As final issue I would like to discuss in this part of the proposal is that we are required to make this research beneficial and available for other researchers. Knowledge should be reachable to all scientists in need for this segment of the research environment.

A large number of government and commercial remote sensing systems have been developed capturing images each time with higher spatial resolutions and in a large variety of spectral ranges. Applications of remote sensing technology include environmental monitoring, climate change studies, agriculture, mineral exploration, archeology, meteorology, military application, and others [103]. This wide range of applications and the increasing availability of sensors pose the need of regulation and ethical guidelines regarding to the acquisition, processing, and interpretation of remote sensing imagery.

Some rules have been established as general guidelines for information sharing and technology cooperation among countries that practice remote sensing activities. One of the rules say explicitly that re mote sensing activities cannot have an effect on the autonomy of other lands. These principles are limited to activities in outer space leaving a gap for the regulation of remote sensing activities using aircrafts and do not take into account individual privacy. Privacy is, maybe, the aspect more discussed about remote sensing imagery. The increasing incorporation of this technology in law enforcement activities [82, 104] and the emergence of high spatial resolution imagery systems with information available for everyone pose the question how far the use of these technologies respects the privacy of individuals.

8. CONCLUSIONS AND FUTURE WORK

In most of the unmixing methods for hyperspectral imaging, the spatial information of the hyperspectral images is not exploited, but in recently works the spatial information has become very relevant, and combined with spectral information to develop new algorithms for spectral unmixing. These algorithms include spatial information using the relation between neighborhoods in the unmixing process. Another methods use the spatial information in the preprocessing stage, but working with the standard spectral techniques for endmembers extraction.

The experimental results show the potential of the proposed approach to perform unsupervised unmixing of large scenes images, and to extract spectral endmember classes that better capture the spectral variability in an endmember class. Splitting a large scene into tiles allows the extraction of spectral endmember classes that have small contrast at the full image level but high contrast at the local level. In addition, experimental results show that the Shannon entropy is sensitive to changes caused by natural factors at the image. For instance, in a forest scene, the spectral signature of a particular tree species may vary due to minerals in the soil or by water content. A single spectral signature can, by itself, provide suitable accuracies in some relatively homogeneous environments. Because of the spectral complexity of many landscapes, the use of single endmember spectra to represent a particular material may results in inaccurate analysis for complex regions over large landscapes. Splitting the image in tiles and extracting high number of endmembers to cluster the endmember classes to highlight some material that in global analysis are mixed with other materials.

Our method called Spatially Adaptive Constrained Non Negative Matrix Factorization for Hyperspectral Unmixing, take advantage to process small homogeneous regions to easily detect

single endmembers that represent specific material in the image, and then cluster these endmember for all regions in endmember classes and obtain a global description in the entire image. The image is divided in different regions using the quadtree partition method depending of the splitting criterion (the norm of the Shannon entropy) found homogeneous regions. In this dissertation, we developed an unsupervised unmixing computing system based in Non Negative Matrix Factorization, for large scenes that take full advantage of homogeneous local information using the quadtree partition method and built a global image description.

8.1 Conclusions.

Our method consisted in dividing the hyperspectral image, using the quadtree partition method, in homogeneous regions depending of the splitting criterion. Processing each tile separately to extract the endmembers and clustering them in endmember classes. Then calculate the abundances globally and grouping each abundance in the corresponding endmember class for the global description.

Previously to select the procedure to follow in the algorithm, we made several experiments relating to select the spectral metric to use in our approach. We compare the sensitivity of three different spectral metrics (mean distance from spectral centroid, the mean of all values in the image and the norm of Shannon Entropy), exploring the effects of changing this criterion in the partitioning, and different partitions were obtained with 100, 95, 90, 85, 80, and 75 percent. The results showed the high sensitivity in the Shannon entropy metric which resulted in the best partitioning.

Also, to obtain an adequate number of tiles in the image, we divided two images (AVIRIS APHill and Indian Pines) in 64 tiles manually make the unmixing process and compare with the

results obtained with the partitions obtained to using the norm of Shannon entropy. Although the amount of the endmembers is greater than those obtained using the norm of Shannon entropy, the resulting clusters are the same number for the APHill image, and two more in the Indian Pines image. However, the main endmember classes were extracted, showing that it is not necessary to reach 64 tiles in the image. Only find homogeneous tiles in the image help us to find the endmember classes corresponding with the ground truth of the image.

The results from the proposed approach agree more with published ground truth for the A.P. Hill image than what was possible with the regular cNMF. The endmembers obtained with the cNMF fail to detect small details found in the image that are detected with the local approach using the norm of Shannon entropy metric. The river water is mixed with vegetation, the generic road with the gravel and the soil ag field, obtaining only 6 endmembers versus 13 clusters of the local approach.

Using the Indian Pines image the results from the proposed approach with published ground truth are in more agreement than the results with the regular cNMF. Again, the endmembers obtained with the cNMF cannot detect details found in the image and mix them, while these details are detected with the local approach. The Soybeans & Corn are mixed, the woods with background and grass pasture, the hay-windrowed with the grass and trees, obtaining 8 endmembers versus 12 clusters of the local approach.

In Cuprite image, the results show that with the local analysis, we can separate more classes than the global analysis. The global analysis could detect 15 classes, and with the local analysis we could extract 18 endmember classes. With the local analysis, the Rocks and the Muscovite-

Chlorite can be separate very well and the Alunite and Chalcedony as well while the global analysis fails.

Results from the unmixing analysis for this metric using quadtree partitioning, agree well with published ground truth for the AVIRIS Images as APHill, Indian Pines and Cuprite images. The APHill image analysis results show 43 tiles with 139 endmembers, clustered in 13 endmember classes the overall accuracy was 86.46%. The Indian Pines image analysis results show 31 tiles with 134 endmember, clustered in 12 endmember classes with overall accuracy 82.69%. The Cuprite image analysis results show 37 tiles with 169 endmembers, clustered in 18 endmember classes with overall accuracy 81. 91%.

Furthermore, when results are compared with other approaches, we find similarities results between our method and the Unmixing based on Multiscale representation method [43], being our approach more sensitive in detecting things in the background and very similar in the detection of other mixed classes. For this method, the overall accuracy for APHill was 50.5%, and for Cuprite image was 46.12%. Also, the comparison with the Spatially Adaptive Hyperspectral Unmixing (SAHU) [65] approach (that uses spatial information) extracts only 7 global relevant clasess in the Indian Pines image including the background mixed with other classes. The abundances for these clusters mix the background with woods (vegetation) or the background with roads (Pavement or gray bare soil), another class is the bare soil that corresponds to all crops in the landscape, roof corresponds to stone steel tower class, the wet bare soil that corresponds to the area of hay-windrowed and background, and specular reflection.

The PCE [66] method is an unmixing technique based on the partitioning of spectral data into several convex regions. With this method, the 16 classes were found for the Indian Pines

image with a total of 14 endmembers. Combinations for the 14 endmembers with diferents percents show the abundance result. The corn and soybean classes (notill, min and clean) for example, are compossed by the endmebers 2, 6, and 10 with different percents. Other classes obtained, from the endmembers represent very well the asigned ground truth in more than 70%, and others endmembers represent almost 89% of the abundances (eg. Hay-windrowed, Oats and Wheat). The remaining classes the abundances are mixtures for two o more endmembers.

Again, when we review these methods some classes appear mixed in the same abundance, while our approach can detect small classes and separate them. This is thanks to splitting the image in homogeneous tiles that can be represented by two or three endmembers.

8.2   Future Work.

Some challenges that remain to improve, would basically three things, two of them relate to increase the processing speed of the algorithm and the third related to obtain better results. The first is the runtime processing of the determination of the number of endmembers in each region, in which the image is divided. It is important to find another method equally effective, but with lower processing speed for this calculation. The second thing, is also related to the speed of processing and is the computation of global abundances, it is necessary to find another way, analyzing local abundances and create a relationship with the global, since the calculation of local abundances is faster. And the third thing is related with the process of clustering of endmembers that extract endmember classes, since when we do a manual clustering we can differentiate more classes in the image. Very similar endmembers cannot automatically be separated by clustering.

9. REFERENCES

[1]   John A. Richards and Xiuping Jia. "Remote Sensing Digital Image Analysis". Springer-Verlag Berlin Heidelberg, 2006.

[2]   National Geospatial Intelligence Agency (NGA). "Hyperspectral Imagery (HSI) Dimension Reduction". http://www.ipam.ucla.edu/publications/gss2005/gss2005_5579.ppt

[3]   NASA. Jet Propulsion Laboratory. California Institute of Technology, Last Updated: October 6, 2008. http://aviris.jpl.nasa.gov/html/aviris.overview.html

[4]   Galileo Group Inc. Copyright. All rights reserved. 2007.http://www.galileo-gp.com/_aisa eagle.html

[5]   NASA. ALL RIGHTS RESERVED Copyright California Institute of Technology U.S. Government Sponsorship Acknowledged under NAS7-1260 CL 08-2417 Plone and the Plone logo are registered trademarks of the Plone Foundation. Distributed under the GNU GPL license. 2010. http://hyspiri.jpl.nasa.gov/

[6]   N. Keshava and J.F. Mustard. Spectral unmixing. Signal Processing Magazine, IEEE, 19(1):44-57, Jan 2002.

[7]   Specim. Spectral Imaging Ltd. All Rights Reserved,2007.\ http://www.specim.fi/

[8]   R. Basedow, P. Silverglate, et. al. "The HYDICE Instrument Design." In Proceedings of the International Symposium on Spectral Sensing Research, Vol. 1, pp. 430-445, 1992.

[9]   NASA. "Hyperion Satellite Sensor." http://edc.usgs.gov/products/satellite/eol1.html.

[10]   N. Keshava. " A Survey of Spectral Unmixing Algorithms".In Lincoln Laboratory Journal, 2003. Volume: 14. Number 1, Page(s): 55 - 78, April 2003.

[11]   S. Jia and Y. Qian. Constrained nonnegative matrix factorization for hyperspectral unmixing. Geoscience and Remote Sensing, IEEE Transactions on, 47(1):161 - 173, January. 2009.

[12]   D. D. Lee and H. Sebastian Seung. "Algorithms for Non-negative Matrix Factorization". In Advances in Neural Information Processing, pp. 556-562, 2001.

[13]   D. Donoho and V. Stodden. "When does Non-Negative Matrix Factorization give a correct Decomposition into Parts". In NIPS Workshop on ICA: Sparse Representations in Signal Processing, Whistler, Canada,2003.

[14]   P. Sajda, S. Du and L. Parra. "Nonnegative Matrix Factorization for Rapid Recovery of Constituent Spectra in Magnetic Resonance Chemical Shift Imaging of the Brain". In IEEE Transactions on Medical Imaging, Vol. 23, No. 12, December 2004.

[15]   Yahya M. Masalmah and Miguel Vélez-Reyes. "A full algorithm to compute the constrained positive matrix factorization and its application in unsupervised unmixing of hyperspectral imagery". In Sylvia S. Shen and Paul E. Lewis, editors, Algorithms and Technologies for Multispectral, Hyperspectral, and Ultraspectral Imagery XIV, volume 6966, page 69661C. SPIE, 2008.

[16]   M. Vélez-Reyes and S. Rosario. "Solving abundance estimation in hyperspectral unmixing as a least distance problem". In Geoscience and Remote Sensing Symposium, 2004. IGARSS '04. Proceedings. 2004 IEEE International, volume 5, pages 3276 -3278 vol.5, Sept. 2004.

[17]   Andrea Santos and Miguel Vélez-Reyes. "Understanding the effect of Spatial Resolution on Unmixing Algorithms for Hyperspectral Imagery". Puerto Rico University at Mayaguez Campus. May 2010.

[18]   J. M. van den Hof and J. H. van Schuppen. "Positive Matrix Factorization via Extermal Polyhedral Cones." Linear Algebra and its Applications, Vol.293, pp. 171-186, 1999.

[19]   Chein Chang, Qian Du. "Estimation of number of spectrally distinct signal sources in Hyperspectral Imagery". IEEE Transactions on Geoscience and remote sensing, Vol.42 (3), Page(s): 608-619, March 2004.

[20]   Peter Bajorski. "Does virtual dimensionality work in Hyperspectral Images?". In Sylvia S. Shen and Paul E. Lewis, editors, Algorithms and technologies for Multispectral, Hyperspectral and Ultraspectral Imagery XV, Vol.7334, Page(s): 73341J, SPIE 2009.

[21]   Parente, M., and Plaza, A, "Survey of Geometric and Statistical Unmixing Algorithms for Hyperspectral Images," Proceedings of the 2011 IEEE International Geosciences and   Remote Sensing Symposium, 1135−1138 (2011).

[22]   Masalmah. Y, Vélez-Reyes, M."Unsupervised Unmixing of Hyperspectral Imagery". Circuits and Systems, 2006. MWSCAS'06. 49th IEEE International Midwest Symposium on Volume: 2. Page(s): 337 - 341, October, 2006.

[23]   Y. Wu and K. W. Tam "On Determination of the Number of Signals in Spatially Correlated Noise," IEEE Trans. Signal Processing, vol. 46, no. 11, pp. 3023 - 3029 November 1998.

[24]   K. M. Wong, Q. T. Zhang, J. P. Reilly, and P. Yip, , "A new criterion for the determination of the number of signals in high-resolution array processing", Advanced algorithms and architectures for signal processing III; Proceedings of the Meeting, San Diego, CA, Aug. 15-17, 1988, pp. 352 - 357

[25]   A. P. Liavas, P. A. Regalia and J. P. Delmas, "Blind Channel Approximation: Effective Channel Order Determination," IEEE Trans. Signal Processing, vol. 47, no. 12, December 1999.

[26]   M. Wax and T. Kailath, "Detection of signals by information theoretic criteria," IEEE Trans. Acoust., Speech, Signal Processing, vol. ASSP-33, pp. 387-392, Apr. 1985.

[27]   P. Stoica and Y. Selen. "Model-order selection: a review of information criterion rules", Signal Processing Magazine, IEEE, vol. 21, Issue 4, July 2004, pp. 36-47.

[26]   Gao, L., Zhang, B., Sun, X., Li, S., Du, Q., and Wu, Ch., "Optimized maximum noise fraction for dimensionality reduction of Chinese HJ-1A hyperspectral data". EURASIP Journal on Advances in Signal Processing, Vol 65. 2013. http://asp.eurasipjournals.com/content/2013/1/65.

[27]   Monica Chagoyen, Pedro Carmona-Saez, Concha Gil, Jose Maria Carazo, and Alberto D. Pascual-Montano."A literature-based similarity metric for biological processes". BMC Bioinformatics, 7-363, 2006. [19] K. Eriksson, D. Estep, P. Hansbo, C. Johnson, "Computational differential equations", 1996.

[28]   A. Umaña and M. Vélez-Reyes. "Determining the dimensionality of hyperspectral imagery for unsupervised band selection". In Proceedings of SPIE, volume 5093, 2003.

[29]   J. W. Boardman, F. A. Kruse, and R. O. Green. "Mapping Target Signatures via Partial Unmixing of AVIRIS Data". In Proceedings of JPL Airborne Earth Science Workshop, Pasadena, CA, 1995. http://aviris.jpl.nasa.gov.

[30]   M. E. Winter."Comparison of Approaches for Determining End-Members in Hyperspectral Data". In Proceedings of the Aerospace Conference, Vol. 3, Page(s): 305-313, 2000.

[31]   L. Parra, C. Spence, P. Sajda, A. Ziehe, and K. R. Mller. "Unmixing Hyperspectral Data". In Advances in Neural Information Processing, Vol. 12 (Proc. NIPS*99), Page(s): 942- 948, MIT Press, 2000.

[32]   M. E. Winter. "Fast Autonomous Spectral Endmember Determination in Hyperspectral Data". In Proceedings of the Thirteenth International Conference on Applied Geologic Remote Sensing, Vol. II, Page(s): 337-344, Canada 1999.

[33]   Michael E. Winter. N-findr: an algorithm for fast autonomous spectral endmember determination in hyperspectral data. In Michael R. Descour and Sylvia S. Shen, editors, Imaging Spectrometry V, volume 3753, pages 266-275.SPIE, 1999.

[34]   Qian Du, Nareenart Raksuntorn, Nicolas H. Younan, and Roger L. King. Variants of n-findr algorithm for endmember extraction. In Lorenzo Bruzzone, Claudia Notarnicola, and Francesco Posa, editors, Image and Signal Processing for Remote Sensing XIV, volume 7109. SPIE, 2008.

[35]   K. Lee. A Subpixel Scale Target Detection Algorithm for Hyperspectral Imagery. PhD thesis, Rochester Institute of Technology, Center for Imaging Science, 2003.

[36]   J. Nascimento and J. Dias. "Vertex component analysis: A fast algorithm to extract endmembers spectra from Hyperspectral data". In Proceedings of the First IbPRIA, vol. 2652, pp. 626-635, Spain, 2003.

[37]   G. Solyar, C. Chang, and A. Plaza. "Endmember generation by projection pursuit". In Proceedings of SPIE: Algorithms and Technology for Multispectral, Hyperspectral, and Ultraspectral Imagery XI, vol. 5806 , April 2005.

[38]   A. Hyvarinen, J. Karhunen, and E. Oja. "Independent Component Analysis". John Wiley and Sons, 2001.

[39]   A. Ifarraguerri and C. Chang. "Hyperspectral image segmentation with convex cones". In IEEE Transactions on Geoscience and Remote Sensing, vol. 37, No. 2, pp. 756-770, March 1999.

[40]   Plaza, A., Martinez, P., Perez, R., and Plaza, J., "Spatial/Spectral Endmember Extraction by Multidimensional Morphological Operations". In IEEE Transactions on Geoscience and Remote Sensing, Vol. 40, No. 9, pp. 2025-2041, September 2002.

[41]   Rogge, D. M., Rivard, B., Zhang, J., Sanchez, A., Harris, J. and Feng, "Integration of spatial and spectral information for the improved extraction of endmembers," Remote Sensing of Environment Vol 110, pp. 287−303, February 2007.

[42]   M. Velez-Reyes, S. Rosario, A. Puetz and R. B. Lockwood. "Iterative Algorithms for Unmixing of Hyperspectral Imagery". In Proceedings of SPIE: Algorithms and Technologies for Multispectral, Hyperspectral, and Ultraspectral Imagery IX, Vol. 5093, April 2003.

[43]   M. C. Torres-Madroñero. "Unsupervised Unmixing Analysis Based on Multiscale Representation". UPRM Dissertation. 293 Pages. 2013.

[44]   Shi, C., Wang, L., "Incorporating spatial information in spectral unmixing: A review," Remote Sensing of Environment Vol 149, pp. 70−87, May 2014.

[45]   A. Pascual-Montano, J.M. Carazo, K. Kochi, D. Lehmann, and R.D. Pascual-Marqui. "Nonsmooth nonnegative matrix factorization (nsnmf)". Pattern Analysis and Machine Intelligence, IEEE Transactions on, 28(3), Page(s):403-415, March 2006.

[46]   Patrik O. Hoyer. "Non-negative matrix factorization with sparseness constraints". *Journal of Machine Learning Research* 5, Aug 2004.

[47]   Daniel D. Lee and H. Sebastian Seung. Learning the parts of objects by nonnegative matrix factorization. Nature, 401(6755), Page(s):788-791, October 1999.

[48]   Seung-Jean Kim, K. Koh, M. Lustig, S. Boyd, and D. Gorinevsky. An interiorpoint method for large-scale l1-regularized least squares. Selected Topics in Signal Processing, IEEE Journal of, 1(4), Page(s):606-617, Dec. 2007.

[49]   D. Manolakis, G. Shaw, and N. Keshava. "Comparative analysis of hyperspectral adaptive matched filter detectors", in Proc. of the SPIE, Apr. 2000.

[50]   Chang C. I., Ren H. et. al. "Subpixel Target Size Estimation for Remotely Sensed Imagery". In Proceedings of SPIE: Algorithms and Technologies for Multispectral, Hyperspectral, and Ultraspectral Imagery IX, Vol. 5093, April 2003.

[51]   L. Jimenez, D.A. Landgrebe, "Projection pursuit in high dimensional data reduction: Initial conditions, feature selection and the assumption of normality, "Proceedings of the IEEE International Conference on Systems, Man and Cybernetics 1, Oct 22-25, 1995.

[52]   J.C. Harsanyi, C.-I. Chang, "Hyperspectral image classification and dimensionality reduction: An orthogonal subspace projection approach," IEEE Transactions on Geoscience and Remote Sensing, vol.32, no.4, July 1994.

[53]   C.-I. Chang, X.-L. Zhao, M.L.G. Althouse, J.J. Pan, "Least squares subspace projection approach to mixed pixel classification for hyperspectral images," IEEE Transactions on Geoscience and Remote Sensing vol.36 no.3, May 1998.

[54]   Ben Somers, Gregory P. Asner, Laurent Tits, Pol Coppin, "Endmember variability in Spectral Mixture Analysis: A review", Remote Sensing of Environment, Volume 115, Issue 7, 15 July 2011, Pages 1603-1616, ISSN 0034-4257.

[55]   S. Schweizer, J. Moura, "ML-detection in hyperspectral imagery: A GMRF modeling approach," Proceedings of SPIE-The International Society for Optical Engineering 3717 p 125-134 Apr 5-Apr 6 1999.

[56]   K. Segl, S. Roessner, "Pixel oriented selection of endmember combination for linear stochastic spectral unmixing applied to urban environments," SPIE, vol.3753, July 1999.

[57]   A. Stocker, A. Schaum, "Application of stochastic mixing models to hyperspectral detection problems," Proceedings of SPIE - The International Society for Optical Engineering, v 3071, p 47-60, Apr 22-23 1997.

[58]   M. Petrou, P.G. Foschi, "Confidence in linear spectral unmixing of single pixel," IEEE Transactions on Geoscience and Remote Sensing, vol.37, no.1, January 1999.

[59]   G.H. Golub, C.F. Van Loan, "An analysis of the total least squares problem," Siam J. Numer. Anal., vol.17, no.6, December 1980.

[60]   P.E. Gill, W. Murray, M.H. Wright, "Practical optimization," Academic Press, London, 1981.

[61]   M.J.D. Powell, "The convergence of variable metric methods for nonlinearly constrained optimization calculation", Nonlinear programming 3d, (O.L. Mangasarian, R.R. Meyer, and S.M. Robinson, eds.) Academic Press, 1978.

[62]   S. Wild, J. Curry, and A. Dougherty. "Motivating Non-negative Matrix Factorizations."In Eighth SIAM Conference on Applied Linear Algebra, Philadelphia, 2003.

[63]   P. Paatero and U. Tapper. "Positive Matrix Factorization: A Non-negative Factor Model with Optimal Utilization of Error Estimates of data values." Environmetrics, Vol. 5, pp. 111-126, 1994.

[64]   S. Marinetti, L. Finesso, E. Marsilio. "Matrix Factorization Methods: Application to Thermal NDT/E." In Proceedings of the Fifth Workshop, Advances in Signal Processing for Non Destructive Evaluation Materials, Canada, 2006.

[65]   F. Shahnaz, M. Berry, P. Pauca, and R. Plemmons. "Document Clustering using Nonnegative Matrix Factorization." In Information Processing and Management, Vol. 42, No. 2, pp. 373-386, 2006.

[66]   A. N. Langville, M. W. Berry, M. Browne, V. P. Pauca, and R. J. Plemmons. "Algorithms and Applications for the approximate Nonnegative Matrix Factorization." In Computational Statistics and Data Analysis. Elsevier. 2007.

[67]   M. Chu, F. Diele, R. Plemmons, and S. Ragni. "Optimality, Computation, and Interpretations of Nonnegative Matrix Factorizations." In SIAM Journal on Matrix Analysis, October 2004.

[68]   P. Pauca, J. Piper, and R. Plommens. "Nonnegative Matrix Factorization for Spectral Data Analysis." to appear In Linear Algebra and its Application, 2005.

[69]   C.-J. Lin. "Projected gradient methods for non-negative matrix factorization."To appear in Neural Computation, 2007.

[70]   J. M. van den Hof and J. H. van Schuppen. "Positive Matrix Factorization via Extermal Polyhedral Cones." Linear Algebra and its Applications, Vol.293, pp. 171-186, 1999.

[71]   C. E. Rasmussen and C. K. I. Williams."Gaussian Processes for Machine Learning". MIT Press, 2006.

[72]   M.N. Schmidt, H. Laurberg."Non-negative Matrix Factorization with Gaussian Process Priors". Technical University of Denmark and Aalborg University. 17 Pages, January 16, 2008.

[73]   A. Cichocki, R. Zdunek, and S. ichi Amari, "Csiszar's divergences for nonnegative matrix factorization: Family of new algorithms".In lecture notes in Computer Science, vol. 3889, pp. 32-39, 2006.

[74]   J. M. van den Hof and J. H. van Schuppen. "Positive Matrix Factorization via Extermal Polyhedral Cones." Linear Algebra and its Applications, Vol.293, pp. 171-186, 1999.

[75]   T. Virtanen, A.T. Cemgil. "Mixtures of Gamma Priors for Non-Negative Matrix Factorization based Speech Separation". Tampere University of Technology. Tampere, Finland. Bogazici University, Istanbul, Turkey.2009.

[76]   E. Esser, M. Moller, S. Osher, G. Sapiro, and Xin, J. "A Convex Model for Nonnegative Matrix Factorization and Dimensionality Reduction on Physical Space". IEEE Transactions on Image Processing. Vol. 21, Issue 7. July 2012, Page(s): 3239 - 3252.

[77]   W. Yu-Xiong, Z. Yu-Jin. "Nonnegative Matrix Factorization: A Comprehensive Review". IEEE Transactions on Knowledge and Data Engineering. Vol. 25, Issue 6. June 2013, Page(s): 1336 - 1353.

[78]   W. Nan, D. Bo and Z. Liangpei. "An Endmember Dissimilarity Constrained Non-Negative Matrix Factorization Method for Hyperspectral Unmixing". IEEE Journal of Selected Topics in Applied Earth Observations and Remote Sensing. Vol. 6, Issue 2. April 2013, Page(s): 554 - 569.

[79]   K. Wilson, B. Raj, P. Smaragdis, A. Divakaran. "Speech Denoising Using Nonnegative   Matrix Factorization with Priors". Mitsubishi Electric Research Laboratories. August 2008.

[80]   Zare, A.; Gader, P." PCE: Piece-wise Convex Endmember Detection". IEEE   Transactions on Geoscience and Remote Sensing. Vol. 48, Issue 6. June 2010, Page(s): 2620 - 2632.

[81]   Canham, K., Schlamm, A., Basener, B., Messinger D., "High Spatial Resolution   Hyperspectral Spatially Adaptive Endmember Selection and Spectral Unmixing", Algorithms and Technologies for Multispectral, Hyperspectral and Ultraspectral Imagery. Proc. of SPIE Vol. 8046 (80481O-1), 2011 SPIE.

[82]   http://aviris.jpl.nasa.gov/data/free_data.html, and   http://speclab.cr.usgs.gov/

[83]   Jia, S. and Qian, Y., "Constrained Nonnegative Matrix Factorization for Hyperspectral Unmixing," IEEE Transactions on Geoscience and Remote Sensing, Vol. 47, No. 1. January 2009, Page(s): 161 – 173.

[84]   Liu, X., Xia, W., Wang, B., and Zhang, L. "An Approach Based on Constrained Nonnegative Matrix Factorization to Unmix Hyperspectral Data," IEEE Transactions on Geoscience and Remote Sensing, Vol. 49, No. 2. February 2011, Page(s): 757 – 772.

[85]   Qian, Y., Jia, S., Zhou, J., and Robles-Kelly, A. "Hyperspectral Unmixing via L½ Sparsity-Constrained Nonnegative Matrix Factorization," IEEE Transactions on Geoscience and Remote Sensing, Vol. 49, No. 11. November 2011, Page(s): 4282 – 4297.

[86]   Yokoya, N., Yairi, T., and Iwasaki, A. "Coupled Nonnegative Matrix Factorization Unmixing for Hyperspectral and Multispectral Data Fusion," IEEE Transactions on Geoscience and Remote Sensing, Vol. 50, No. 2. February 2012, Page(s): 528 – 537.

[87] Chang, C. and Ji, B., "Weighted abundance-constrained linear spectral mixture analysis," IEEE Transactions on Geosciences and Remote Sensing 44, 378−388 (2006).

[88] Cipar, J. J., Lockwood, R., Cooley, T., and Grigsby, P., "Background spectral library for fort A.P. Hill, Virginia," Proc. SPIE. 5544, 35–46 (2004).

[89] Chang, C. and Du, Q., "Estimation of number of spectrally distinct signal sources in Hyperspectral Imagery," IEEE Transactions on Geosciences and Remote Sensing 42(3), 608-619 (2004).

[90] Masalmah, Y. and Velez-Reyes, M., "Unsupervised unmixing of hyperspectral imagery," Proceedings of the 49th IEEE International Midwest Symposium on Circuits and Systems 2, 337-341 (2006).

[91] Goenaga-Jimenez, M. and Velez-Reyes, M., "Incorporating Local Information in Unsupervised Hyperspectral Unmixing". SPIE Conference. Security and Sensing Baltimore, 23-27 April 2012.

[92] Parente, M., and Plaza, A, "Survey of Geometric and Statistical Unmixing Algorithms for Hyperspectral Images," Proceedings of the 2011 IEEE International Geosciences and Remote Sensing Symposium, 1135−1138 (2011).

[93] Bioucas-Dias, J. and Plaza, A., Dobigeon, N., Parente, M., Du, Q., Gader, P., and Chanussot, J., " Hyperspectral Unmixing Overview: Geometrical, Statistical and Sparse Regression-Based Approaches," IEEE Journal of Selected Topics in Applied Earth Observations and Remote Sensing, Vol. 5, No. 2. April 2012, Page(s): 354 – 379.

[94] Rogge, D. M., Rivard, B., Zhang, J., Sanchez, A., Harris, J. and Feng, "Integration of spatial and spectral information for the improved extraction of endmembers," Remote Sensing of Environment 110, 287−303 (2007).

[95] Manolopoulos Y., Papadopoulos A. N., Vassilakopoulos M. "Spatial Databases: Technologies, Techniques and Trends". Idea Group Inc (IGI), 340 P, Dec 31, 2004.

[96] Rocchini, D." Effects of spatial and spectral resolution in estimating ecosystem α-diversity by satellite imagery" Remote Sensing of Environment, Volume 111, Issue 4, 28 December 2007, Pages 423-434.

[97] Rocchini, D., Blakenhol, N., Carter, G., Foody, G., Gillespie, and T. "Remotely sensed spectral heterogeneity as a proxy of species diversity: Recent advances and open challenges". Ecological Informatics, Volume 5, Issue 5, September 2010, Pages 318-329.

[98] Palmer, M., Earls, P., Hoagland, B., White, P., Wohlgemuth, T. "Quantitative tools for perfecting species lists". Environmetrics, Volume 13, Issue 2, March 2002, Pages 121-   137.

[99] Richards, J. A. and Jia, X. "Remote Sensing Digital Image Analysis: An Introduction",   2nd Ed., Springer, Berlin, (2006).

[100] Goenaga, M. A.; Torres-Madronero, M. C.; Velez-Reyes, M.; Van Bloem, S. J.; Chinea,   J.   D." Unmixing Analysis of a Time Series of Hyperion Images Over the Guánica Dry   Forest in Puerto Rico". Journal of Selected Topics in Applied Earth Observations and Remote Sensing, IEEE Geoscience; Signal Processing & Analysis Issue: 99. 2012, Page(s): 1 - 10.

[101] Zhang W., Dai M., Yin C. "Compression of hyper-spectral images based on quadtree partitioning". 2nd IEEE International Conference on Computer Science and Information Technology, 2009, Page(s): 421 - 423.

[102] Duarte, J., Velez-Reyes, M., Castillo, P. "Scale-Space in Hyperspectral Image Analysis". SPIE Defense and Security Symposium (Orlando, Fl.) vol. 6233, pp. 334-345, 2006.

[103] Dongxiang C., Tiankun L. "Iterative Quadtree Decomposition Segmentation of Liver MR Image". International Conference on Artificial Intelligence and Computational   Intelligence,   2009. Volume: 3, Page(s): 527 - 529.

[104] Kantardzic M., "Data Mining: Concepts, Models Methods, and Algorithms", Wiley-IEEE Press, Hoboken, (2002).

[105] R Purdy, "Attitudes of UK and Australian farmers towards monitoring activity with satellite technologies: Lessons to be learnt," Space Policy, vol. 27, 4, pp 202-212, 2011.

[106] S. McKee, "Remote sensing issues at the supreme court of Canada," Bulletin association of Canadian map libraries and archives, vol. 123, pp 3-6, 2005.

[107] Ben Somers, Gregory P. Asner, Laurent Tits, Pol Coppin, Endmember variability in Spectral Mixture Analysis: A review, Remote Sensing of Environment, Volume 115, Issue 7, 15 July 2011, Pages 1603-1616, ISSN 0034-4257.

[108] http://www.merriam-webster.com/dictionary/ethic